Geology, geochemistr sotope analysis of the Vredenburg Batholi Columbine Granites Paternoster/Vredenbur a: Implications on their petrogenesis, tectonic setting, and sources.

by

Luke Adriaans

Thesis submitted in fulfillment of the requirements for the degree of Master of Science in the Faculty of Natural Sciences at the University of the Western Cape

Supervisor: Dr. Russell Bailie

Declaration

I, Luke Adriaans, hereby declare that the work contained in this dissertation is my own original work and that I have not previously, in its entirety or in part, submitted it at any other university for a degree.

Signature: . . . . 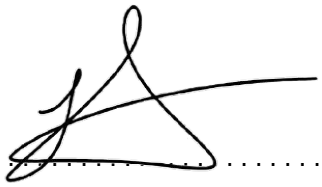 . . . . . .

Luke Adriaans

Date: 21/ 02/ 2018

Abstract

The late− to post−collisional Cape Granite Suite (CGS) located in the southwest of South Africa is comprised of S−, I−, and A−type granites, mafic intrusives, and volcanic flows. The CGS is interpreted to have formed during the closing of the Adamastor Ocean during the Late−Proterozoic to Early−Cambrian. Recently, the S−type granites have received much attention concerning their petrogenesis and sources. However, the I− and A−type granites remain poorly understood and little studied. Therefore, with new geochemical and isotopic data the petrogenesis, sources, and tectonic settings of I− (Vredenburg Batholith) and A−type (Cape Columbine) granites of the CGS form the focus for this study.

The major and trace element data presented in this thesis show that the granites from the Vredenburg Batholith are weakly peraluminous to metaluminous, ferroan, and alkali−calcic. Associated with the granites are metaluminous, magnesian, and calc−alkalic igneous enclaves. Formerly, the granites have been interpreted to have formed by fractionation. However, with new geochemical analyses and re-assessment of such models, it can be shown that such processes are incompatible with accounting for the chemical variation displayed by the granites and their enclaves. Moreover, the I−type granites and enclaves exhibit positive linear trends between whole−rock major and trace elements vs. maficity (Fe + Mg), which can be explained by co−entrainment of peritectic and accessory phases. The lithogeochemical characteristics of the enclaves and host granite reflect melting of a heterogeneous source. Moreover, the granite and enclave's $\varepsilon Nd_{(t)}$ values reflect melting of Paleoproterozoic-aged crustal sources. Finally, with tectonomagmatic discrimination diagrams, it can be shown that the tectonic setting of the granites indicates a transition from a collisional to extensional regime which corroborates the inferences of previous studies.

The Cape Columbine Granites lithogeochemical characteristics are ferroan, calc−alkalic and weakly peraluminous. They show typical A−type granite characteristics in having high silica content, high Na + K values, REE enrichment as compared to S− and I−type granites and strong negative Eu anomalies. For this thesis, it can be shown that anatexis of quartzofeldspathic protolith in an extensional regime produced the chemical variation of the Cape Columbine Granite. Moreover, their isotope ratios are typically radiogenic, indicative of a crustal origin. With this new geochemical data evidence is provided against and in support of previous inferences made about the petrogenesis of the I− and A−type granites of the CGS. This also betters our understanding of the magmatic processes involved in the construction of the CGS over time.

Keywords: Vredenburg Batholith, Cape Columbine Granite, Petrogenesis, Sources.

Acknowledgements

I would like to thank the many people who contributed to the completion of this Masters dissertation. My sincerest appreciation is expressed to the following people and organisations:

1) My supervisor Dr. Russel Bailie for the continuous support, encouragement, knowledge, supplementation of articles and his invaluable guidance. This dissertation would not have been possible without your help.

2) To Gharlied Abrahams for aiding me with the geochemical software and plotting data. Also, for the knowledge shared.

3) To all my friends who continuously let me know that I make them proud. Well, I hope I can continue that feat.

4) I would like to thank the NRF, for funding my MSc project over the course of 2 years.

5) Lastly, thanks to my parents for all their support and encouragement.

Contents

List of figures

List of Tables

Chapter 1 Introduction

Granites occupy volumetrically the greatest portion of continental crust and thus their magma production provides a significant degree of crustal contribution (Farina et al., 2012; Moyen et al., 2016). Granites have been classified into S−, I−, and A−types based on their protoliths and the tectonic environment in which they are produced (Chappell and White, 1974; Loiselle and Wones, 1979). In any given S− and I−type granitic intrusion, a range of rock compositions can occur from relatively mafic compositions (granodiorites) to the most felsic leucogranites (Clemens, 2012; Villaros et al., 2009a). Moreover, the petrogenetic processes involved in producing such a diverse set of rocks remains a matter of debate and are poorly understood (Clemens and Stevens, 2012; Clemens et al., 2011; Farina et al., 2012; Gao et al., 2014). Some models have gained favourable recognition, such as fractional crystallisation of a mantle source magma, magma mixing between crustally− and mantle−derived magmas, varying degrees of partial melting, restite unmixing, and, most recently, peritectic assemblage entrainment (Barbarin, 1999; Chappell and White, 1974; 1984; Clemens 2012, Clemens and Stevens, 2012; Frost et al., 2001; Frost and Frost, 2011; Stevens et al., 2007, and references therein). Full descriptions of the processes are discussed below (Section 1.1) and in the referenced articles. For this thesis, these models will only be tested for I− and A−type granite associations.

Along the west coast of South Africa there are a series of pluton and batholith phases that progress from S−, to I− and finally, A−type granites belonging to the Mid-Ediacaran and Early Cambrian Cape Granite Suite (CGS) (Clemens et al., 2017a; d; Fig.1.1). The latter two types are the focus of this study, in particular, the Vredenburg batholith (I−type) and the Cape Columbine granites (A−type or ferroan). Recently, considerable attention has been given to the petrogenesis and geochronology of the CGS (Clemens et al., 2017a; d; Stevens et al., 2007; Villaros et al., 2009a; b). However, these studies have mainly focused on its S−type granites, including the Saldanha and Postberg ignimbrites, as well as the intermediate to mafic Yzerfontein pluton. Comparatively few studies have been done on the petrogenesis of the Vredenburg and Cape Columbine granites. In fact, the last comprehensive study of the Vredenburg granites was conducted a few decades ago (Scheepers, 1981), and in a general study on the geochemistry and petrogenesis of the CGS (Scheepers, 1995). The findings of Scheepers (1995) suggest that the I−type granites were a result of fractional crystallisation and subduction−related processes and that the A−type granites were produced by melting of a quartzofeldspathic source in an extensional setting. It will be shown here why a fractionation model alone cannot explain the chemical variation of the I−type granites; whereas, the findings of this study are consistent with his conclusions about the A−type granite production.

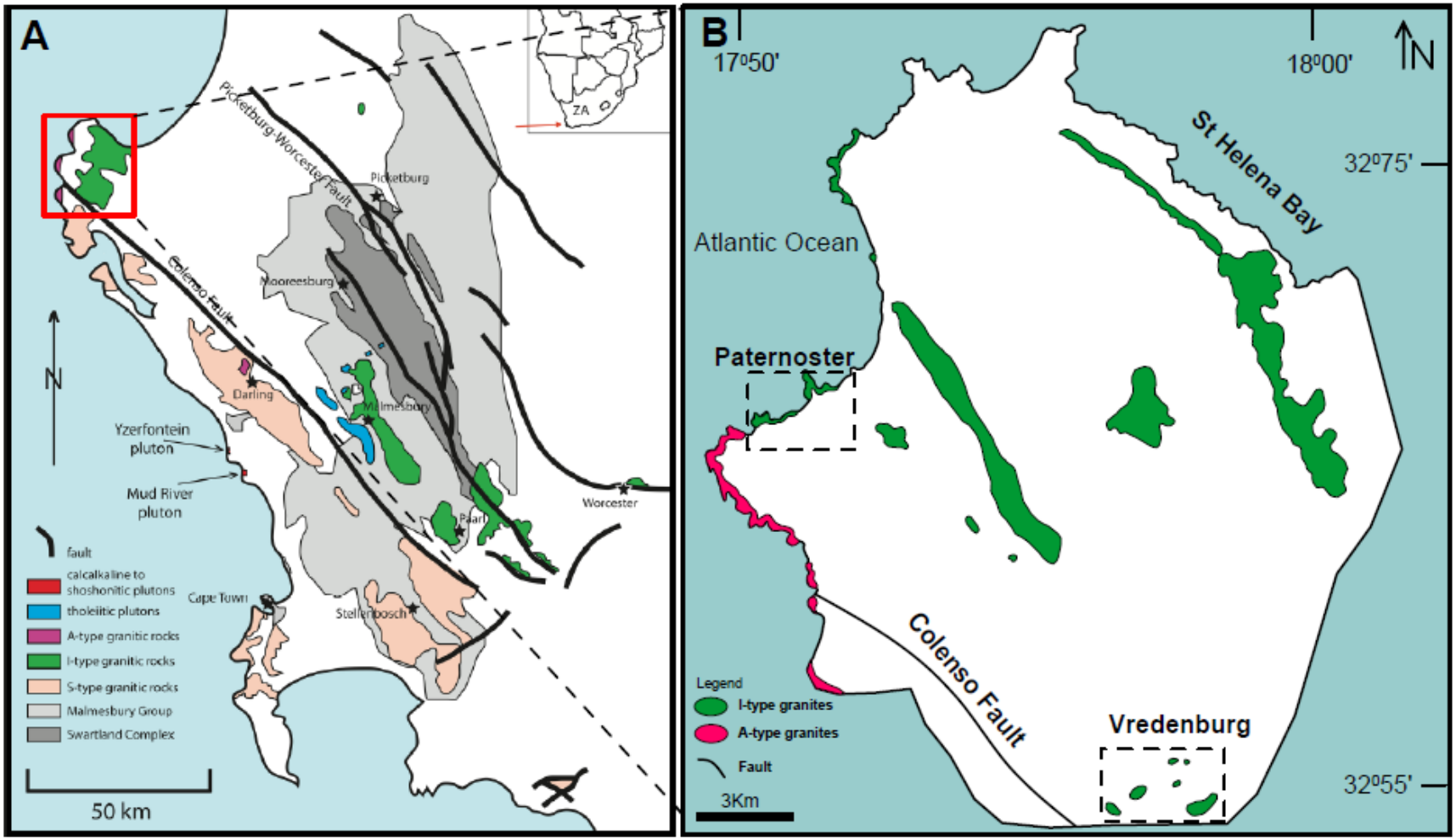

Figure 1.1: A) Sketch map of the west coast geology of South Africa, which shows the exposure of Malmesbury Group and Swartland Complex sedimentary host rocks, as well as the intrusive S–, I– and A–type granitic suites of the Cape Granite Suite (CGS) and its associated intermediate to mafic plutons (from Clemens et al. 2017d). The red arrow in the insert shows the location of the area within southern Africa (top right). B) Zoomed in red square in (A) which shows the I– and A–type granitic outcrops in and along the towns of Vredenburg and Paternoster modified after Siegfried (1981). The dashed squares indicate the area of interest for this study. For zoomed in maps within this study area see Chapter 4.

As for their tectonic setting, this has been constrained by structural and geochronological data (Kisters et al., 2002). However, these interpretations may benefit from additional geochemical substantiation using new and improved tectonic diagrams which use major and trace element discriminant functions (Verma et al., 2013). Thus, offering an additional aim for this investigation into the I−type granites of the Vredenburg batholith and ferroan Cape Columbine granites of the Cape Granite Suite along the south−western coast of South Africa. Whole−rock geochemical and Sr−Nd isotopic analyses were undertaken for both granitic bodies to better understand the petrogenesis of the I−type and ferroan (A−type) granites as well as constrain the sources and geotectonic settings of these rocks.

1.1) Petrogenesis models proposed for I−type and A−type granites

1.1.1) I−type granites

Processes that control the diversification of the chemistry in both S− and I−type granites are still somewhat enigmatic (Gao et al., 2014). Thus, many petrologists have postulated various models to describe the primary processes responsible for their chemical variation. The models have been grouped into two broad classes, namely 1) closed system magmatic chamber processes and 2) source−controlled processes (Garcia−Arias and Stevens, 2017). The former consists of more widely accepted processes, such as crystal fractionation, assimilation of wall−rock, and mixing of different magmas (Garcia−Arias and Stevens, 2017). These mentioned processes render the chemical diversity displayed by granitoids to be a function of internal processes of the magma itself (Zarrebini, 2016). The second class is comprised of the restite unmixing and peritectic assemblage entrainment models (White and Chappell, 1977; Stevens et al., 2007). These models of the latter class postulate that the chemical variability in granites is derived from the melting of the source material as well as the solids (peritectic or restite) that are entrained in the melt (Clemens et al., 2011; Clemens and Stevens, 2012). The aforementioned model groups have both drawn some degree of substantiation for each of them, however, there is still no firm consensus as to which process is the primary contributor to the variety of granites observed in a single pluton or batholith that exhibit I−type characteristics. Furthermore, each model from the two groups has their own limitations which further contribute to difficulties in determining the petrogenetic processes responsible for compositional variations.

The crystal fractionation model has been proposed by Bowen (1928) and in essence states that chemical and petrological variation in granitic magmas is due to early forming mafic minerals which crystallise and then separate from a mantle−derived basic magma, due to gravitational settling and/or other processes of kinetic isolation of crystals such that these are unable to re−equilibrate with the residual liquid as crystallisation continues (Clemens and Stevens, 2012; DePaolo, 1981; Gao et al.,

2016; Garcia−Arias and Stevens, 2017). Although not as evident as for, e.g., mafic−ultramafic layered intrusions support such gravitational driven processes exist in the form of concentrated layers of ferromagnesian minerals and mafic mineral cumulates (Garcia−Arias and Stevens, 2017). Also, the significance of this model implies that felsic magmas are the products of extensive mafic magma differentiation. However, Clemens et al. (2011) have highlighted the problems that arise from this model. If this process was the dominant one to produce the variety of granites in a single pluton, surely there would be a considerably large volume of a mafic component (e.g. gabbros) that would be observed with the granites, but no such suite has yet been located.

It has also been suggested that bulk wall−rock assimilation of crustal material entrained in the magma during its ascent from source to emplacement could be the cause of compositional variation (DePaolo, 1981). Field observations that drew petrologists to this idea were the abundance of metasedimentary xenoliths present in outcrops (Villaros, 2010; White and Chappell 1988). In its postulation it was suggested that a mantle-derived basic magma can obtain major, trace, and isotopic characteristics of a granitic magma by assimilation of crustal material. These chemical characteristics would be the product of either mineral disaggregation by xenoliths entrained in the magma or due to dissolution and crystallisation (Stevens and Clemens, 2012). This idea was challenged by Glazner (2007) who suggested that such a process would be energy limited. Glazner (2007) demonstrated that heat consumption of such processes would result in rapid cooling and a high degree of crystallisation of the magma. The resultant magma would be have such a high crystalline content (≈70%) that the magma becomes immobilised and further magmatic evolution is halted. Although, partial melts from the xenolith can contribute to hybridisation by mixing with the host magma, however, such processes would contribute to local chemical variation. Therefore, wall-rock assimilation has some substantiation on the basis of xenoliths observed in granite suites, however, it has been considered to be a secondary and local contributor for chemical variation in I−type granites (Clemens and Stevens, 2012).

In literature magma mixing or mingling is suggested to be one of the main contributors to chemical diversity in I−type granites (Clemens et al., 2011). The evidence for magma mixing is based on the presence of mafic microgranular enclaves (MME), often observed in granite suites. The origin of these MME is in many cases are thought to be mantle-derived basaltic magmas (Farina et al., 2012; Han et al., 2014; Villaros,2010). This suggests that there is some mantle−derived magma component associated with a felsic crustal magma. As demonstrated by Metcalfe et al. (1995) and Clemens et al. (2016) such processes can occur. However, Clemens et al. (2009, 2011) argues against this idea being the primary contributor for the chemical variation of granites on the basis that basaltic magmas don't exhibit the same chemical correlations (i.e. the tight linear trends between maficity (Fe + Mg) vs. Ti). .

Furthermore, evidence presented by Clemens et al. (2017b, c) to substantiate the argument of Clemens et al. (2009) suggests that the MMEs do not necessarily have to represent the progenitor of a mixing process that produced the host granite; rather they could have originated from a previously emplaced mafic magma (Clemens et al., 2017b). Therefore, the presence of MMEs, or lack thereof, does not necessarily represent a mantle−crust magma mixing process as a significant contributor to the geochemical diversification of granites (Clemens et al., 2011).

White and Chappell (1977) presented the restite unmixing model, which implies that granites are representatives of low temperature melts and varying degrees of entrainment of mineral assemblages (restites) that remains after anatexis. In addition, the model suggests that the entire source rock accompany the melt into shallow crustal levels, and that the chemical variation in the granites are due to the progressive melt separation and entrainment of restite mineral assemblages (Clemens and Stevens, 2012; Clemens et al., 2011; White and Chappell, 1988).. Clemens and Wall (1981), Wall et al. (1987) and Clemens and Mawer (1992) argued against this model, specifically against the petrological, physical and chemical characteristics that are implied by the model. Moreover, Clemens and Stevens (2012) expresses the lack of textural and mineralogical field evidence. Therefore, the model has come under a lot of scrutiny and has generally not received acceptance by petrologists.

More recently, Stevens et al. (2007) postulated a revised model of restitic entrainment that could be responsible for chemical variation in granites, namely peritectic assemblage entrainment (PAE). The gist of the model is that the geochemical diversity of granites can be explained by the entrainment of peritectic phases (in small grain sizes) in the partial melt that is carried along from the source (Clemens, 2012; Stevens et al., 2007). Peritectic phases are mafic minerals that are produced during incongruent melting of hydrous phases such as biotite and hornblende (Clemens et al., 2011; Clemens, 2012). As demonstrated by Stevens et al. (2007), experimentally melting various source compositions would result in purely felsic melts which cannot account for the ferromagnesian components observed in granite suites. Therefore the high concentrations of Fe and Mg must come from another source, which was speculated to be the peritectic phases. The model was used to explain the variations in chemistry displayed by S−type granites, however, Clemens et al. (2011) have extended the model to I−type granites. Moreover, Clemens et al. (2011), Clemens and Stevens (2012) and Villaros et al. (2009a, b) have stated that PAE is the most compatible model which can explain chemical diversity observed in granites from the post−Achaean. This deduction was made on the basis of the trends of the major− and trace−elements when plotted against maficity (Fe + Mg, cation) (Stevens et al., 2007; Villaros et al., 2009b). Tight linear positive correlations are observed for the chemical parameters of certain peritectic phases, such as biotite (e.g. titanium (Ti)) which attests to the stoichiometry of biotite melting at high

temperatures (Zarrebini, 2016). Moreover, it was suggested that coupled melting of biotite and hornblende would produce clinopyroxene which is able to explain the trends of calcium and the aluminum saturation index (ASI) vs. maficity (Farina et al., 2012). These trends are an intrinsic feature of PAE (Clemens et al., 2011). Additionally, trace element trends, such as those of the high field strength elements (HFSE) and light rare earth elements (LREE), are attributed to the entrainment of zircon and monazite (Villaros et al., 2009b). Typically trace elements associated with zircon (Zr and Hf) and monazite (Ce, Th, LREE.) show similar trends to the reactants produced by peritectic phases (Villaros et al., 2009b). This trace element trend is further proof of the entrainment of certain phases from the source. Therefore, this model has been argued for rather successfully. Although PAE can explain chemical variation in I−type granites considerably well, it is not necessary to exclude closed chamber processes as it has been demonstrated that granitic magma can be produced by many different processes. To be noted, this section only covers what is considered to be the main petrogenetic processes and some of which will be investigated later. For a full description of other processes see Clemens and Stevens (2012).

1.1.2. A−type granites (ferroan)

In the case of ferroan granites, they are believed to be associated with upliftment or extensional tectonic settings (anorogenic) (Whalen et al., 1987). They are characterised by high total alkali contents, high Fe/ (Fe + Mg) ratios, high REE, Zr, Nb and Ta, and otherwise low trace element contents (Frost and Frost, 2011). Moreover, ferroan granites have been grouped into two types, namely A1, which was allied to oceanic island basalts (OIB), and A2 that reflect similar characteristics to subduction or collision zones, on the basis of their trace element chemistry (Eby, 1990, 1992). Moreover, the source−type classification scheme of Eby (1990, 1992) revolutionised the way ferroan granites are viewed as they were no longer restricted to only anorogenic processes. Despite the many schemes, there is still no general consensus as to the sources and petrogenetic process involved in ferroan granite genesis (Sun et al., 2015). The most prevalent processes deemed to be responsible for the chemical diversity in ferroan granites are: 1) fractionation of mantle−derived magmas (Anderson et al., 2003; Frost and Frost, 1997, 2008, 2011; Moreno et al., 2014), 2) partial melting of various crustal sources that have been depleted by hydrous felsic melts (Frost and Frost, 2011; Sun et al., 2015; Whalen et al., 1987) and (3) a combination of the first two models, in which differentiating basaltic magmas assimilate crustal rocks.

Fractionation of mantle−derived basaltic magma with or without crustal contamination has been postulated to be the significant process in ferroan granite magmatism (Frost and Frost, 2011). Barker et al. (1975) investigated the ferroan granites of Pikes Peak Batholith, USA, and speculated that the crustal component might be from a granulitic lower crust. Collins et al. (1982) extended this idea and suggested that melting of such a crustal component alone would produce ferroan granitic magmas on the basis that melting of a granulitic source in vapour−absent conditions would create water deficient melt containing halides and large, high charge cations that are a typical feature of ferroan granites (Frost and Frost, 2011). However, Creaser et al. (1991) refuted this hypothesis, arguing that if that were the case the melts would have lower concentrations of K, silica (SiO_2) and Fe/Mg ratios than their progenitor. Moreover, Frost and Frost (1997) proposed that the fractionation of basaltic magmas without a crustal component could be the ideal process to produce ferroan magma. Evidence of this was provided by rhyolitic bodies which have similar geochemical characteristics as ferroan granites located in tholeiitic volcanoes from oceanic islands that were several kilometers from any continental crust component. It was speculated that the rhyolitic magma had to have been produced by extreme fractionation of the tholeiitic magma (Frost and Frost, 1997, 2008). In addition, Frost and Frost (1997) showed that tholeiitic rocks typically crystallise in reducing environments where oxygen fugacity levels are of log 1 or 2 units below the FMQ buffer and that, therefore, magnetite crystallisation is late. This late crystallisation of magnetite is responsible for the high Fe concentrations at high SiO_2 values observed in ferroan granites (Osborn, 1956; Frost and Frost, 2011). Moreover, the lithochemical evolution of basaltic magmas supports this hypothesis (Frost and Frost, 2011), in particular, with respect to the modified alkali lime−index (MALI) variation. Initially, at low SiO_2 contents, basalts exhibit high MALI values. As differentiation occurs the MALI values of basalts tend to cross all the alkalic, alkali−calcic, calc−alkalic and calcic boundaries defined by the MALI plot. This trend is controlled by plagioclase crystallisation (Frost and Frost, 2008). Therefore, based on experimental and field geochemical data differentiation is an important contributor to ferroan granite genesis.

Partial melting of crustal rock is invoked to be responsible for the compositional variation in ferroan granites (Frost and Frost, 2011). Experimental ferroan melts were produced by melting magnesian tonalite gneiss with unequal amounts of hydrous minerals (Skjerlie and Johnson, 1993). Moreover, Frost and Frost (2011) redid a melting experiment by Patiňo Douce (1997). These studies showed that melting magnesian tonalite and, granodiorite with equal hydrous mineral abundance at low pressures produces ferroan granites, however, the produced melts would be enriched in calcium relative to natural ferroan magmas. The significance of this experiment was to show that ferroan granites can be

produced by dehydration melting processes at low pressures, reflecting geological constraints that would be expected in extensional environments.

Lastly, although the models of differentiation of tholeiitic magmas and partial melting of certain crustal rocks at low pressures are adequate to produce ferroan melts, many petrologists suggest that instead of viewing these processes as isolated systems, they should, instead, be viewed as co−magmatic processes, where both models are crucial in ferroan melt production (Frost and Frost, 2011). These speculations come from the observed chemistry in natural ferroan suites (Hill et al., 1996; Moreno et al., 2014). Moreover, Hill et al., (1996) demonstrated that the ferroan granites of the Lebowa Granite Suite, Bushveld Complex, which have been produced by extreme differentiation of basaltic magmas, have chemical signatures that are related to partial melting of the crust. Furthermore, ferroan granites are characterised by high−temperature melts (> 900 °C) in extensional environments (Creaser et al., 1991; Haapala and Rämö, 1990). In addition, to obtain such high temperatures in the crust, there has to be a mantle−derived magmatic influence, such as mantle underplating (Haapala and Rämö, 1990). Based on these tectonic conditions Frost and Frost, (2011) speculate that fractionation of basaltic magmas ascending through the crust will have sufficient energy and temperature to melt the surrounding wall rock.

Chapter 2 Geological Setting

2.1 Introduction

The Neoproterozoic−Cambrian Saldania Belt (SB) represents a local segment of the Pan−African Orogenic Belts that formed during the construction of Gondwana (Rozendaal et al., 1999). It is separated into two branches; 1) a southern branch comprised of the Kango, Gamtoos and Kaaiman Groups, exposed as inliers within E−W trending mega−anticlinal folds within the Permo−Triassic Cape Fold Belt and 2) a NW−SE trending western branch composed of the Malmesbury Group and Klipheuwel Group (Rozendaal et al., 1999; Belcher and Kisters, 2003; Chemale et al., 2011; Frimmel et al., 2013) (Fig. 2.1). Syn− to post−orogenic granitoids of the Cape Granite Suite (CGS) intruded the Malmesbury (Western Branch) and Kaaimans Groups during the Saldanian Orogeny (Fig. 2.1) (Scheepers, 1995; Rozendaal et al., 1999; Frimmel et al., 2013).

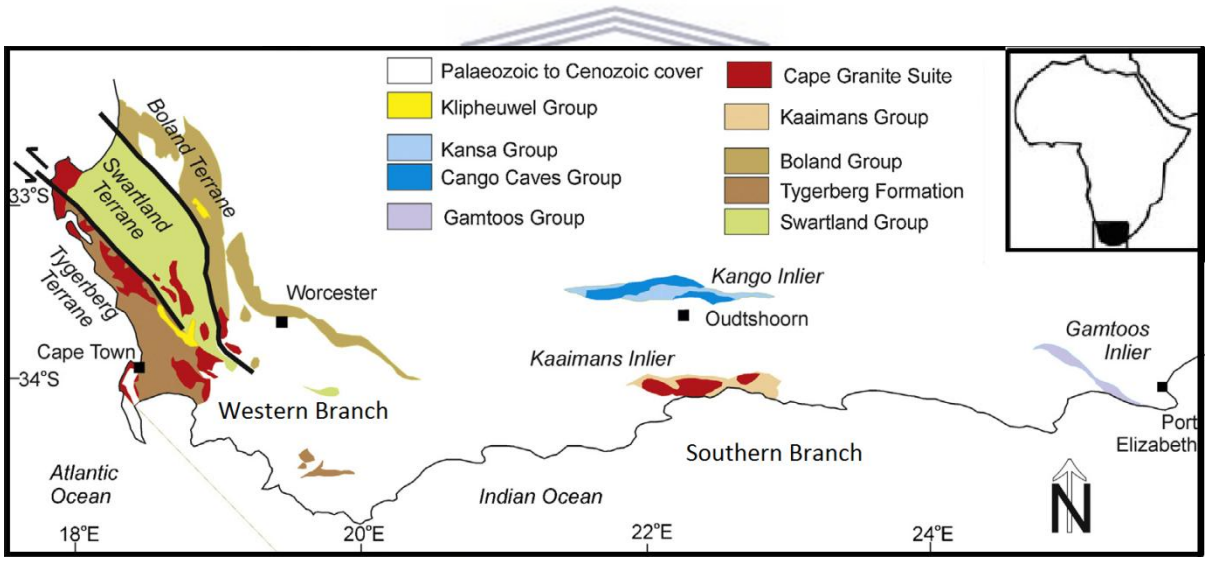

Figure 2.1: Regional geological map of the Saldania Belt and its branches from (Frimmel et al., 2013), modified after (Gresse et al., 2006)

2.2 Regional Geology

2.2.1) Western Branch of the SB

Three partly conflicting geodynamic models for the formation of the western branch of the SB are summarised in Table 2.1 (after Hartnady et al., 1974; Rozendaal et al., 1999; Belcher and Kisters, 2003; Frimmel et al., 2013). According to Hartnady et al., (1974) the Malmesbury group is separated into three terranes, namely, from southwest to northeast, the Tygerberg, Swartland and Boland

terranes, which are bounded by NW− SE trending strike−slip faults, including the Colenso Fault separating the Tygerberg and Swartland terranes, and the Piketberg−Wellington Fault separating the Swartland and Boland terranes (Fig. 2.1). Belcher and Kisters (2003) suggested a model that recognises three groups unconformably stacked on top of each other, namely, from oldest to youngest, the Swartland, Malmesbury, and Klipheuwel Groups.

More recently, a model by Frimmel et al., (2013), recognises two terranes, namely the Malmesbury Terrane and the Boland Zone (terrane) (Fig. 2.2), the former terrane being a combination of the previous Tygerberg and Swartland terranes. The latter model only recognises the Piketberg−Wellington Fault as a terrane boundary, whereas the Colenso Fault is considered to be a reactivated deeper ancient basement structure.

Table 2.1: Summary of the conflicting geodynamic schemes for the western branch of the Saldania Belt according to Belcher and Kisters (2003), Gresse et al. (2006), Frimmel et al. (2013) and Hartnady et al. (1974).

Hartnady et al. (1974) &Gresse et al. (2006)				**Belcher and Kisters (2003)**		**Frimmel et al. (2013)**		
Group	Subgroup	Formation	Lithology	Group	Formation	Group	Formation	Age (m. y.)
Boland Terrane Klipheuwel Malmesbury	 Boland	Populiersbos Magrug Brandwacht Porterville Noree Piketberg	Shale/Phyllite Sandstone/Conglomerate Greywacke/Volcanics/congl Shale/Phyllite Sandstone/Volcanics Sandstone/Congl.	Klipheuwel	Populiersbos Magrug Franschhoek	Klipheuwel	Populiersbos Magrug Franschhoek	 <551 >552
Piketberg-Wellington Fault				**Unconformity**		**Unconformity**		
Swartland Terrane Malmesbury	 Swartland	 Franschhoek Bridgetown Moreesburg Klipplaat Berg River	 Sandstone/Congl. Mafic volcanics/Dolomite Greywacke Sandstone Greywacke	Malmesbury	Porterville Tygerberg Piketberg	**Boland Zone** Boland	Brandwacht Porterville Noiree/Piketberg **Unconformity** Bridgetown	540 550 800
Colenso Fault				**Unconformity**		**Piketberg-Wellington Fault**		
Tygerberg Terrane Malmesbury		Tygerberg	Greywacke/Mafic volcanics	Swartland	Moreesburg Bridgetown Berg River	**Malmesbury Terrane** Malmesbury	Moreesburg/ Tygerberg Klipplaat Berg River	>552 <554

The Malmesbury Terrane, as defined by Frimmel et al. (2013; Fig. 2.2) includes a basement succession of greywacke from the Berg River Formation overlain by quartz−sericite−chlorite schist with limestone and sandstone interbedding, which is overlain by interlayered greywacke and phyllite of the Moreesburg/Tygerberg Formations (Rozendaal et al., 1999; Frimmel et al., 2013). Similar lithostratigraphic successions of greywacke along the Colenso Fault of the Moreesburg and Tygerberg Formations in the southwest of the Malmesbury Terrane are indicative that the Colenso Fault is not a terrane boundary (Frimmel et al., 2013). Associated with the Malmesbury Terrane is a local andesitic volcanic succession termed the Bloubergstrand Member (Rozendaal et al., 1999). The Boland Terrane is composed of, from oldest to youngest, the Piketberg/Noiree, Porterville, and Brandwacht Formations which are indicative of a delta or nearshore environment which is unconformably overlain by coarse-grained, proximal detritus sediments from the Klipheuwel Group (Theron et al., 1992; Rozendaal et al., 1999; Frimmel et al., 2013).

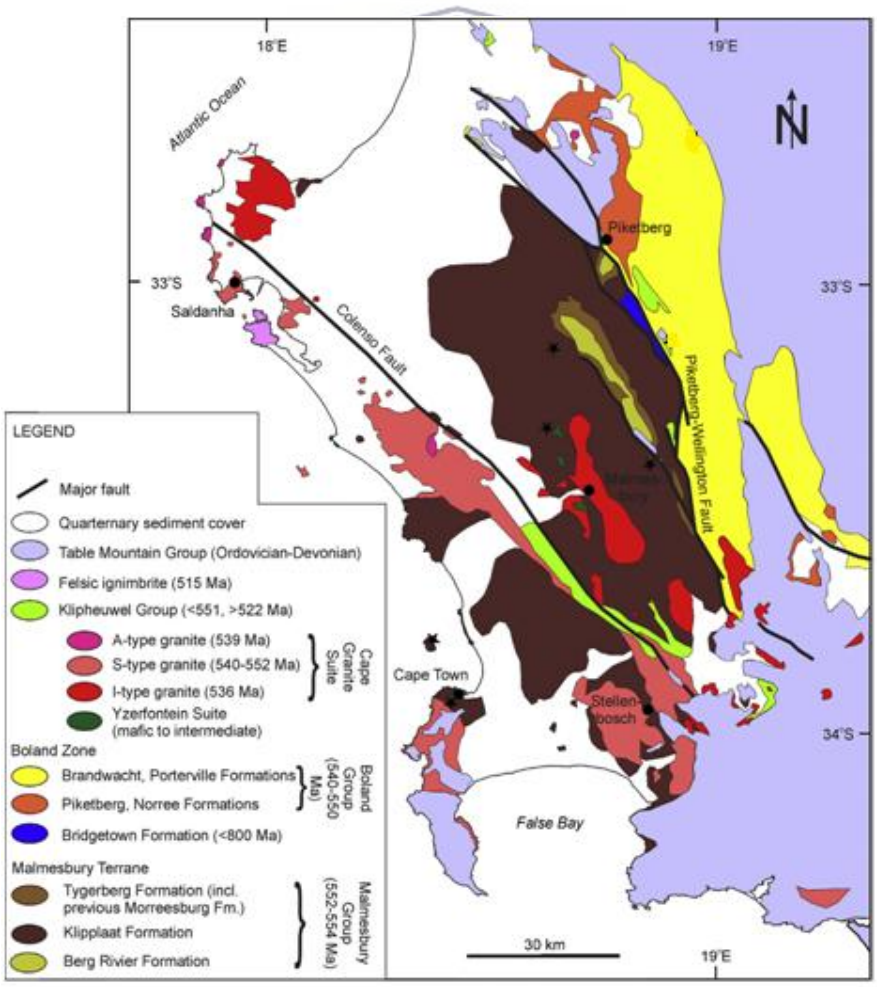

Figure 2.2: A simplified geological map of the western branch of the Saldania Belt (Malmesbury Group) and granite intrusions of the Cape Granite Suite. From Frimmel et al. (2013)

Deformation in the southwestern portion of the Malmesbury Group (previously known as the Tygerberg Terrane) resulted in a widespread NNW−SSE striking sub-vertical cleavage and open to tight, upright folding (Belcher and Kisters, 2003; Rowe et al., 2010; Frimmel et al., 2013). Polyphase deformation towards the core of the Malmesbury Group developed an early, subhorizontal S_0/S_1 transposition foliation (D_1), associated with S_1−parallel quartz veins and tight− to isoclinal folding of S_2 (D_2), and open− to tight re−folding with a sub-vertical axial planar cleavage (D_3) which is prominent across the Malmesbury Terrane (Rozendaal et al., 1999; Belcher and Kisters, 2003). D_2 coincides with the main deformational phase of the Pan−African thrusting (Hartnady et al., 1985). D_4 is indicated by southwest− or northwest−plunging kink bands that cross cut D_2 and D_3 fold axes which plunge to the northwest or southeast (Frimmel et al., 2013). A sub−greenschist facies metamorphic overprint and weakly deformed NW−SE folding are present in the Boland Zone (Belcher and Kisters, 2003; Frimmel et al., 2013).

The main structural features of the Malmesbury Group are the NNW−SSE trending strike−slip faults (Fig. 2.2), namely, the Colenso Fault and the Piketberg−Wellington Fault. The Colenso Fault is a poorly exposed, continuous fault extending ~150 km parallel to the Atlantic Coast defined by mylonitic and brecciated outcrops along the NW−SE extent of the fault (Theron et al., 1992; Kisters et al., 2002; Belcher and Kisters, 2003). Kisters et al. (2002) suggest that the sense of shear of the Colenso Fault was initially sinistral based on the emplacement and deformation of gneissose granitoids of the Darling Batholith (~547± 7Ma). Following the emplacement of the Darling granites, the fault reversed to dextral shearing at ~539 ± 4 Ma with dextral movement continuing until ~520 Ma. These age constraints are based on the emplacement and deformation features of the Trekoskraal and Cape Columbine granites, respectively. The reversal of the Colenso Fault has been tentatively correlated with the main uplifting of the Malmesbury Group which occurred in a transtensional or extensional setting (Kisters et al., 2002).

2.2.2) Cape Granite Suite (CGS)

Granitoids of the CGS intruded the Malmesbury Group in four phases (Table 2.2) during the late Neoproterozoic and early Paleozoic eras (555 – 510 Ma) (Scheepers and Armstrong, 2002). These granitoids are exposed within the Malmesbury Group (Rozendaal et al., 1999). The felsic magmatic events are characterised based on their variable internal structures, their relationship with the country rock, nature of magmatic enclaves, mineralogy and geochemical characteristics (Scheepers and Armstrong, 2002).

Table 2.2: Summary of our current understanding of the magmatic events of the Cape Granite Suite which intruded the Malmesbury Group during the late Neoproterozoic to early Cambrian, from youngest to oldest (after Clemens et al., 2017d; Scheepers and Armstrong, 2002).

Felsic magmatic events in the Saldania Belt			
Magmatism	Association	Rock type	Examples
Phase IV (520 Ma)	Aa	Alkali feldspar granite, quartz syenite	Klipberg granite
	Ab	Alkali feldspar granite	Cape Columbine granite
Phase III (540–520 Ma)	Ib	Granite, alkali feldspar granite	Paarl fine grained granite and Slippers Bay granite
	Ia	Monzogranite, granite, alkali feldspar granite	Paarl coarse- and medium-grained granite, Vredenburg monzogranite and Greyton pluton.
Phase II (538 Ma)	Volcanic	Ignimbrite, tuffisite, quartz porphyry	Postberg ignimbrite, Saldanha quartz porphyry
Phase I (555–540 Ma)	Sb	Granite	Trekoskraal granite, Karnberg granite, Rondeberg Granite and coarse porphyritic Darling granite
	Sa2	Granite, alkali feldspar granite	Stellenbosch fine grained granite, Contreberg granite and Olifantskop granite
	Sa1	Granite	Hoedjiespunt granite, Seeberg granite, and Peninsula granite

Phase I, which is the oldest of the granitoid intrusives, are the syn- to late-tectonic granites found mainly in the south-western section of the Malmesbury Terrane (Scheepers 1995; Scheepers and Armstrong, 2002; Frimmel et al., 2013; Fig. 2.2). They are peraluminous to metaluminous S-type granites to granodiorites (Scheepers and Armstrong, 2002). The metaluminous Sb granite intrusions close to, or along the Colenso Fault concluded phase I magmatism (Scheepers and Armstrong 2002). At the end of phase I there was a transition from S-type to I-type granites indicated by the amphiboles present in the Sb granites (Siegfried, 1981; Scheepers and Armstrong, 2002). However, before the I-type magmatism commenced there was a volcanic production of Phase II (Clemens et al., 2017a), consisting of peraluminous S-type volcanic and subvolcanic rocks found in the Malmesbury Terrane (Frimmel et al., 2013; Scheepers and Armstrong, 2002). They are characterised by rhyolitic to

rhyodacitic peraluminous felsic rocks occurring as ignimbrite flows, quartz porphyritic granites and tuffsites (Clemens et al., 2017d; Scheepers and Armstrong, 2002). Phase III is composed of late− to post−tectonic I−type granites located in the north−western portion of the Malmesbury Terrane and the Boland Zone (Frimmel et al., 2013; Rozendaal et al., 1999; Scheepers and Armstrong 2002). The metaluminous to slightly peraluminous I−type granites are grouped into two associations, namely Ia consisting of monzogranites and granites, and Ib composed of alkali feldspar granites (Scheepers and Armstrong, 2002). Xenoliths present in the I−type granites are of sedimentary, and igneous to meta−igneous origins (Scheepers and Armstrong, 2002). Finally, Phase IV saw the conclusion of the CGS magmatism. This phase is defined by A−type granites found in the Malmesbury Terrane (Scheepers 1995; Scheepers and Armstrong, 2002; Frimmel et al., 2013). The initial stages of granitoid intrusion had a high−K calc−alkaline composition becoming more intermediate at the final stages of magmatism (Scheepers, 1995; Scheepers and Armstrong, 2002). These granites are separated into two associations, including the Aa−type composed of amphibole quartz syenite to biotite quartz syenite and alkali feldspar granite with sedimentary xenoliths present, and Ab composed of alkali feldspar granites (Scheepers and Armstrong, 2002).

2.3) Local Geology

2.3.1) Vredenburg Batholith

The Vredenburg Batholith forms the northwestern most pluton of the CGS. It outcrops along the coasts of Paternoster and St Helena, with large masses inland around the town of Vredenburg. The area has been mapped in detail by Siegfried (1981). The granitoids composition varies from granite, through quartz monzonite to alkali feldspar granite (Scheepers, 1995). It has a well−defined magmatic lamination, defined by alkali feldspar megacrysts (Kisters et al., 2002). Furthermore, it has a modal mineral assemblage of quartz, plagioclase and alkali feldspar and, mafic mineral assemblages of biotite, hornblende, and ilmenite (Siegfried, 1981). The Vredenburg Batholith, according to Siegfried (1981) and Scheepers (1995), is typically CaO− and K_2O−rich and metaluminous−peraluminous in composition with silica contents around 68 – 74% (Scheepers, 1995). Scheepers (1995) classified them as shoshonitic due to their high alkali values; furthermore, there is typically a decrease in Zr with increasing differentiation. The granitoids are moderately LREE-enriched with La_N/Yb_N values of ≈5.8−6.1. Eu anomalies are strong to moderate (Eu/Eu*=0.33−0.52) when normalised to chondritic values (Scheepers, 1995).

2.3.2) Cape Columbine Granites

The Cape Columbine Nature Reserve was built on a magmatic intrusion, the final phase of the Cape Granite Suite, being the Phase IV post−tectonic A−type granites, and more specifically the Ab association, Cape Columbine granites, exposed at the NW end of the Colenso Fault (Clemens et al., 2017d Scheepers, 1995; Scheepers and Poujol, 2002; Kisters et al., 2002). The Cape Columbine Granite is pink− to greyish in colour, coarse− to medium− grained, composed of, in decreasing order alkali−feldspar, plagioclase, quartz along with biotite and accessory amounts of tourmaline, zircon, and apatite (Kisters et al., 2002). Several sub-vertical, NNW−SSE trending cataclasites, and mylonitic zones cut across the area of Paternoster (Siegfried, 1981; Kisters et al., 2002). A weak sub-vertical NW trending foliation fabric and well-defined west dipping foliation are developed in the Cape Columbine Granite and Vredenburg monzogranite, respectively (Kisters et al., 2002). Scheepers (1995) described the main chemical features of the pluton. They typically display an aluminum saturation index which varies from peralkaline to metaluminous. They are enriched in alkalis as well as Thorium (Th). Lastly, their REE profiles are more LREE−enriched than the Vredenburg Batholith (La_N/Yb_N=11) and they have an Eu anomaly value of [Eu/Eu*=0.23]. Their REE profiles are unique in that they are enriched in the HREE, especially Yb, with slightly lower values of Dy, Ho, and Er (Scheepers, 1995).

Chapter 3 Methodology

The area of study is located along the north-western section of the Saldania Belt. A small scale mapping of the areas of interest was done. In addition, rock samples were collected to investigate the geochemical, petrographic, and, structural features of the I− and A−type granites outcropping mainly along the coast of Paternoster and inland around the town of Vredenburg (Vredenburg Batholith) and, along the coast of the Cape Nature Reserve (Cape Columbine Granite), respectively. Analyses used for this research include; transmitted light microscopy, X−Ray Fluorescence (XRF) Spectrometry, Laser−Ablation Inductively Coupled Plasma Mass Spectrometry (LA−ICPMS) and a variety of computer software.

3.1 Mapping

New maps of the area of research were produced for this study on rocks previously mapped as I− and A−type granites of the Cape Granite Suite (e.g. Scheepers, 1995; Rozendaal et al., 1999) in the north-western section of the Saldania Belt. Google Earth™ images were used as a base to create rough maps, which were digitised using Surfer 11™ software.

3.2 Sampling and Petrography

In total 66 samples were collected, the majority of those from within the Vredenburg Batholith (58 samples). These samples consist of the main host porphyritic granite (28), igneous enclaves (15), sheared host rock material (5), xenoliths (Malmesbury shales, 10) a sample of mafic dike and an aplitic vein. Due to the rounded shape of the granite outcrops, the hammering out of samples was difficult. This resulted in a minimal number of samples collected for the mafic dikes, xenoliths and a variety of enclaves (Igneous enclaves 2 (IE2), see following chapters) hosted in the granite. The rocks which were difficult to sample, as well as the sheared rocks, are not the focus of this study and were not analysed for their geochemical properties. Moreover, IE2−type enclaves were not analysed petrographically either. 8 samples were collected from the Cape Columbine Granite consisting of equigranular coarse-grained granites.

Polished thin sections were prepared at the Department of Earth Sciences at the University of the Western Cape for the granites and at Continental Instruments in India for the igneous enclaves (IE1) and, country rock xenoliths. Thin sections were analysed by a Leica transmitted light microscope to determine the modal assemblages and textural (including structural) features.

3.3 Whole−rock geochemistry

3.3.1 Major element compositions

Whole rock analyses were done on fresh rock samples that were crushed by a stainless steel crusher and milled in a Sieb ring tungsten−carbide mill for 5 minutes. Milling samples with a ring mill resulted in contamination of Cr_2O_3 which has been reflected in the geochemical analysis and, therefore, this element has not been reported. The milling bowl was cleaned with quartz and wiped down with acetone after milling each sample to avoid cross-contamination.

Whole-rock analysis was carried out on 43 samples (35 from the Vredenburg Batholith; 23 granite samples and 12 igneous enclaves, and 8 from the Cape Columbine Granite samples) at the Central Analytical Facilities (CAF) at Stellenbosch University. Loss on ignition was calculated first. This was done by placing sample material in a porcelain crucible then placing it in an oven with a temperature of 1000°C for 1 hour. The major element concentrations of the samples were then determined using XRF analysis on fusion glass beads produced from ultra-pure flux (lithium tetra− and meta−borate and, lithium iodide) mixed with 1g of anhydrous sample material. XRF spectrometry was performed using an Axios Wavelength Dispersive spectrometer from PANalytical with a 2.4kW Rh X−ray tube. Standards used for granites include national (SARM®) standard, NIM−G.

3.3.2 Trace element compositions

Trace element compositions were determined by Laser−Ablation Inductively Coupled Plasma Mass Spectrometry (LA−ICPMS) at CAF. Fusion disks used for XRF analysis were coarsely crushed and mounted along with up to 12 other samples in a 2.4cm round resin disk. The mount was mapped and then polished for analysis. The instrumentation set up includes a Resolution 193nm Excimer laser from ASI connected to an Agilent 7700 ICP−MS. For traces in fusion disks, 2 spots of 100µm are ablated on each sample in helium (He) gas with a flow rate of 0.35L/min, mixed with argon (Ar) (0.9L/min) and nitrogen (N) (0.009L/min) just before being introduced into the ICP plasma. The system operated at 2mJ energy and 10Hz frequency. Quantification was done using NIST 612 for calibration and the % SiO_2 from XRF measurement as an internal standard, using standard – sample bracketing. Two replicate measurements were made on each sample. The calibration standard was run every 12 samples. A quality control standard is run at the beginning of the sequence as well as with the calibration standards throughout. BCR−2 or BHVO 2G, both basaltic glass certified reference standards produced by the United States Geological Society (USGS) (Dr Steve Wilson, Denver, CO 80225), is used for this purpose. A fusion control standard from certified basaltic reference material (BCR−2, also from the USGS) is also analysed at the beginning of a sequence to verify the effective ablation of fused

material. Data processing was done using Iolite V3.32 software obtained from the University of Melbourne –School of Earth Sciences 2016.

3.4 Isotopes

Six samples, two from each rock type, were analysed for radiogenic isotopic ratios for Rb−Sr and Sm−Nd at the Department of Geological Sciences, University of Cape Town (UCT). The determination of Rb, Sr, Sm and Nd concentrations in the sample was performed on a PESCIEX Elan 6000 ICP-MS at UCT following dissolution and dilution with 5% HNO_3 containing an internal standard, with concentrations determined in duplicate for each sample. The international standard BHVO-2 was analysed with every batch of samples as a measure to achieve accuracy and precision. The background compositions were measured and the instrumental mass fractionation was corrected using the exponential law and fractionation factors based on the measured $^{86}Sr/^{88}Sr$ and $^{146}Nd/^{144}Nd$ ratios. For the assessment of instrument tuning and stability, the Sr solution of the NIST SRM987 Sr isotope standard and the Nd solution of the JNdi-1 Nd isotope standard were analysed twice prior to any samples and after every fifth sample. The external, measured σ_2 reproducibility of the SRM987 and JNdi- 1 standards were determined on the average $^{87}Sr/^{86}Sr$ and $^{143}Nd/^{144}Nd$ ratios, respectively. The $^{87}Sr/^{86}Sr$ data were reported and normalized to 0.710255 and $^{143}Nd/^{144}Nd$ data normalized to 0.512115. The initial $^{87}Sr/^{86}Sr$ and $^{143}Nd/^{144}Nd$ ratios were calculated using decay constants of 1.42 x 10^{-11} y^{-1} (Steiger and Jäger, 1977) and 6.54 x 10^{-12} y^{-1} (Begemann et al., 2001), respectively. The samples were subjected to HF and HNO_3 acid digestion. The separation of Sr and Nd isotopes were undertaken by chromatographic techniques as described by Miková and Denková (2007), after that described by Pin and Zalduegui (1997) and Pin et al. (1994). All isotope analyses are performed on a NuInstruments NuPlasma HR in the AEON EarthLab, housed in the Department of Geological Sciences, UCT, South Africa. Sr was analysed as a 200ppb 0.2% HNO_3 solution. The NIST SRM987 reference standard was used. A normalising value of 0.710255 for $^{87}Sr/^{86}Sr$ was used. The average $^{87}Sr/^{86}Sr$ values for the SRM987 standard for these analyses was 0.71083±11 (n = 6). The international rock standard BHVO-2 gave a value of 0.703473±20 relative to a value of 0.703479±20 reported by Weis et al. (2006). The long-term UCT average is 0.703487±32 (n = 124). All Sr isotope data was corrected for Rb interference using the measured signal for ^{85}Rb and the natural $^{85}Rb/^{87}Rb$ ratio. Instrumental mass fractionation was corrected using the exponential law and a $^{86}Sr/^{88}Sr$ value of 0.1194. Nd isotopes were analysed as 50 ppb 2% HNO_3 solutions using NuInstruments DSN-100 desolvating nebuliser. JNdi-1 was used as a reference standard, with a $^{143}Nd/^{144}Nd$ normalizing value of 0.512115±7 using the methodology of Tanaka et al. (2000). The average $^{143}Nd/^{144}Nd$ ratios for the JNdi-1 reference for these analyses is 0.512074±22 (n = 6). For the same standard Tanaka et al. (2000) reported a value of 0.512115±7. All

Nd isotope data is corrected for Sm and Ce interference using the measured signal for ^{147}Sm and ^{140}Ce, and the natural Sm and Ce isotope abundances. Instrumental mass fractionation was corrected using the exponential law and a $^{146}Nd/^{144}Nd$ value of 0.7219.

3.5 Geochemical Plots

All plots for modeling were produced using GCDkit software 4.1 (Janoušek et al., 2006). Tectonomagmatic discriminant functions were calculated using TecDia java software (Verma et al., 2013).

Chapter 4 Lithological Description

4.1 Introduction

Chapter 4 contains the lithological description of the rocks observed in the field of the area of study. Lithological descriptions of the rocks will be a composite of their field description and petrographic features. The layout of this chapter will be as follows: A *heading* which groups the rocks to the pluton or batholith to which they belong, e.g. Vredenburg Batholith, according to how they were mapped in this study and by previous authors (e.g. Scheepers, 1995; Siegfried, 1981), followed by a *subheading* indicating the rock type from the group to which it belongs (e.g. Granites). The structure of this chapter is as follows, a brief introduction will be given of the pluton or batholith after each heading and, the subheading sections will contain the field descriptions, petrography and, lastly, a summary of all the rock types of significance will conclude the chapter. To be noted, as mentioned in the previous chapter, the difficulty in sampling hindered petrographic and geochemical studies to be done on some of the xenoliths and igneous enclaves. Therefore, in the petrographic section with subheading "*Igneous enclaves"* the microphotographs contain images of only the coarse−grained, porphyritic variety of igneous enclaves (IE1).

4.2) Vredenburg Batholith

The Vredenburg Batholith in the field occurs as irregular outcrops that are exposed in and around the town of Vredenburg and its residential areas, across farms and, along the coastlines of Paternoster to the Cape Columbine nature reserve and St Helena Bay separated by either ocean or beaches, rather than what previous studies mapped as a single large outcrop (Scheepers, 1995). The rocks comprising the Vredenburg Batholith have been classified as monzogranite, granite and alkali feldspar granite. For this study, three main areas of granites along the coastal village of Paternoster and the Cape Nature Reserve (Fig. 4.1) and, those located in the town of Vredenburg (Fig. 4.2) were investigated. Moreover, the predominant rock type mapped was granite. The granites mapped contain entrained rock fragments (enclaves), namely country rock meta−sedimentary xenoliths (from the Malmesbury Group) and various intermediate to felsic igneous enclaves (IEs). The size of outcrop varies, with some ranging from tens of meters to well over hundreds of meters squared. The surfaces of the outcrops are weathered and appear pinkish to light grey and exhibit prominent magmatic structures (Fig. 4.3).

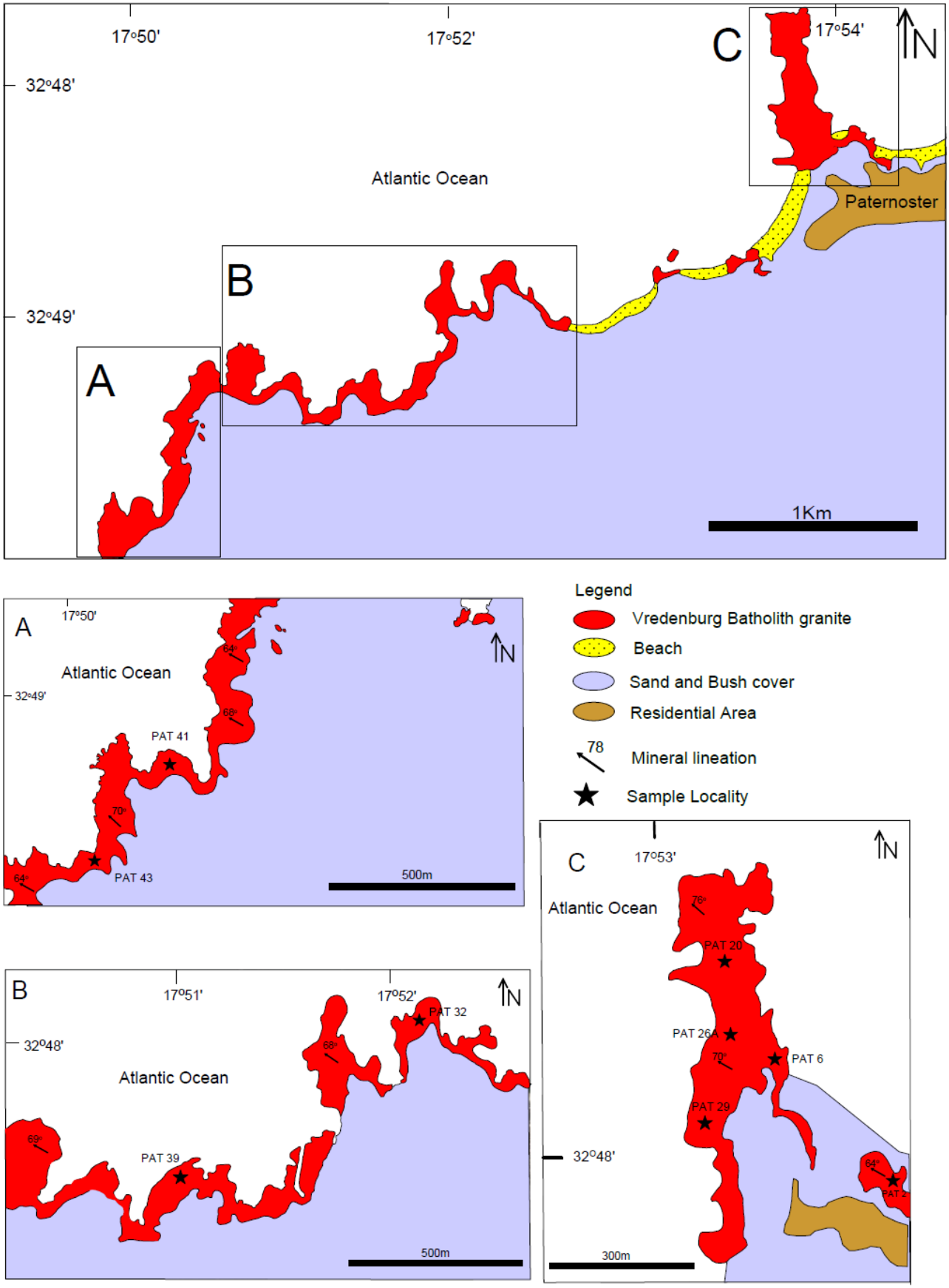

Figure 4.1: A simplified geological map of the Vredenburg Batholith granites along the coast of Paternoster. Insets A, B, and C are zoomed in sections of the rectangle blocks outlined on the main map.

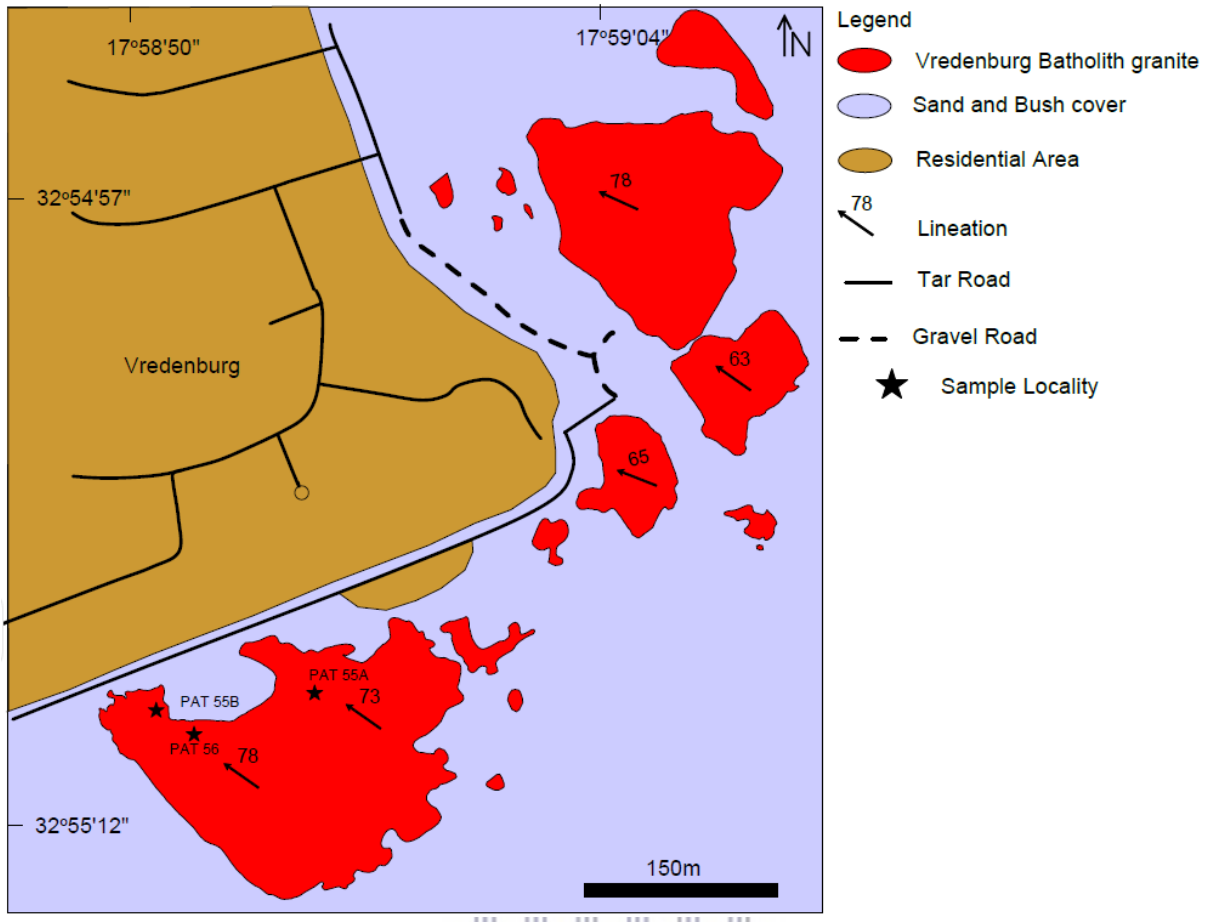

Figure 4.2: A simplified geological map of the Vredenburg Batholith granite outcrops in the town of Vredenburg.

4.2.1) Granites

The Vredenburg Batholith I−type granites to granodiorites, or simply termed granites for this study, in outcrop are coarse−grained, orange− to light−grey in colour with pinkish alkali feldspar megacrysts (1 – 4cm in length), giving it a porphyritic texture. The megacrysts are euhedral to subhedral in shape and define the NW−SE magmatic fabric of the pluton with some containing plagioclase mantled rims of ≈1 – 2mm thickness (Fig. 4.5 B). The Vredenburg Batholith contains spectacular magma mingling zones (Fig. 4.3 A – D& F) that produced large portions of granodioritic outcrops which are found only in "Section C" of the mapped area (Fig. 4.1). Smaller IEs (IE1 and IE2) and country rock inclusions (xenoliths) are present throughout the batholith (Fig. 4.8). Sharp contacts are generally observed between the granite and enclaves (Fig. 4.3 E and Fig. 4.5, excluding A), however, in sections where the magma mingling zones are located there are gradational contacts between the enclaves and granite (Fig. 4.3 D). Moreover, in a rare case, parts of the host granite are entrained in the granodiorite (Fig. 4.3 B), which exhibits a sharp contact.

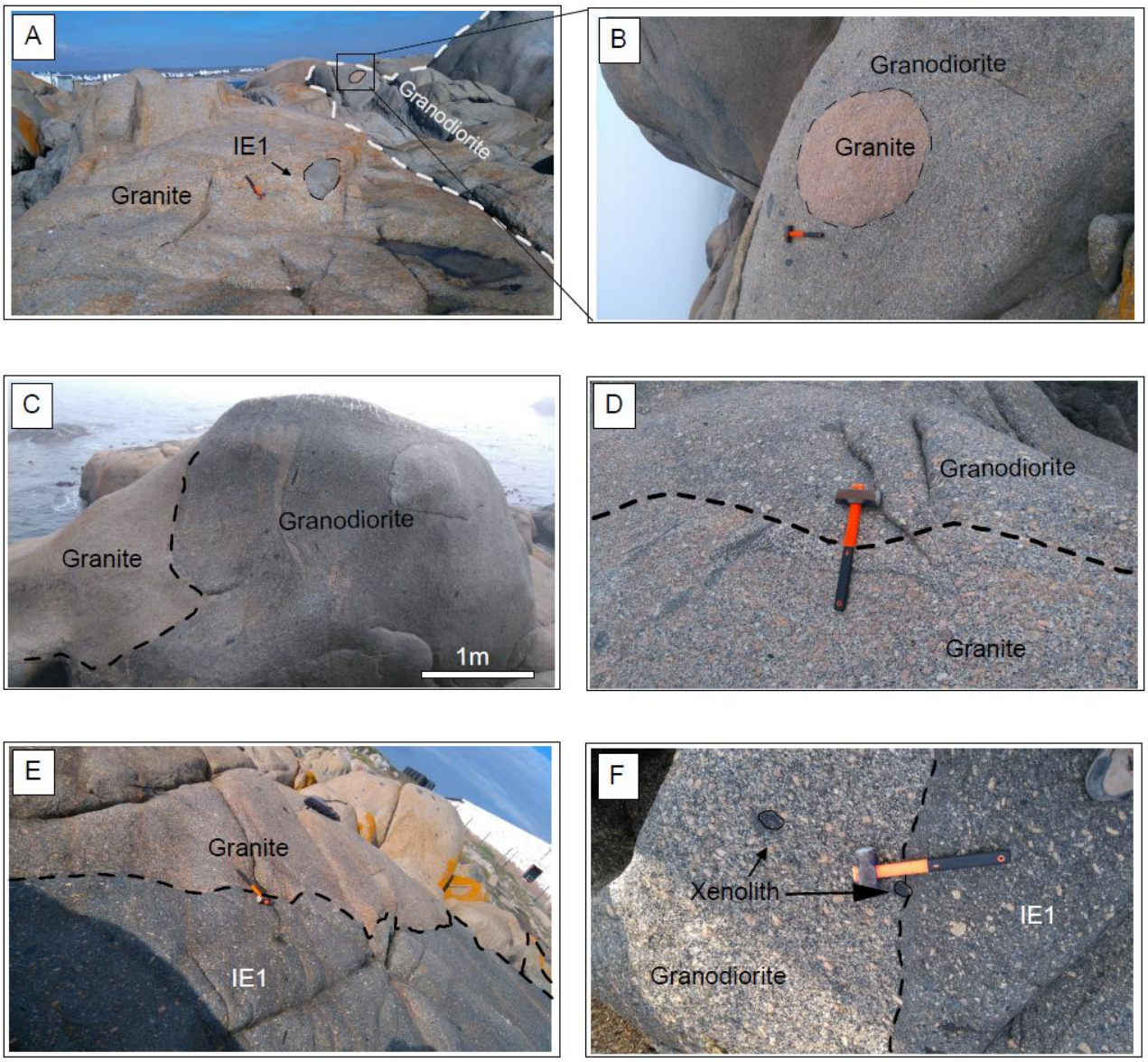

Figure 4.3: Field photographs of the granites, their magmatic structures, enclaves and, contacts of the Vredenburg Batholith. A, B, C and D) Illustrations of the various types of contacts between the host granite (or simply granite) and the granodiorite as well as IE including examples of magma mingling zones. B) Inset in A, zoomed in image of the host granite appearing as an enclave in the granodiorite. E) Contact between granite and enclave (IE1). F) Contact between granodiorite and enclave (IE1), H). The length of the hammer is 32cm.

In hand samples, the groundmass of the granite has a coarse−grained, equigranular texture and consists of quartz (25 – 30%) that are 1 to 2cm in length, plagioclase crystals (20 – 25%), alkali−feldspar (25 – 30%), biotite and hornblende grains which are smaller than the surrounding matrix (0.8 – 1.0cm in length) and constitute a combined 10 −12%. According to the CIPW norm values, the secondary and accessory minerals of the granite include corundum, rutile, apatite, ilmenite, and zircon, however, these secondary phases are not visible in thin section.

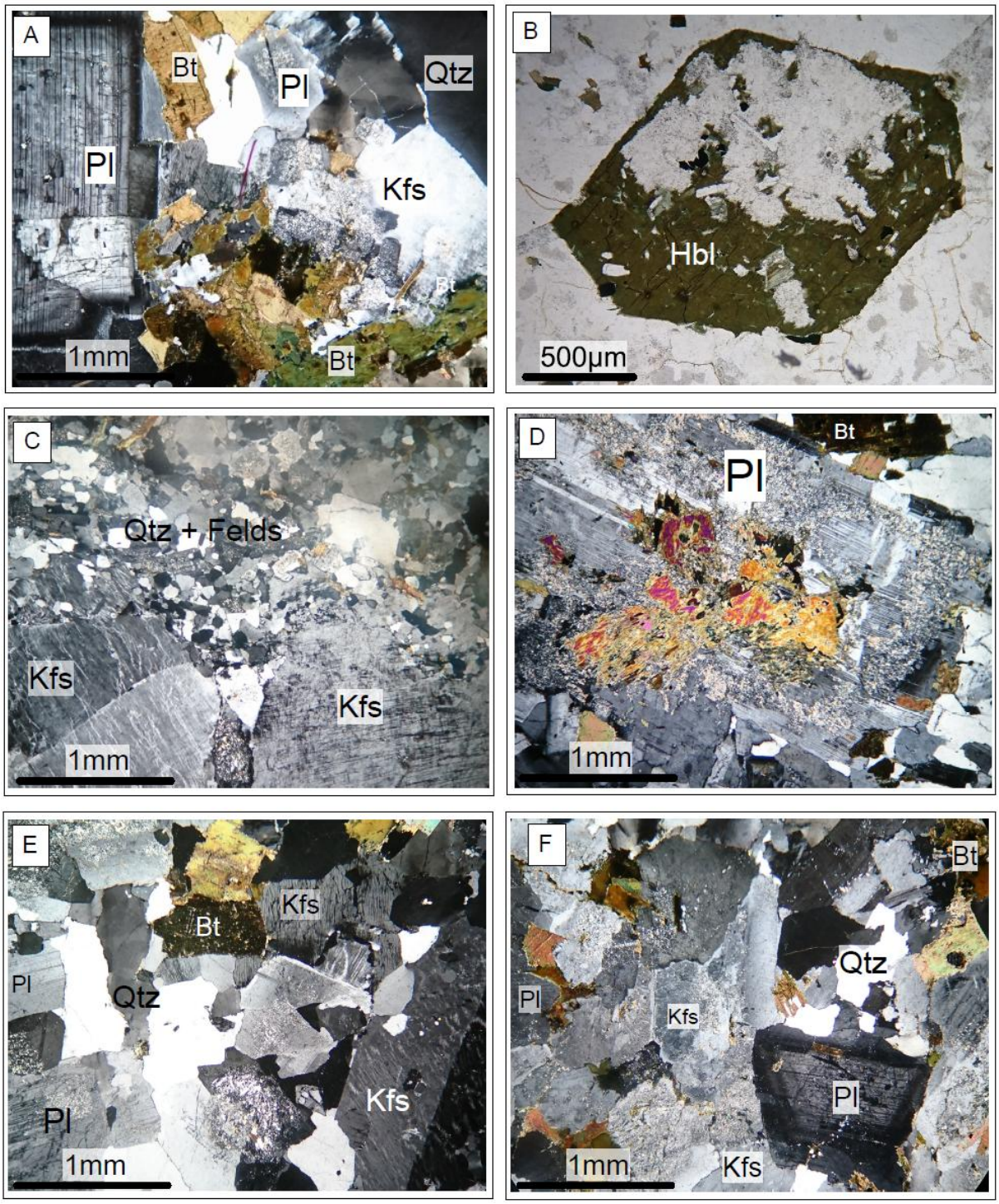

Figure 4.4: Photomicrographs of the Vredenburg Batholith granites. (A) Two biotite generations. The second generation (green) is overgrowing the first generation (brown) (bottom of the image). A plagioclase crystal exhibiting oscillatory zoning (left) is also present (crossed polarised light). (B) An euhedral hornblende with near perfect edges (plane polarised light). (C) Deformed euhedral alkali−feldspars with one twin crystal exhibiting perthitic texture (bottom left) and another undeformed (bottom right) crystal with microperthitic texture (crossed polars). (D) Plagioclase crystal, the core of which has been altered to sericite and epidote minerals with prehnite and pyrophyllite (crossed polars). (E & F) The typical equigranular texture of the groundmass observed from granite thin sections, E also shows an alkali−feldspar megacryst which exhibits perthitic exsolution textures and has quartz embayed at the edges (crossed polars). Mineral abbreviations: Bt = biotite, Felds = feldspars, Hbl = Hornblende, Kfs = alkali feldspar, Pl = plagioclase and Qtz = quartz.

In thin section, there is a bimodal grain size distribution, with megacrysts defined by perthite and a finer-grained matrix composed of quartz, plagioclase, perthite, biotite, and hornblende (Fig. 4.4). The alkali−feldspar megacrysts are euhedral to subhedral being 1 – 2 mm along the long axis and 1 mm in width. The megacrysts occur as two types, being those that are deformed and those that are undeformed (Fig. 4.4 C). The undeformed crystals have a microperthitic texture which is common for orthoclase, with deformed megacrysts showing Carlsbad twinning and albitic exsolution lamellae and, therefore, exhibiting perthitic texture. Certain megacrysts have embayed rims which have been filled by quartz (Fig. 4.4 E). Inclusions which are common in the alkali−feldspar megacrysts are quartz and plagioclase (Fig. 4.4 C) and, in rare cases, biotite.

The groundmass exhibits an equigranular texture (Fig. 4.4). Quartz crystals are typically smaller (0.5 – 1mm), subhedral to anhedral and fill the interstitial spaces of larger grains. Quartz occurs as the polycrystalline and monocrystalline variety and typically exhibits undulose extinction. Some quartz crystals have fractures that are filled with finer grained material, which are most likely filled with ilmenite.

Plagioclase forms euhedral to subhedral grains with lengths up to 2mm. Many of the crystals appear murky and cloudy due to sericitic replacement and, in rare cases, they have epidote alterations occurring with prehnite and pyrophyllite (Fig. 4.4 D & E). They are characterised by the alternating twins and some crystals exhibit oscillatory zoning. Overgrowths in the plagioclase are quartz (Fig. 4.4 A) and, in some rare cases, pyrophyllite (Fig. 4.4 D).

Biotite (0.1 – 1.5mm in size) is the most abundant ferromagnesian mineral occurring as two generational types. The first generation has brown pleochroism, occurs as subhedral to anhedral grains, have the typical tabular shape, but some of the boundaries have been resorbed by the second generation. Inclusions of quartz and zircon grains are observed in the brown biotite types. The second type has green pleochroism and forms euhedral to subhedral grains. These biotites overgrow the groundmass matrix and have consumed the edges of the first generation. The green biotites contain small (<1mm) zircon inclusions (Fig. 4.4 A). The first generation biotites are relatively more abundant than the second generation.

Hornblende constitutes the least abundant of the minerals in thin section. They are typically euhedral to subhedral, reach up to 1mm in length and, in one sample, has a prismatic habit (Fig. 4.4 B). The hornblende grains contain quartz inclusions.

4.2.2) Magmatic fabrics

The Vredenburg Batholith exhibits magmatic fabrics throughout the batholith defined by: 1) the NW magmatic lineation defined by the preferred orientation of the long axes of alkali−feldspar crystals and quartz aggregates (Fig. 4.5 A), 2) the undeformed subhedral to anhedral quartz and feldspar groundmass surrounding euhedral alkali−feldspar megacrysts (Fig. 4.5 B), moreover the alkali feldspar exhibits recrystallised rims, 3) layering of mafic minerals, such as the biotite schileren which extend for a few meters and as a whole have a thickness of ≈20cm (Fig. 4.5 C), and 4) the long axes of IEs that are aligned with the NW trending magmatic foliation (Fig. 4.5 D).

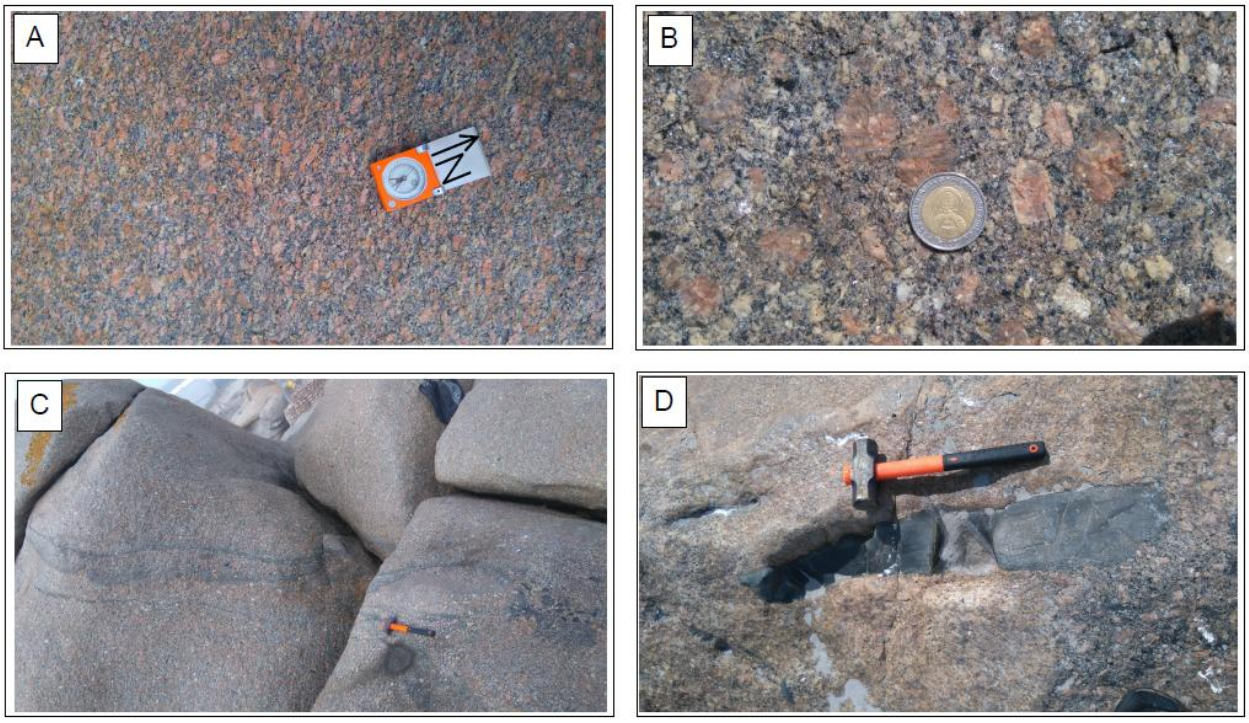

Figure 4.5: Magmatic fabrics of the Vredenburg batholith. A) Preferred mineral orientation defined by alkali feldspar megacrysts. B) Alkali feldspar megacryst exhibiting rapakivi texture with a plagioclase mantled rim. C) Mafic minerals defining biotite schlieren. D) Elongated intermediate igneous enclave (IE2) with its long axis in the same direction as the magmatic fabric. Scales: compass = 12cm, coin = 2.5cm, and hammer = 32cm.

4.2.3) Submagmatic and solid−state fabrics

Submagmatic deformation structures are well preserved and evident in the Vredenburg Batholith. Numerous cataclasite and mylonite zones are observed in the granites (Fig. 4.6 A, B). These structures are speculated to have formed by strike−slip movement of the Colenso Fault The cataclastic zones appear as extremely fine−grained, dark bands that typically are 8 to 10 cm in width and reach lengths

well over 100m and typically, trend N – S (Fig. 4.6 A& C). In thin section, cataclasite zones have rounded to elongated, fractured quartz grains suspended in a fine−grained matrix consisting of biotite and feldspars (Fig. 4.7 A−B). Subparallel to the magmatic foliation S−C structures within the mylonites are prevalent throughout almost the entire outcrop and indicate a dextral sense of shear (Fig. 4.6 C). The S−C structures suggest a continuous deformation from magmatic− to solid−state (Han et al., 2014). In thin section, the submagmatic fabrics are defined by the recrystallisation of pre-existing alkali feldspar crystals (Fig. 4.7 C) which is indicative of near−solidus high−temperature processes (Han et al., 2014).

Solid−state fabric features are prevalent in thin section as well (Fig. 4.7 D−F). They are characterised by kinking and bending in deformation twins of plagioclase crystals (Fig. 4.7 D−E), albitic exsolution lamellae of the alkali feldspar crystals (Fig. 4.7 F), and the common undulatory extinction observed in quartz. Lastly, the Vredenburg batholith contains many shallow fractures that appear as conjugate joint sets (Fig. 4.6 D). Two trends are observed, a north−south trending set and an east−west trending joint set. The spacing between the joint ranges from a few cm's to ≈1m in other areas. They are located throughout the outcrop and are most likely related to the exhumation of the granite batholith.

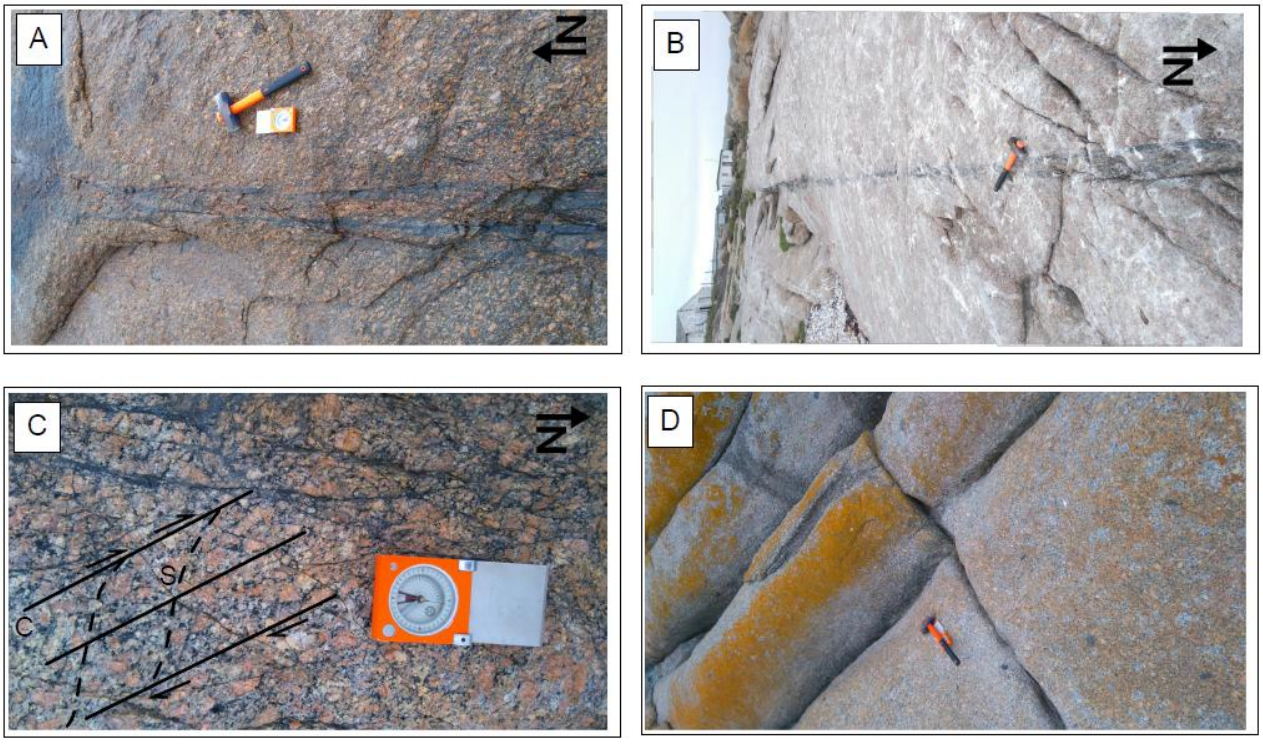

Figure 4.6: Submagmatic and solid−state fabrics of the Vredenburg batholith. (A & B) Cataclasite zones. (C) S−C structures of the granite indicate a dextral sense of shearing. (D) Shallow joints defining a conjugate joint set. Scales: Hammer = 32cm and compass = 12cm.

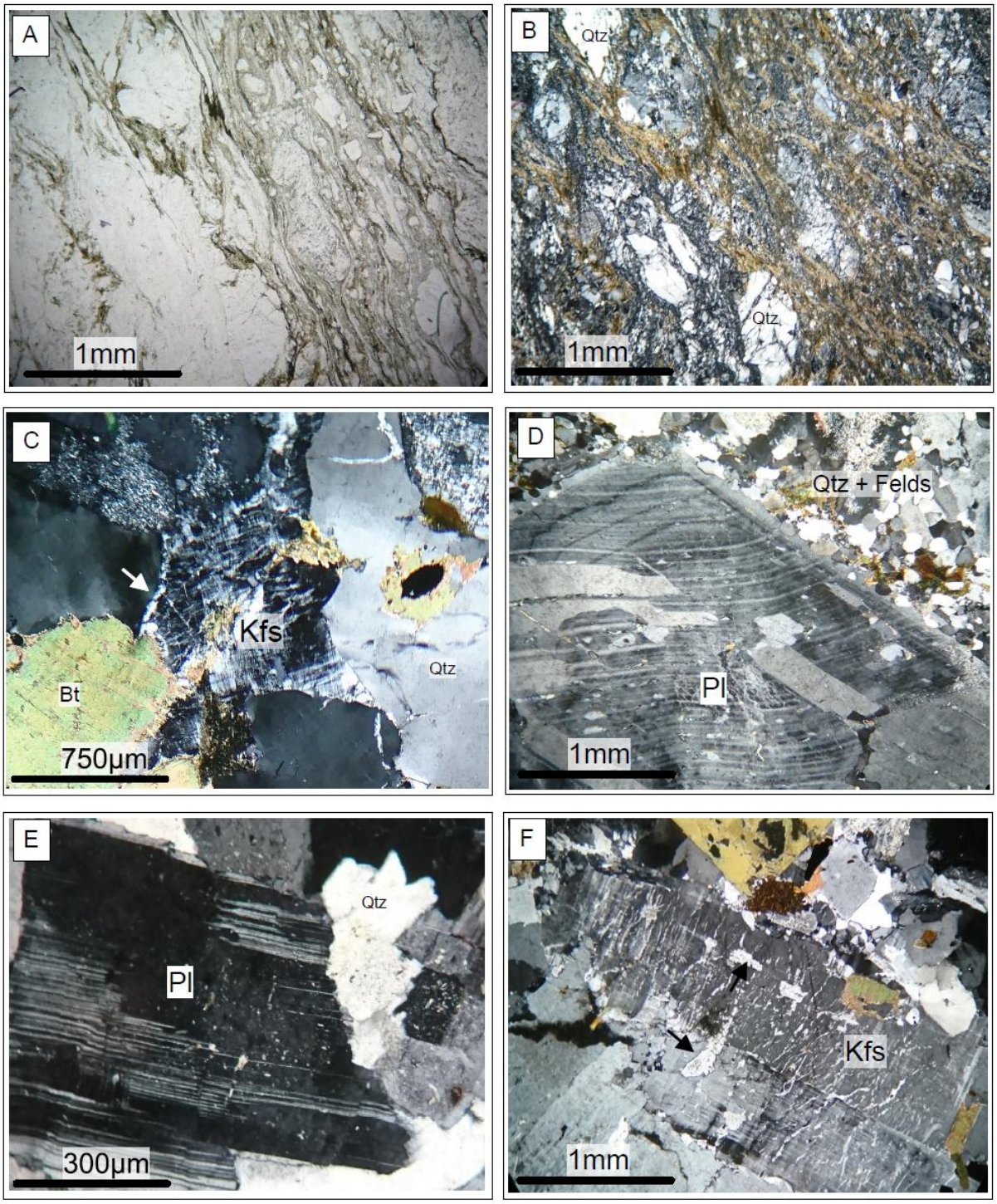

Figure 4.7: Photomicrographs of submagmatic and solid−state fabrics of the Vredenburg Batholith. (A & B) Mylonitic deformation in the Vredenburg granites. The quartz crystals are rounded and supported in a fined grained matrix of quartz, feldspars, and biotite defining a strong foliation A=plane polarised light and B=crossed polars. (C) Microfractures in Kfs grain filled with elongated quartz (white arrows) (crossed polarised). (D) Wave−like bending of deformation twins of the plagioclase which also exhibits oscillatory zoning and Kfs inclusions (crossed polarised). (E) Kinking in the twinning of the plagioclase as well as recrystallised margins (crossed polars). (F) Albite exsolution lamellae in the Kfs megacryst due to internal deformation. The megacrysts contain quartz (black arrows) and biotite inclusions (crossed polars). Mineral abbreviations: Bt = biotite, Felds = feldspars, Kfs = alkali feldspar, Pl = plagioclase and Qtz = quartz.

4.2.4) Igneous enclaves

Entrained in the granites are a variety of igneous enclaves, from intermediate to mafic, coarse− to fine−grained, porphyritic to equigranular, and with different mineral assemblages. The porphyritic enclaves (IE, labeled as IE1 in the figures) contain euhedral plagioclase and alkali feldspar phenocrysts orientated parallel to the magmatic fabric of the host granite. The alkali feldspar phenocrysts are smaller than those in the host granite (0.2 – 2cm in length), however, their abundance is much less (≈5%). The plagioclase phenocrysts are 0.5 – 1cm in size. The groundmass is medium−grained and comprises biotite (≈30%), hornblende (10%), plagioclase (10%) and quartz (5%). Their secondary and accessory mineral assemblages are similar to the host granites. The enclaves labeled IE2 are fine−grained, equigranular with a mafic mineral assemblage comprised mainly of biotite and hornblende. Their size ranges from 4cm (Fig. 4.8 G) to relatively large blobs well over 60cm (Fig. 4.8 B and E). The shapes of the IE2enclaves vary from amoeboid (Fig. 4.8 B), round (Fig. 4.8 D), ovate (Fig. 4.8 F) and oval (Fig. 4.8 G). Contacts between the granite and IE2 are sharp (Fig. 4.8 B – H) indicating that the enclaves crystallised beforehand and were carried along by the ascending magma (Villaros, 2010).

From the enclaves, only a single population was investigated petrographically. These are the intermediate, porphyritic igneous enclaves labeled IE1, which, from here on, will be referred to as igneous enclaves or IE. In thin section, they show a panidiomorphic texture characterised by equigranular grain sizes and subhedral to anhedral crystal shapes (Fig. 4.9 C−H). Biotite is the most abundant ferromagnesian mineral observed, with their crystal sizes ranging from 0.8 to 1mm forming stubby block shapes (Fig. 4.9 F). The most common biotite observed has light brown pleochroism in plane polarised light. The second type of biotite is light green in plane polarising light. The second type of biotite is much larger in size (≈1.5mm) than the light brown variety and is more common in the enclaves resembling the second-generation biotite observed in the host granites (Fig. 4.9 C & D). In Fig. 4.9 G & H biotite and hornblende is seen to have replaced an orthopyroxene grain. Inclusions observed in the biotites include zircon, which has a greater abundance compared to those in the biotite of the host granite, and opaque minerals (Fig. 4.9 H). Alkali feldspar crystals occur as rare megacrysts entrained from the granite (Fig. 4.9 D), and as medium−grained crystals (both orthoclase and microcline) which are more common in the assemblage of the IEs (Fig. 4.9 D & H). The megacrysts are subhedral and are partially replaced by sericite. The medium−grained alkali feldspar from the groundmass are anhedral and have fractures which are filled with quartz. Plagioclase crystals are anhedral, exhibit deformation twins and, in some cases, have been replaced by sericite and contain

quartz inclusions (Fig. 4.9 H). Quartz generally takes up the interstitial spaces in the matrix of the IE. They are medium grained (0.5 – 0.7mm) and exhibit undulose extinction.

Metasedimentary xenoliths are present throughout the outcrop as well, with their abundance, in particular, much greater in “section C” at the northwestern corner of Paternoster (Fig. 4.1) relative to the other sections of the mapped area. Their size varies from a few cm to 27cm across the long axis (Fig. 4.8 A). Xenoliths appear as either isolated fragments or within xenolith−enriched zones (Fig. 4.8 A). Based on previous studies the metasedimentary xenoliths are postulated to be from the Malmesbury Group (Belcher and Kisters, 2003). No evidence for contamination was observed of the host granites by the xenoliths. According to Belcher and Kisters (2003) and Villaros (2010), the xenoliths have been subjected to low-grade metamorphism; their mineral assemblage resembles that of the lower greenschist facies. In thin section, the xenoliths are fine−grained and show a relict planar lamination sedimentary structure (bedding) (Fig. 4.9 B). Grains are elongated and subhedral to anhedral. Biotite is most abundant (50%) and shows tabular shapes, however, the edges are angular (Fig. 4.9 B). Quartz grains are stubby and, in some cases, have smooth boundaries, however, they are mainly sharp and jagged with interlocking boundaries. Orthoclase crystals are present in minor amounts (<5%) and show lamellae that are albitic in composition.

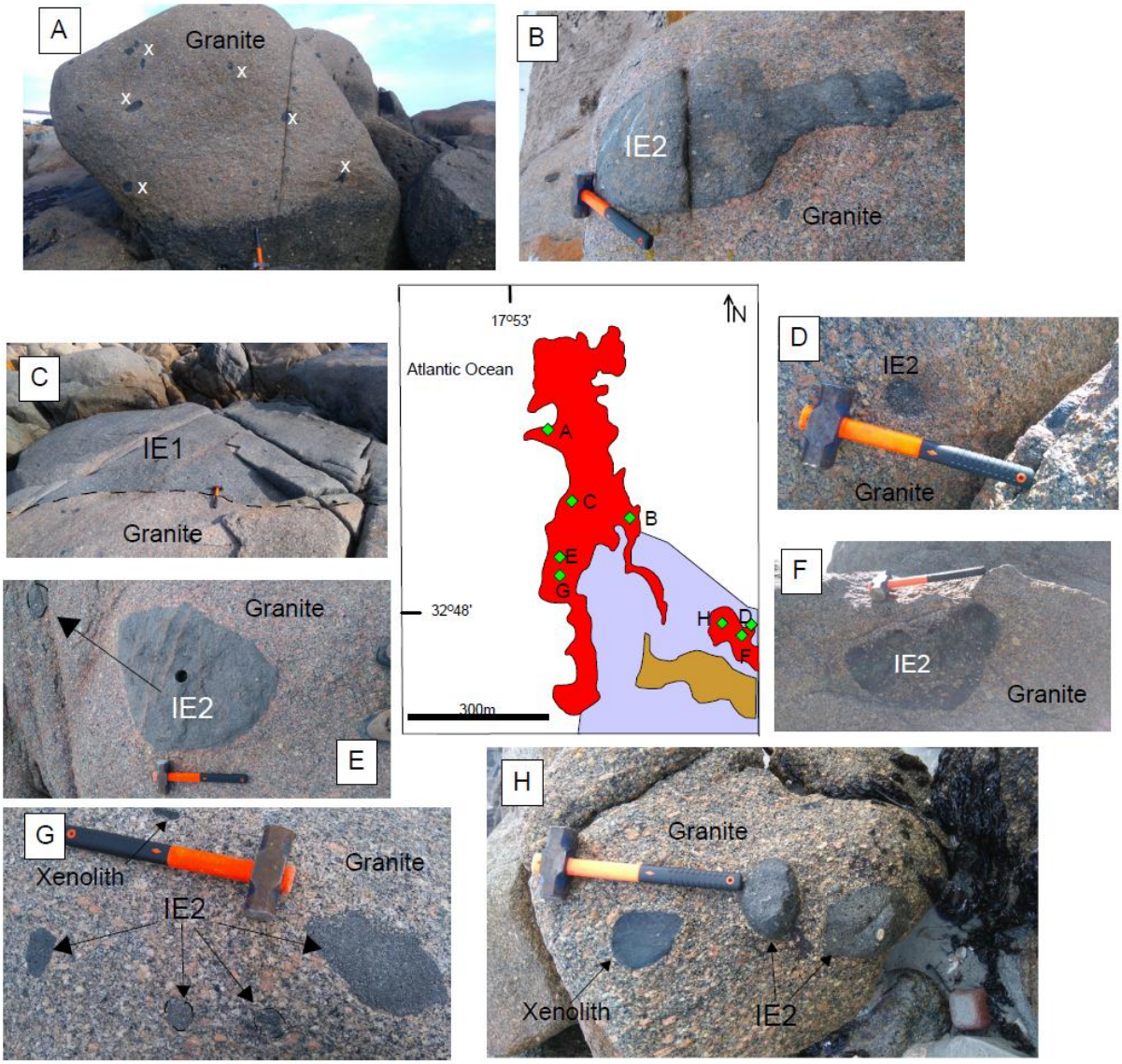

Figure 4.8: Field photographs of the magmatic microgranular enclaves and xenoliths. (A) Abundant xenolith zone in the granite, with xenoliths marked by an x. (B) Amoeboid shaped enclave (IE2). (C) Large enclave in the granite (IE1). (D) Rounded enclave (IE2). (E) Quartz veins crosscutting an enclave (IE2) the arrow points to a xenolith. F) Enclave exhibiting a greater abundance of alkali feldspar minerals (IE2), indicative of mingling. G)& H) Various shapes and sizes of xenoliths and enclaves (IE2). The length of the hammer is 32cm. The central map shows the location of each photo.

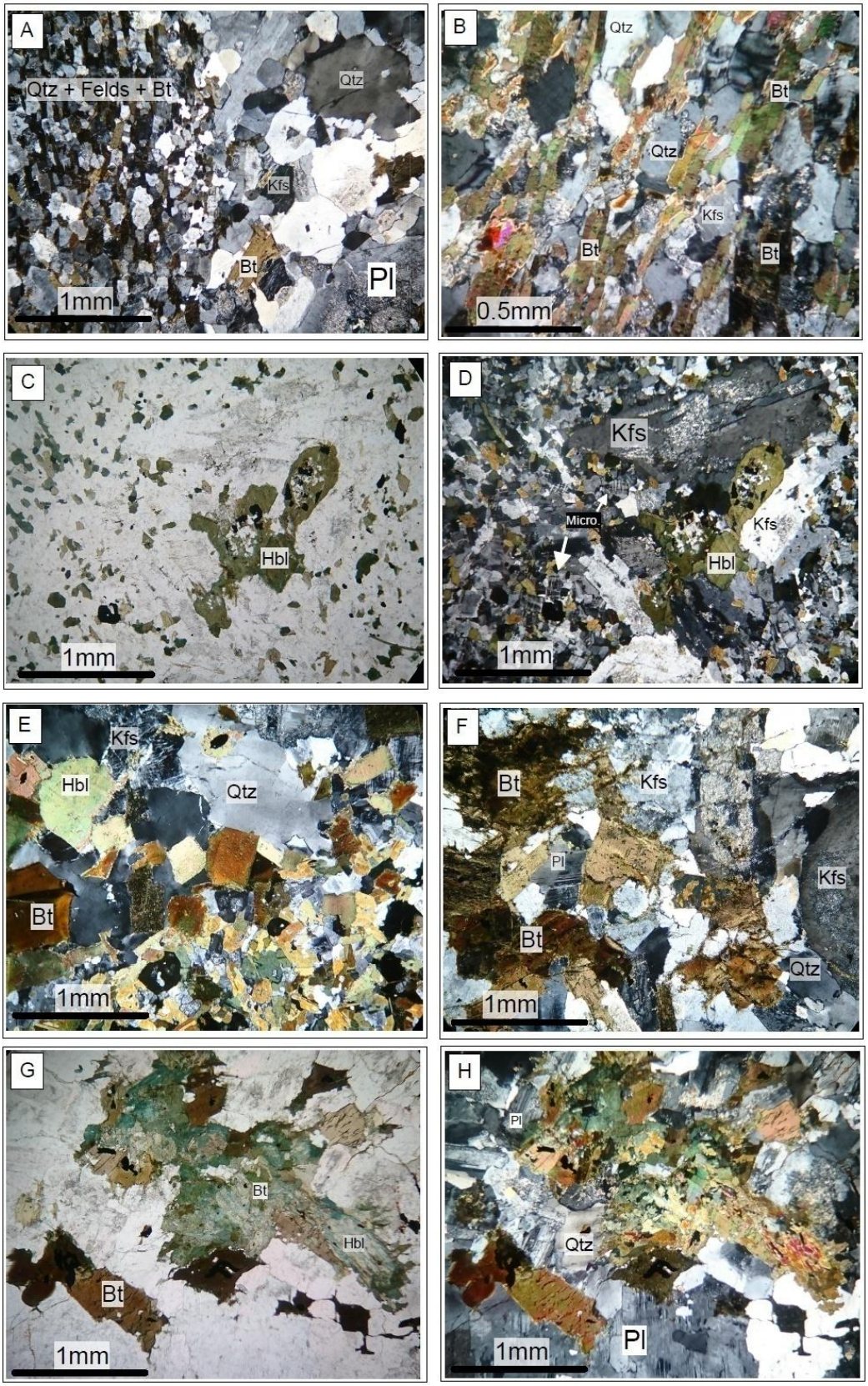

Figure 4.9: Photomicrographs of IE1 and xenoliths. (A) Contact between the xenolith (left) and host granite (right) (crossed polars). (B) Relict foliation defined by the alignment of the matrix of the xenoliths (crossed polars). (C& D) The entrainment of alkali feldspar and hornblende in an IE. The alkali feldspar exhibits sericitisation (C= plane polarised light, D= crossed polars). (E) Contact between the granite (top left) and IE (bottom right) (crossed polars). (F) Panidiomorphic textures which are common of the IE (crossed polars). (G & H) Biotite and hornblende aggregate replacing a pyroxene crystal (G= plane polarised light, H= crossed polars). Mineral abbreviations: Bt= biotite, Felds = feldspar, Hbl = hornblende, Kfs = alkali feldspar, Micro = microcline and Qtz = quartz.

4.2.5) Aplite veins and mafic dikes

The Vredenburg Batholith was intruded by aplite veins and mafic dikes. The aplite dikes generally have a strike trending E−W and typically dipping angles that are sub-vertical (> 80°); however, in rare cases, there are veins that strike N−S that dip subhorizontally at <10° (Fig. 4.10 A). They are fine−grained, composed of quartz (40%) and feldspars (60%) with an equigranular texture in hand specimen. All the vein−granite boundaries have sharp contacts, suggesting intrusion into a relatively rigid host granite. In thin section, the aplite veins exhibit a granophyric texture (Fig. 4.11 A). The boundaries of the alkali feldspar have been overgrown by myrmekite, albeit they still exhibit their euhedral shape. Quartz crystals are subhedral to anhedral and have fractures filled with finer material. Mafic dikes also intrude the granite within fractures, striking E−W and having dip angles that are sub-vertical to vertical (angles > 85°) (Fig. 4.10 B). Their textures and mineral composition are fine−grained and gabbroic in hand specimen. The mineral assemblage consists of chlorite (50%), plagioclase (30%) and orthopyroxene (20%) (Fig. 4.11 B−D). Plagioclase crystals are euhedral and much larger than the surrounding matrix. Moreover, they have been sericitised (Fig. 4.11 B). Chlorite crystals occur interstitially. Orthopyroxene crystals appear to be replaced by chlorite. They show second order interference colours in crossed polars (Fig. 4.11 D). The crystals are fractured and have jagged edges. The contacts observed between the host granite and mafic dikes are sharp.

Figure 4.10: Aplite vein and mafic dikes in the Vredenburg batholith. A) Crosscutting aplite veins. B) Mafic dike intruded into the Vredenburg batholith, dike width = 70cm. The length of the hammer is 32 cm.

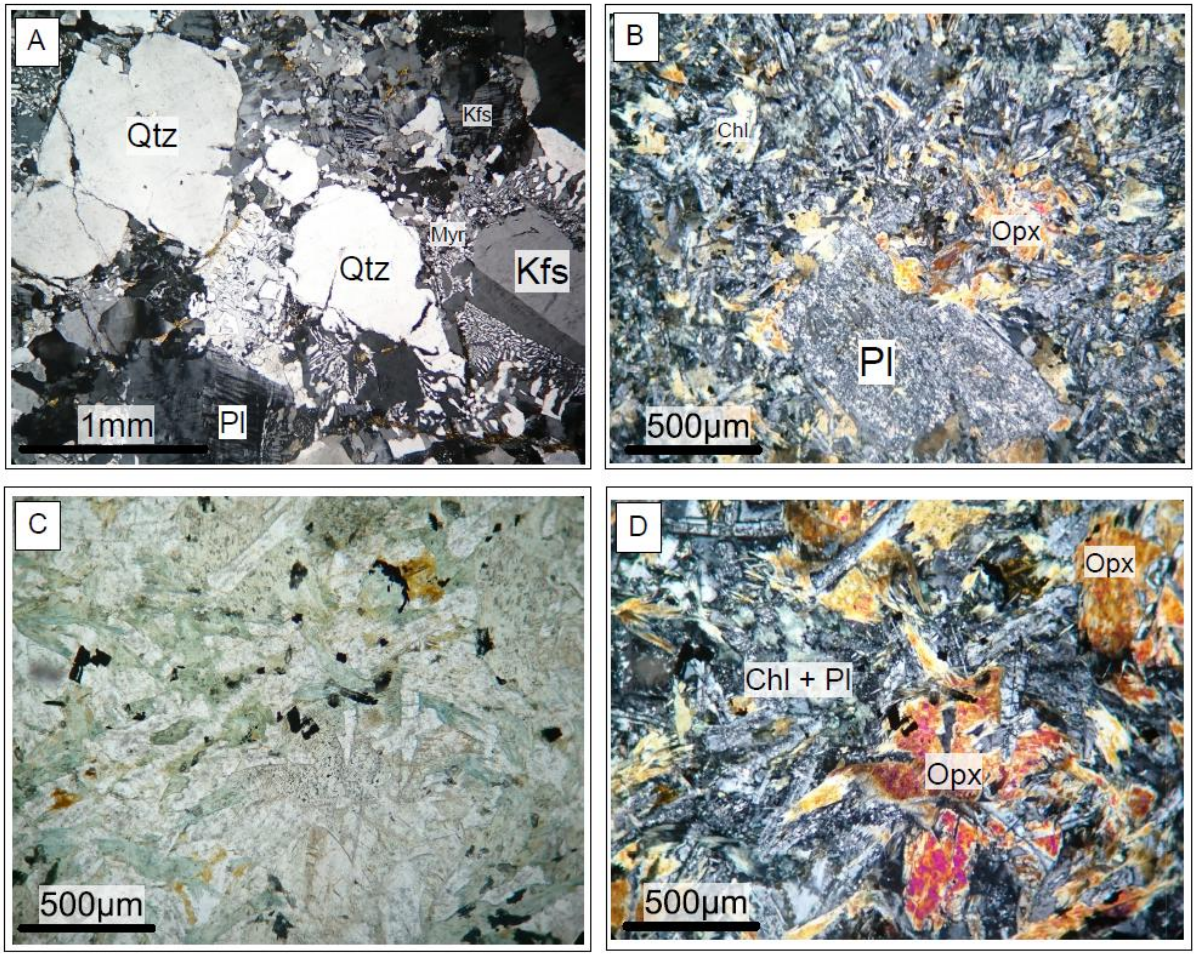

Figure 4.11: Photomicrographs of an aplite vein (A) and the mafic dike (B, C, and D) . (A) Granophyric texture exhibited by the aplite vein, as well as myrmekitic intergrowth along orthoclase phenocryst grain boundaries (crossed polars). (B) Plagioclase that has been sericitised. (C & D) Interstitial textures defined by the chlorite and plagioclase, D) An anhedral orthopyroxene which has been replaced by chlorite (C=plane polarised light and D= crossed polars). Mineral abbreviations: Chl = chlorite, Myr = myrmekite, Opx = orthopyroxene, Pl = plagioclase and Qtz = quartz.

4.3) Cape Columbine Granite

The outcrops occur along the west coast of the Cape Columbine Nature Reserve just north of the Colenso Fault (Fig. 4.12). They are of the Ab−type and have been classified as alkali feldspar granites (Scheepers, 1995).

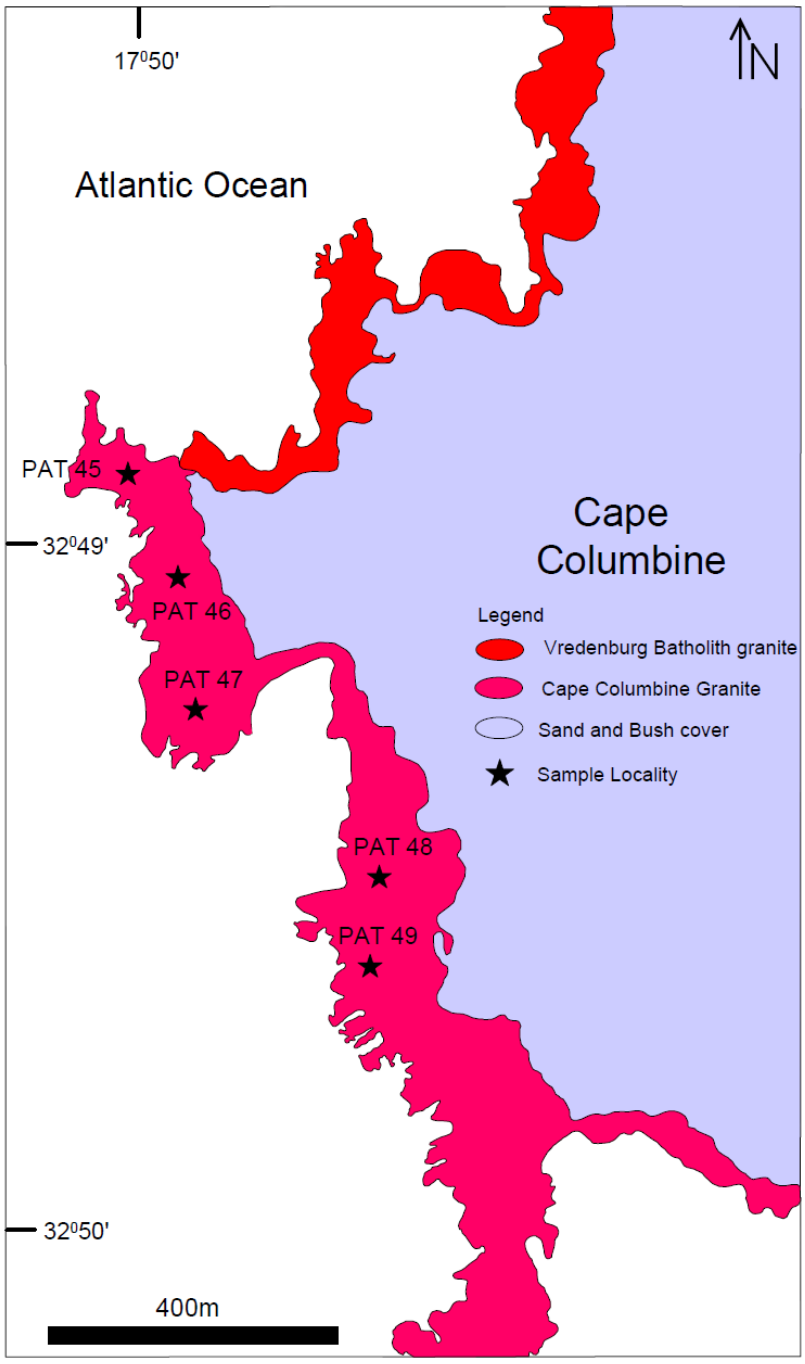

Figure 4.12 A simplified geological map of the Cape Columbine Granite and Vredenburg Batholith granite along the coast of Cape Columbine.

4.3.1) Cape Columbine granites

The granites in outcrop and hand specimen are massive, foliated, red to orange in colour, equigranular and coarse−grained. The mineral assemblage, with modal percentages in parentheses, consists of euhedral to subhedral alkali feldspar (50%), quartz (25%), plagioclase (20%), biotite (<5%), grain sizes vary between ≈ 8 – 10mm in length (Fig. 4.13 A) along with accessory amounts of corundum, ilmenite, and apatite. The outcrop contains rafts of the adjacent Vredenburg granites (Kisters et al., 2002) and no metasedimentary xenoliths.

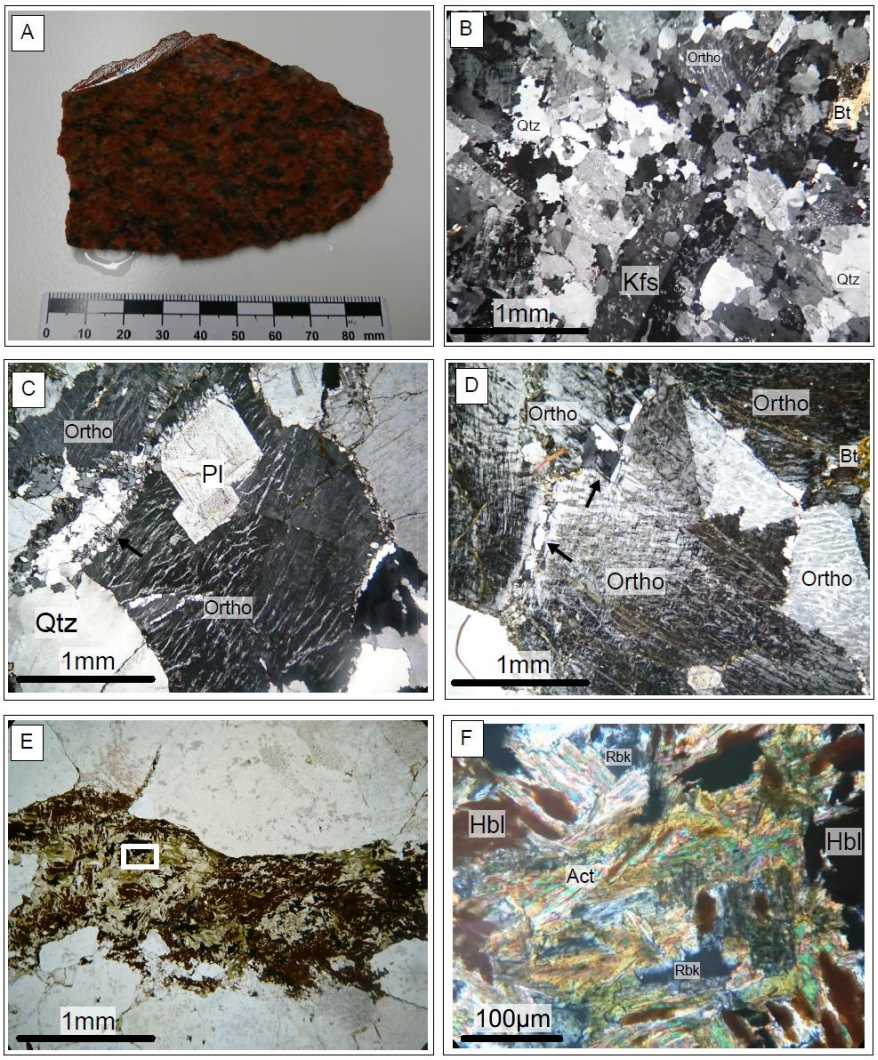

Figure 4.13: Representative images of the Cape Columbine Granite. (A) Hand specimen of the coarse−grained, equigranular, dark−red alkali feldspar granites. (B) In rare cases, a porphyritic texture is observed with the finer quartz filling the interstitial space between orthoclase (crossed polars) (C) Subhedral orthoclase crystal exhibiting perthitic texture with a plagioclase inclusion and a "ribbon−like" recrystallisation of quartz and plagioclase on the rim (black arrow) (crossed polars). (D) Orthoclase showing a cloudy appearance with biotite "hair−like" strand inclusions, as well as, interstitial quartz filling the spaces between the orthoclase crystals (black arrows) (crossed polars). (E & F) Amphibole aggregate replacing pyroxene crystals, F, is a zoomed in image of the white square in E (crossed polars). Mineral abbreviations: Act= actinolite, Bt = biotite, Hbl = hornblende, Ortho = orthoclase, Rbk = Riebeckite and Qtz = quartz.

In thin section, the most abundant mineral is orthoclase (>60%). Orthoclase grains are subhedral to euhedral, 0.5 – 2.5mm along the long axis, with albitic exsolution lamellae; in certain cases, the orthoclase crystals show Carlsbad twinning (Fig. 4.13 B – D). The edges of the crystals are jagged and in certain cases have been recrystallised (Fig. 4.13 C). Plagioclase forms anhedral to subhedral crystal shapes which are 0.8 to 1mm in length. The appearance exhibited is cloudy due to sericite replacing the grain. Where plagioclase grains are clear they exhibit simple polysynthetic twinning (Fig. 4.13 C). Quartz occurs as clots and in a variety of forms (Fig. 4.13 B). The most abundant form of quartz is fine−grained (<0.5mm), anhedral and interstitial, filling fractures (Fig. 4.13 C), with others being medium− to coarse− grained subhedral crystals. All quartz crystals exhibit undulose extinction. The main mineral assemblage of orthoclase, quartz, and plagioclase contain inclusions of biotite that are hair−like strands (Fig. 4.13 B, C, and D). Biotite is the least abundant (≈5%), forming anhedral grains that lack any shape. They appear light brown in plane polarised light and dark brown to green in crossed polars. In Figure 4.13 E & F, an amphibole aggregate consisting of actinolite, hornblende, and riebeckite can be seen replacing a pyroxene grain. All grains comprising the aggregate are anhedral, however, there are actinolite grains which show oval shapes which are subhedral (Fig. 4.13 F).

4.3.2) Deformation features

The Cape Columbine Granite exhibits a preferred northwest trending mineral orientation defined by the alignment of quartz aggregates. However, whether it defines a magmatic foliation is unknown (Kisters et al., 2002). Instead, the granites predominantly display solid−state fabrics defined by mylonite and cataclasite zones (Kisters et al., 2002).

In thin section, solid−state fabrics are present. They occur as: 1) fractures that are filled with finer grained material, such as pseudotachylite, 2) recrystallised quartz and plagioclase crystals around feldspar grains (Fig. 4.13 F), and 3) alkali feldspar crystals that exhibit albite exsolution lamellae (Fig. 4.13 B – D).

4.4) Classification

Due to the porphyritic texture of the granites and IEs, the petrographic analysis did not give a proper representation of the mineral assemblage abundances. Therefore, petrographic analyses were used in conjunction with the CIPW norm to determine the mineral assemblage abundances for classifying the rocks according to the quartz−alkali feldspar−plagioclase, albite was omitted due to it being an end member in both the plagioclase and alkali feldspar solid solution systems, plot of Streckeisen (1974) (Fig. 4.14). CIPW normative calculations, as well as a thin section modal count for each mineral for each rock type (granites and IE from the Vredenburg Batholith, and Cape Columbine Granite), are presented in Table 4.1. The granites and IEs have similar mineral assemblages according to the CIPW norm and plot as syeno−granites and monzogranites. The Cape Columbine Granite classifies mainly as alkali feldspar granites, with one sample plotting in the syeno−granite field.

Table 4.1: Mineral modal assemblage abundances determined by petrographic analysis and CIPW norm calculations for primary minerals.

	Quartz	Orthoclase	Albite	Anorthite	Biotite	Hornblende
Vredenburg Batholith Granites	25 – 30 %	25 − 30%	20 − 22%	8 – 10%	5 – 10 %	<5%
IE	31 – 35%	23 – 25%	23 – 25%	10%	10 – 15%	5 – 10%
Cape Columbine Granite	40%	30%	20 – 25%	<5%	<5%	n/a

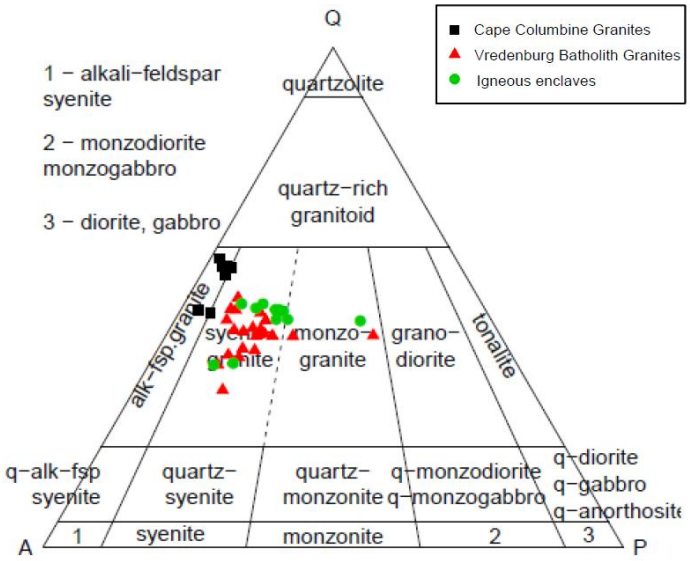

Figure 4.14: Diagram of Streckeisen (1976) which classifies magmatic rocks based on their primary modal mineral assemblage of quartz (Q), alkali feldspar (A) and plagioclase (P) content.

4.5 Summary of lithological description

Vredenburg Batholith

Granites

- The Vredenburg Batholith granites are pinkish to light grey in colour and have a prominent NW foliation defined by aligned alkali feldspar megacrysts..
- Hand specimen samples show a porphyritic texture, where the phenocryst is defined by large euhedral alkali feldspar megacrysts that occasionally contain a plagioclase rim. The groundmass is coarse−grained and composed of, in decreasing order of proportions quartz, plagioclase, alkali feldspar, biotite, and hornblende. The accessory minerals include corundum, rutile, apatite ilmenite and zircon.
- In thin section, the groundmass texture is generally equigranular, with the grain shapes ranging from euhedral to anhedral. The feldspar crystals show evidence of hydrolysis processes, thus most of the feldspar crystals have a cloudy texture due to having been replaced by sericite. Quartz exhibits undulose extinction. Biotite occurs as both a brown and green generations and, where hornblende is present, has euhedral shapes.
- Structural fabrics are observed ranging from magmatic to solid−state. In the Vredenburg Batholith can be summarised as: 1) cataclasite zones, 2) alignment of the mineral assemblage, 3) recrystallised rims of megacrysts, 4) S−C fabrics, 5) long axis of enclaves aligned with the magmatic foliation, 6) fractures in grains, 7) bending and kinking of polysynthetic twinning in plagioclase, and 8) perthitic textures observed in alkali feldspar.
- The outcrop has been intruded by aplitic veins and mafic dikes.
- Enclaves of igneous and country rock (xenolith, Malmesbury Shale) origins are present in the outcrop.
- On the IUGS classification, they plot mainly in the syeno−granite field mainly.

Enclaves within the Vredenburg Batholith

- Enclaves appear as a variety of intermediate to mafic magmatic bodies as well as, country rock entrained fragments (xenoliths).
- The IEs are grey to black in colour and show porphyritic texture. They are found throughout the batholith. Their sizes vary from a few cm across to well over a few meters. The phenocrysts that give the IEs their porphyritic texture are smaller alkali feldspar crystals than those found in

the host granite. The groundmass is composed of a similar composition as the host granite; however, the abundances of the mafic minerals (biotite and hornblende) are much greater.

- In thin section, the IE's studied (IE1) exhibit a panidiomorphic texture and the crystal textures are similar to that of the host granite.
- Contacts between the host granite and IE are generally sharp, however, in rare cases, there are also more gradational contacts.
- Xenoliths are found throughout the granite outcrop. They are composed of lower greenschist facies assemblages. In thin section, sedimentary textures have been preserved, such as planar lamination.
- Similarly to the host granite, the igneous enclaves also classify as syeno−granites.

Cape Columbine Granite

- The granites are equigranular, red in colour, and composed mainly of, in order of decreasing abundances orthoclase, quartz, plagioclase, and biotite.
- In thin section, the dominant mineral is orthoclase which shows perthitic texture and occurs as varieties that either shows Carlsbad twinning or not. Quartz exhibits undulose extinction and fills most of the interstitial spaces. Biotite is not common and generally occurs as strands in the alkali feldspar. In rare cases, an amphibole aggregate replacing a pyroxene was observed.
- Deformation structures present in the Cape Columbine Granites are as follows: 1) mylonitic and cataclastic zones, 2) recrystallisation of orthoclase grains, 3) orthoclase exhibiting exsolution textures, and 4) replacement textures which are abundant in thin section.
- They classify as alkali feldspar granites on the IUGS classification scheme.

Chapter 5 Geochemistry

5.1 Introduction

It should be noted that from this chapter and onwards the Cape Columbine Granite will be referred to as alkali feldspar granites based on their modal classification (Fig. 4.14). Chapter 5 consists of the whole−rock and Sr−Nd isotopic geochemical data from three rock types analysed from the research area. They are: 1) the Vredenburg Batholith (granites: 23 samples; its igneous enclaves: 13 samples), and 2) Cape Columbine Granite (alkali feldspar granites: 8 samples).

The structure of the chapter is as follows: the chapter consists of four sections, a section for major and trace elements (with the REE), isotopes and tectonic discrimination diagrams. The sections are then further separated into three subsections for each of the different rock types present in the field area. Note that before the heading of each section is a table containing the chemical concentrations of the section to follow, except for the last 2 sections, *5.5 Sr−Nd isotopes* and *5.6 Tectonic discriminant diagrams*.

Using maficity as an independent variable better indicates the mineralogical and chemical influences on the magma composition (Clemens et al., 2011). Plots for this chapter were generated using atomic values (cation) for major and trace elements and geochemical factors when plotted against maficity (Mg + Fe per 100g of rock sample). This removes the variations in wt. % concentrations that are caused by Mg# (100MgO/ MgO + FeO_t) and allow data trends to be interpreted for any addition of ferromagnesian material(s) and/or magma mixing processes which will be defined by a line between the host granite and enclave arrays, independently of Mg# (Clemens et al., 2017c). Therefore, modeling and geochemical plotting in the subsection 5.2 "*major elements*" for the granites and igneous enclaves of the Vredenburg Batholith will contain atomic element plots vs. maficity rather than the generally used silica (SiO_2) plots. However, for the alkali feldspar granites of the Cape Columbine Granite SiO_2 is used, as these granites show no variation in maficity values (Table 5.1).

Table 5.1: Whole−rock major elements concentrations for the Vredenburg Batholith (granites and igneous enclaves), and Cape Columbine Granites (alkali feldspar granite).

Rock Type	***Granites***																					
Sample	PAT2	PAT10	PAT11	PAT14	PAT17	PAT19	PAT21	PAT22	PAT26	PAT29	PAT31	PAT33	PAT36	PAT37	PAT39	PAT41	PAT43	PAT51	PAT52	PAT55A	PAT55B	PAT56
Major (%)																						
SiO_2	69,87	69,13	69,19	68,17	68,34	67,72	69,57	69,28	69,47	67,20	67,55	67,90	69,52	72,74	71,40	69,52	70,56	66,68	70,27	69,98	63,24	70,00
TiO_2	0,40	0,46	0,43	0,52	0,41	0,46	0,44	0,44	0,43	0,64	0,55	0,55	0,45	0,21	0,31	0,44	0,26	0,57	0,36	0,39	0,87	0,42
Al_2O_3	13,91	14,44	14,42	14,59	14,60	14,86	14,17	14,20	14,32	14,79	14,76	14,59	14,26	13,47	14,11	13,99	14,24	15,16	14,73	14,40	15,20	14,51
Fe_2O_3	3,28	3,67	3,51	3,92	3,39	3,76	3,46	3,62	3,45	4,42	4,27	4,12	3,71	2,32	2,87	3,83	2,60	4,15	2,80	3,01	6,37	3,20
MnO	0,05	0,05	0,06	0,06	0,05	0,06	0,05	0,06	0,06	0,07	0,06	0,06	0,05	0,06	0,05	0,08	0,05	0,08	0,05	0,06	0,18	0,05
MgO	0,63	0,69	0,68	0,91	0,59	0,68	0,74	0,77	0,69	1,18	0,88	0,87	0,67	0,31	0,44	0,60	0,41	0,83	0,51	0,55	0,92	0,58
CaO	2,23	2,25	2,20	2,38	2,03	2,07	1,90	2,05	2,23	3,06	2,37	2,59	1,33	1,26	1,38	1,93	1,59	2,29	1,80	1,72	2,79	1,93
Na_2O	3,09	3,06	3,16	2,96	3,18	3,20	2,88	2,98	3,09	3,05	3,01	3,02	2,88	2,92	3,02	3,26	3,19	3,03	3,14	3,00	3,00	3,04
K_2O	4,34	4,64	4,65	4,46	5,01	5,13	4,98	4,67	4,53	3,86	4,82	4,31	5,07	5,14	4,88	4,20	5,08	5,95	5,97	6,09	6,70	5,63
P_2O_5	0,11	0,11	0,11	0,12	0,10	0,12	0,11	0,12	0,11	0,18	0,13	0,14	0,11	0,05	0,07	0,10	0,07	0,20	0,12	0,13	0,20	0,14
L.O.I.	1,08	1,00	1,17	1,38	1,03	1,10	1,15	1,00	1,07	0,96	0,84	1,06	1,15	0,96	1,08	0,89	1,08	1,15	0,71	0,69	0,65	0,74
Sum Of Conc.	99,01	99,51	99,60	99,48	98,75	99,17	99,47	99,20	99,46	99,42	99,26	99,23	99,22	99,46	99,62	98,85	99,15	100,11	100,48	100,04	100,13	100,26
Mg + Fe	0,02	0,03	0,03	0,03	0,02	0,03	0,03	0,03	0,03	0,04	0,03	0,03	0,03	0,01	0,02	0,03	0,02	0,03	0,02	0,02	0,04	0,02
A/CNK	1,01	1,02	1,01	1,04	1,02	1,02	1,04	1,04	1,02	1,00	1,02	1,02	1,13	1,06	1,11	1,04	1,04	0,97	0,99	0,98	0,88	0,99
Fe*	0,84	0,84	0,84	0,81	0,85	0,85	0,82	0,82	0,83	0,79	0,83	0,83	0,85	0,88	0,87	0,86	0,86	0,83	0,85	0,85	0,87	0,85
ASI	1,01	1,03	1,02	1,05	1,02	1,02	1,05	1,04	1,02	1,01	1,03	1,02	1,13	1,07	1,11	1,05	1,05	0,98	0,99	0,99	0,89	1,00
MALI	5,20	5,45	5,61	5,04	6,16	6,26	5,96	5,60	5,39	3,85	5,46	4,74	6,62	6,80	6,52	5,53	6,68	6,69	7,31	7,37	6,74	0,07
Mg#	45,82	45,29	46,04	50,55	43,39	44,33	48,50	48,36	46,83	54,03	47,57	48,18	44,30	37,04	40,30	40,82	40,98	46,83	44,51	44,59	38,87	44,39

Table 5.1. *(Cont.)*

Rock Type	***Igneous enclaves***													***Alkali feldspar granite***							
Sample	PAT4	PAT6	PAT7	PAT13	PAT15	PAT24	PAT25	PAT26A	PAT28	PAT30	PAT35	PAT50	PAT54	PAT18	PAT34	PAT38	PAT45	PAT46	PAT47	PAT48	PAT49
Major (%)																					
SiO_2	71,06	69,52	62,31	71,32	71,18	68,63	68,60	64,26	68,81	68,21	73,62	69,86	67,80	75,13	75,94	76,77	76,67	78,62	77,50	77,79	76,38
TiO_2	0,42	0,55	1,02	0,43	0,44	0,60	0,62	1,08	0,59	0,67	0,29	0,63	0,68	0,09	0,09	0,04	0,04	0,06	0,06	0,06	0,04
Al_2O_3	13,52	13,84	14,94	13,45	13,49	14,11	13,95	14,56	14,06	13,97	12,78	13,69	14,21	12,49	12,09	12,30	12,34	11,87	11,44	11,63	11,77
Fe_2O_3	3,20	4,10	8,25	3,10	3,28	4,26	4,57	6,96	4,34	4,78	2,60	4,49	4,33	1,24	1,44	1,19	1,20	1,35	1,51	1,39	1,35
MnO	0,04	0,06	0,13	0,05	0,05	0,06	0,07	0,11	0,06	0,07	0,04	0,06	0,07	0,02	0,01	0,03	0,04	0,01	0,03	0,01	0,02
MgO	0,71	1,18	2,05	0,76	0,77	1,11	1,27	1,98	1,14	1,24	0,51	0,77	0,97	0,17	0,09	0,10	0,06	0,08	0,07	0,07	0,08
CaO	1,88	2,43	4,39	1,50	2,01	2,53	2,55	4,15	2,35	2,75	1,34	2,50	2,36	0,86	0,53	0,63	0,61	0,23	0,42	0,48	0,50
Na_2O	2,74	2,76	3,30	2,56	2,81	2,66	2,69	3,02	2,69	2,85	2,54	2,95	2,90	2,39	2,14	3,42	3,33	3,09	3,09	3,11	3,40
K_2O	4,57	4,06	2,06	4,85	4,35	4,19	3,89	2,28	4,05	3,86	5,06	4,00	5,48	6,15	6,57	4,54	4,81	4,92	4,89	4,87	4,60
P_2O_5	0,09	0,12	0,22	0,09	0,10	0,13	0,14	0,23	0,13	0,15	0,06	0,18	0,21	0,02	0,02	0,01	0,01	0,01	0,01	0,01	0,01
L.O.I.	0,90	1,10	0,97	1,35	0,87	0,89	0,91	1,06	1,03	0,64	0,71	0,85	0,95	0,68	0,50	0,55	0,59	0,57	0,65	0,64	0,58
Sum Of Conc.	99,14	99,73	99,65	99,47	99,36	99,18	99,27	99,70	99,26	99,20	99,57	100,00	99,97	99,26	99,44	99,60	99,71	100,83	99,69	100,08	98,75
Mg + Fe	0,02	0,04	0,07	0,02	0,03	0,04	0,04	0,06	0,04	0,04	0,02	0,03	0,03	0,01	0,01	0,01	0,01	0,01	0,01	0,01	0,01
A/CNK	1,05	1,04	0,96	1,10	1,04	1,04	1,05	0,97	1,07	1,01	1,06	1,00	0,95	1,03	1,04	1,05	1,05	1,10	1,03	1,03	1,03
Fe*	0,82	0,78	0,80	0,80	0,81	0,79	0,78	0,78	0,79	0,79	0,84	0,85	0,82	0,88	0,94	0,92	0,95	0,94	0,96	0,95	0,94
ASI	1,05	1,04	0,96	1,11	1,04	1,05	1,06	0,98	1,08	1,01	1,06	1,01	0,96	1,03	1,04	1,05	1,05	1,10	1,03	1,03	1,03
MALI	5,43	4,39	0,97	5,91	5,15	4,32	4,03	1,15	4,39	3,96	6,26	4,45	6,02	7,68	8,18	7,33	7,53	7,78	7,56	7,50	7,50
Mg#	49,42	55,89	52,25	51,91	50,83	53,43	55,03	55,61	53,63	53,32	46,34	43,02	49,66	37,64	21,58	27,01	18,04	20,69	16,95	18,15	20,69

5.2 Major elements

5.2.1) Granites

The major element compositions of 23 granite analyses are presented in Table 5.1. The granites classify mainly as granites on the total alkalis vs. SiO_2 plot, with a few samples classifying as quartz monzonite and granodiorite (Fig. 5.1). According to the Frost et al. (2001) classification scheme these are mostly ferroan, with a few samples plotting in the magnesian field (Fig 5.1 A); moreover, the samples that plot in the magnesian field are close to the Fe*−index boundary[Fe*−index (FeO^{tot}/FeO^{tot} + MgO) by weight) = 0.79 − 0.88]. For the modified alkali−lime index (MALI; Fig 5.1 B), defined by weight percentage concentration ($Na_2O + K_2O – CaO$), the granites exhibit mainly calc−alkalic to alkali−calcic values (MALI =0.07–7.31), and are weakly peraluminous to metaluminous with an aluminium saturation index (ASI) [Al/Ca x 1.67P + Na + K (molar)] of 0.89–1.13 (Fig. 5.2 C). They are silica−enriched, with their SiO_2 content ranging from 63.24 − 72.74 wt. %. The alkali element, K_2O, varies from 3.86 − 6.70 wt. % (Fig 5.1 D). Especially at low maficity values, the granites exhibit K_2O contents greater than the typical I-type granite (3.5 – 5.5 wt. %; Clemens et al., 2011). For other major oxides that are shown in appendix E, Na_2O values range from 2.88 – 3.26 wt. %. The CaO values are all >1 wt. % with a range of 1.26 – 3.02 wt. %. Other major element variability are: Al_2O_3: 13.47 − 15.20 wt. %, TiO_2: 0.21 – 0.87 wt. %, FeOt: 2.32 – 6.37 wt. %, MgO: 0.31 – 1.18 wt. % (maficity values ranging from 0.01 – 0.04), and P_2O_5: 0.05 – 0.20 wt. %.

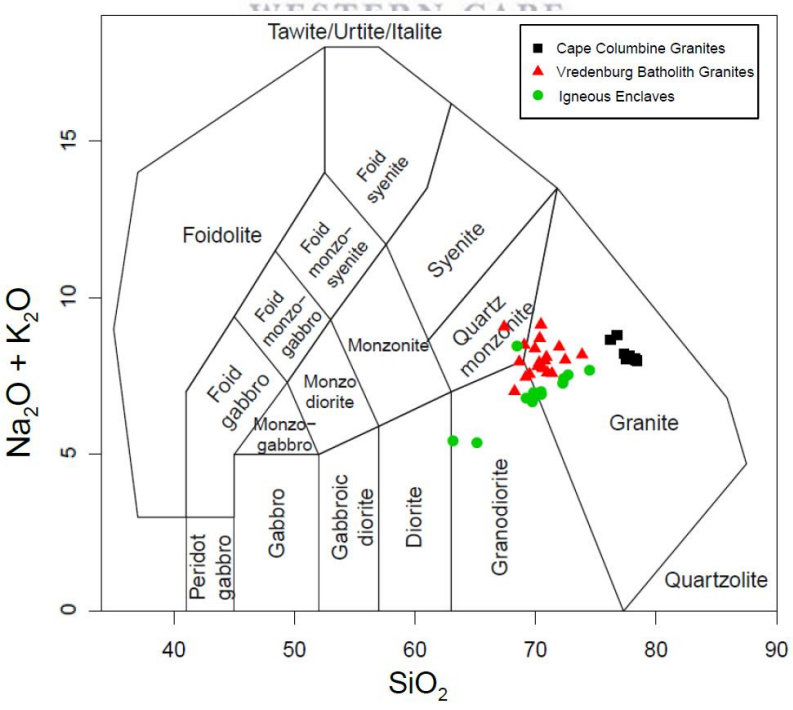

Figure 5.1: Total alkalis versus silica classification plot (after Middlemost, 1994).

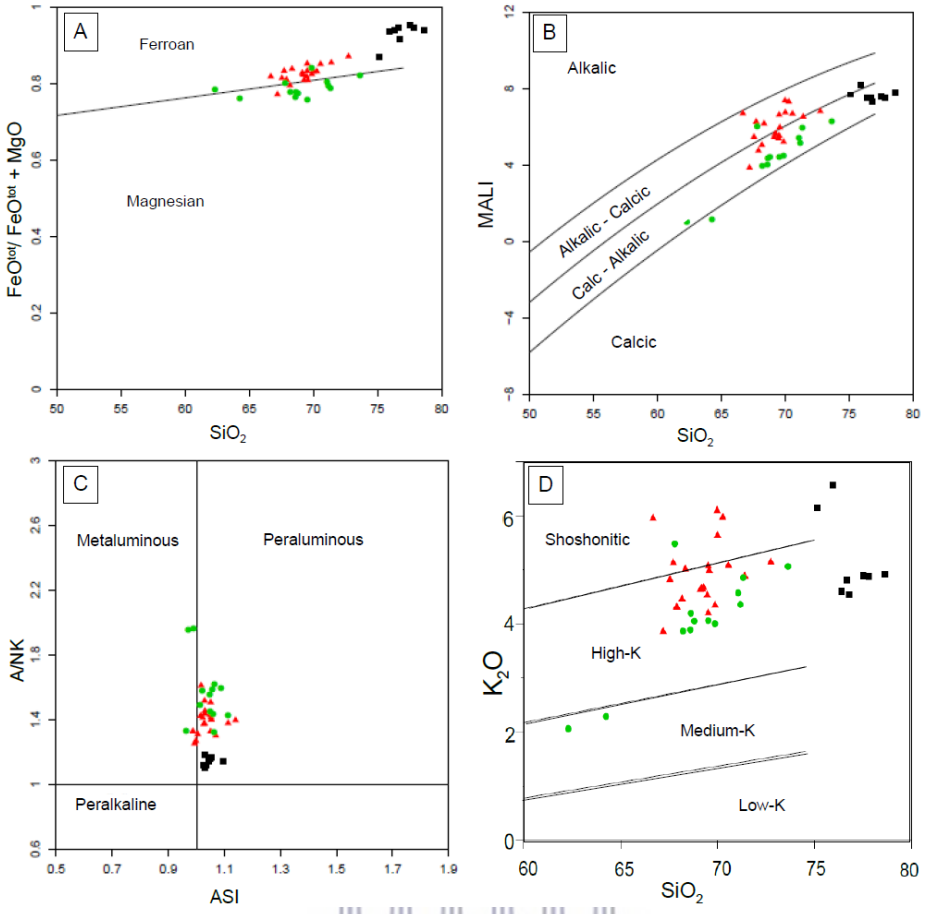

Figure 5.2: Lithochemical classification plots for granitic rocks (after Frost et al., 2001; the K_2O discriminant diagram after Rollinson, 1993). A) Fe*–index [FeO^{tot}/FeO^{tot} + MgO (mol.)] versus SiO_2. B) Modified alkali–lime index (MALI) [$Na_2O + K_2O – CaO$ (mol.)] versus SiO_2. C) Plot of Aluminium saturation index [Al/Ca x 1.67P + Na + K (mol.)] D) Harker plot for K_2O vs. SiO_2. Symbols are the same as in Fig. 5.1.

In the element variation diagrams plotted in Fig. 5.3, there are positive relationships between maficity (Mg + Fe atomic) and Ca, Al, P and Ti, and negative correlations arise between maficity and Na, K and, Si. However, elements such as Na, K, and Al show a scatter in their trends exhibiting a large degree of variation, whereas elements such as Ca, Ti and Si have well-defined negative linear trends with increasing maficity. In particular, a stand out correlation is the tight linear relationship produce by Ti vs. maficity, which has been reproduced in granitic geochemical analyses worldwide and is now considered a key indicator in granitoid chemical evolution which can be explained by the peritectic assemblage entrainment model (Clemens and Stevens, 2012). Lastly, notable trends in the granite compositional variations the steep array defined by Mg# and the decrease in ASI values with an increase in maficity.

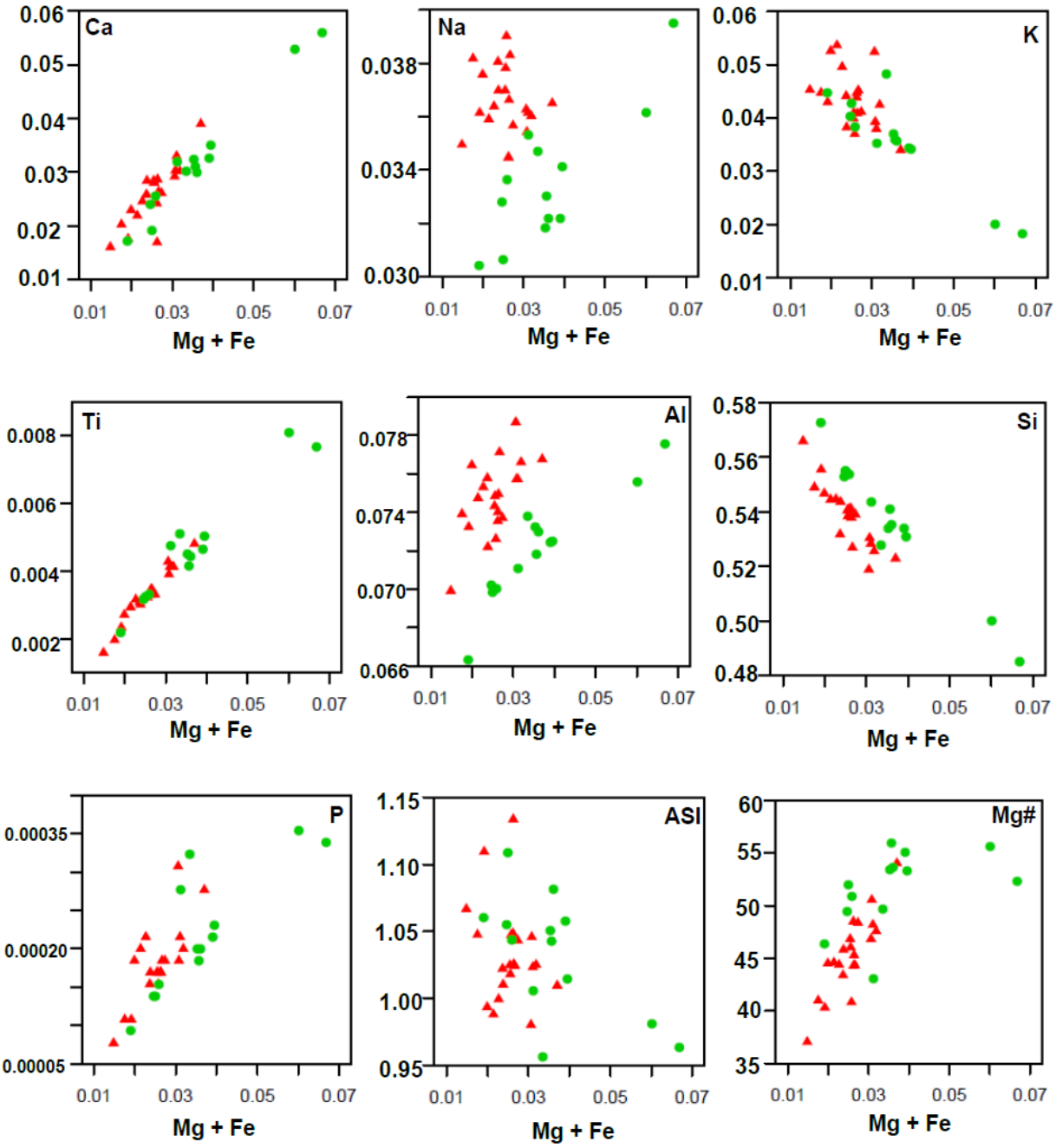

Figure 5.3: Various element atomic values and geochemical factors vs. maficity for the Vredenburg Batholith granites and enclaves. Red triangles represent granites and the green circles represent the IEs.

5.2.2) Igneous enclaves

The IEs mostly classify as granodiorites, with few samples plotting in the granite field and 1 sample plotting in the quartz monzonite field on the total alkalis plot (Fig.5.1). The IEs are mainly magnesian (Fe* = 0.78 – 0.96), with 3 samples plotting in the ferroan field; MALI values are mostly calc−alkalic (MALI = 0.97 – 8.18) with 2 outlier samples, one of which plots in the alkali−calcic field and the other in the calcic field. Both of these samples, however, plot close to the boundaries between their respective fields and the calc−alkalic field. The majority of the samples plot as weakly peraluminous, with 3 samples plotting in the metaluminous field (ASI = 0.96 – 1.11). Their major element data is presented in Table 5.1. The enclaves are enriched in silica relative to mafic rocks and reflect similar values as the host granite (SiO_2= 62.31 to 73.61 wt. %). Their K_2O values are high and range from 3.86 −5.48 wt. %, with 2 samples having lower values of 2.06 and 2.28 wt. % (PAT 7 and PAT26A, respectively). Other variability in the major elements includes: CaO: 1.34 – 4.39 wt. %, NaO_2: 2.54 – 3.30 wt. %, Fe_2O_3: 2.60 – 8.25wt. %, MgO: 0.51 − 2.05 wt. %, Al_2O_3: 12.78 – 14.94 wt. %, P_2O_5: 0.06 − 0.23 wt. %). When plotted against maficity (Mg + Fe) the enclave samples show a positive relationship with Na, P, and Al; there are also tight linear relationships with Ca and Ti (Fig. 5.3). Contrastingly, K and Si have negative linear correlations with increasing maficity (Fig. 5.3).

Based on the chemical compositions (Table 5.1) and trends observed (Fig. 5.3) there are a lot of similarities in chemical compositions and trends between the IEs and host granite for major elements vs. maficity, and there is a considerable degree of overlap. However, the maficity values are much higher in the IEs than in the host granite, which is most likely due to the greater biotite content in the enclaves (e.g. Clemens et al., 2017b). Also, note that for almost any given maficity value, the Mg# is much higher for the IEs (43.02 – 55.89) than its host granite (37.04 – 54.03) (Fig. 5.3). Lastly, the trend in ASI vs. maficity for the IEs and host granite trend toward a metaluminous nature with increasing maficity.

5.2.3) Alkali feldspar granites

Major element compositions for the alkali feldspar granites are presented in Table 5.1. On the total alkalis vs. SiO_2 plot (Fig. 5.1) the alkali feldspar granites classify as granites. The alkali feldspar granites plot in the ferroan field, are calc−alkalic, and weakly peraluminous (Fe*−index= 0.88 – 0.96; MALI= 7.33 – 8.18; ASI= 1.03 – 1.10) (Fig. 5.2). The alkali feldspar granites are enriched in silica, with SiO_2 values of 75.13 − 78.62 wt. %, the alkalis, where K_2O + Na_2O contents are 7.96 – 8.71 wt. %. Other compositional variability, include Al_2O_3, with values ranging from 11.44 to 12.49 wt. %, and Fe_2O_3 varying from 1.19 – 1.51 wt. %. They are depleted in MgO, with values ranging between 0.06 and 0.17 wt. %, CaO (0.23 – 0.86 wt. %), and TiO_2 (0.04 – 0.09 wt. %) relative to the Vredenburg Batholith. Major element variations of CaO, Fe_2O_3, K_2O, MgO, Na_2O, and Al_2O_3 are plotted against silica on Harker diagrams (Fig. 5.4). Only one linear trend is observed on the Harker plots, which is CaO decreasing as silica increases. This decrease in Ca content could be due to the crystallisation of plagioclase (Winter, 2001). The other elements all show varying degrees of scattering. When disregarding the two samples with relatively low SiO_2 contents (<76 wt. %) the K_2O variation is flat with increasing silica and NaO_2 shows a slight negative correlation.

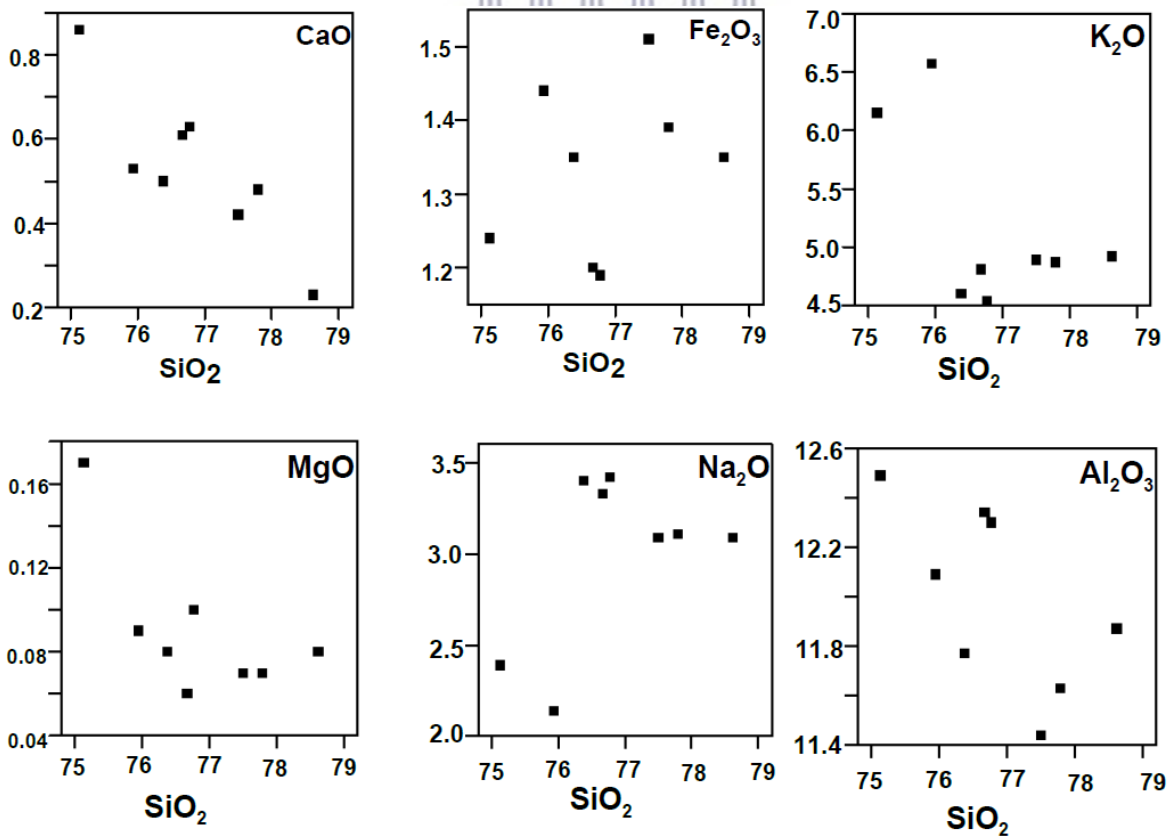

Figure 5.4: Harker plots for selected major elements for the alkali feldspar granites.

Table 5.2: Trace element compositions for the Vredenburg Batholith (granites and igneous enclaves) and Cape Columbine Granite (alkali feldspar granites).

Rock Type	***Granites***																					
Sample	PAT2	PAT10	PAT11	PAT14	PAT17	PAT19	PAT21	PAT22	PAT26	PAT29	PAT31	PAT33	PAT36	PAT37	PAT39	PAT41	PAT43	PAT51	PAT52	PAT55A	PAT55B	PAT56
Trace (ppm)																						
V	58	58	60	74	58	59	65	65	58	87	73	70	63	42	46	55	44	65	49	50	39	54
Cr	270	255	280	287	306	260	286	281	251	255	287	280	301	285	282	253	287	243	256	252	112	259
Co	8	9	25	10	6	6	7	7	10	9	8	8	7	4	5	5	4	6	6	5	7	7
Ni	17	18	24	17	21	14	18	18	17	18	18	19	18	16	15	12	16	21	20	16	11	20
Cu	14	30	25	23	23	13	26	18	10	20	29	28	28	16	14	13	15	29	19	17	14	12
Zn	61	74	68	75	65	59	65	60	59	73	74	76	74	53	62	85	56	80	61	60	108	66
Mo	18	15	16	17	19	15	17	17	17	15	18	17	17	18	17	16	17	17	17	17	8	16
Cs	4	3	5	5	5	7	6	8	4	5	6	5	4	7	3	10	4	9	6	7	8	6
Rb	166	171	180	178	189	193	185	184	173	139	169	156	212	224	199	222	195	342	291	302	372	274
Sr	131	139	133	152	130	139	135	136	134	181	145	157	120	77	100	87	92	211	157	150	87	148
Ba	666	804	723	831	810	949	912	859	734	892	910	868	712	442	534	260	504	1011	675	592	188	558
Nb	19	14	22	15	16	21	16	14	15	19	16	24	17	13	25	19	15	31	22	35	63	24
Zr	191	185	182	194	167	185	169	183	197	209	199	212	179	147	158	238	129	237	178	187	580	197
Hf	5	5	5	6	5	5	5	5	5	5	5	5	5	5	5	7	4	6	5	5	15	5
Ta	1	1	1	1	1	1	1	1	1	1	1	1	1	1	1	1	1	2	1	1	4	2
Pb	29	28	31	28	31	29	31	29	27	25	28	26	28	34	31	33	34	41	38	39	77	34
Th	18	21	20	22	20	20	20	20	21	15	19	21	19	21	21	29	25	42	47	48	37	55
U	4	1	3	4	3	2	3	3	4	2	2	2	2	5	4	5	4	18	11	10	10	10

Table 5.2. (*Cont.)*

Rock Type	***Igneous enclaves***													***Alkali feldspar granites***							
Sample	PAT4	PAT6	PAT7	PAT13	PAT15	PAT24	PAT25	PAT26A	PAT28	PAT30	PAT35	PAT50	PAT54	PAT18	PAT34	PAT38	PAT45	PAT46	PAT47	PAT48	PAT49
Trace (ppm)																					
V	62	83	136	58	63	83	87	155	85	85	52	64	77	35	28	31	26	35	33	31	31
Cr	252	235	189	230	239	237	238	229	258	198	300	215	175	290	290	293	268	338	344	303	311
Co	9	26	19	9	8	10	11	15	8	10	8	7	8	3	2	4	2	2	2	2	2
Ni	16	23	20	17	18	17	19	21	17	16	25	12	15	22	19	18	10	23	23	20	17
Cu	16	19	44	17	12	11	16	34	13	17	10	15	17	7	12	6	11	11	11	8	16
Zn	51	64	130	56	59	67	74	108	69	78	42	78	79	25	24	44	34	40	61	66	72
Mo	15	14	11	14	14	14	13	13	15	11	18	13	13	19	18	19	16	23	21	20	19
Cs	5	6	7	2	6	6	5	4	5	5	5	6	2	4	2	3	10	3	2	2	4
Rb	188	169	145	171	165	153	157	136	156	147	178	193	266	209	151	238	328	235	211	241	258
Sr	122	159	128	131	134	181	163	193	175	165	102	113	175	77	56	14	10	12	9	7	5
Ba	825	953	459	1080	831	1207	977	527	1078	866	470	405	524	411	509	10	17	44	34	40	14
Nb	15	16	27	18	24	14	19	19	19	21	14	19	28	6	4	17	15	23	32	28	26
Zr	230	256	281	225	243	316	298	266	309	286	174	181	326	191	128	184	83	166	155	167	149
Hf	6	7	7	6	7	8	8	7	8	7	5	5	9	5	4	4	4	7	7	8	6
Ta	1	1	1	1	1	1	1	1	1	1	1	1	1	1	0	2	2	2	2	2	2
Pb	32	27	18	28	27	26	24	14	25	23	34	28	42	39	39	45	38	30	33	39	44
Th	19	19	7	15	16	18	17	6	14	14	19	13	37	15	13	26	28	18	22	25	25
U	3	3	1	3	3	2	2	1	2	2	3	4	41	3	2	9	6	4	5	5	6

5.3 Trace Elements

5.3.1) Granites

Trace elements vary in abundance for the granites for selected elements such as the transition metals, V (42 – 87 ppm), large ion lithophile elements (LIL): e.g., Ba (260 – 1010 ppm), Sr (77 – 211 ppm) and Rb (139 – 342 ppm), and high field strength elements (HFSE): e.g., Nb (13 – 35 ppm), Zr (129 – 238 ppm) and Th (15 – 55 ppm). Trace elements are plotted against maficity in Fig. 5.5. Notable trends are observed between the data arrays. Elements controlled by the incongruent melting of biotite (Rb, Sr, Ba, and V) show variable relationships. V vs. Mg + Fe mimics the linear trend of the Ti:maficity plot (Fig. 5.3). However, other elements such as Rb, Ba, and Sr show poor correlations with maficity whether it is negative (Rb) or positive for the others (Fig. 5.5). The trends observed are due to: 1) their concentrations in the incongruent melting of the reactant phases and feldspars, 2) the number of reactant phases that are melted to produce the magma or melt, and 3) equilibration of the melt with biotite and feldspar residue crystals (Villaros et al., 2009b). Similarly, trace elements concentrated in accessory phases, such as Zr and Hf (in zircon), show good positive correlations, whereas the light rare earth elements (LREE) (in monazite) typically show a poor relationship when plotted against maficity for the Vredenburg Batholith as compared to the S−type Peninsular Pluton granites of South Africa (Fig. 5.5; Villaros et al., 2009b). The trend for the LREE could be due to the lack of monazite in the source. The trends observed in major and trace element data arrays for granites are a consequence of the co−entrainment of peritectic and accessory phases from the source (Clemens et al., 2011, Clemens and Stevens, 2012; Villaros et al., 2009b).

5.3.2) Igneous Enclaves

Similar to the major element trends of the host granite, the trace elements show similar to near identical trends as those of the host granite (Fig. 5.5). However, Zr and Eu concentrations at almost all maficity values are higher in the igneous enclaves than the host granites. This effect may be due to the fact that magmas that entrain more peritectic phases tend to entrain higher abundances of accessory phases, such as zircon (Clemens et al., 2017c, Villaros et al., 2009b), and, as for the Eu*, this might be an effect of the element going into the residual plagioclase.

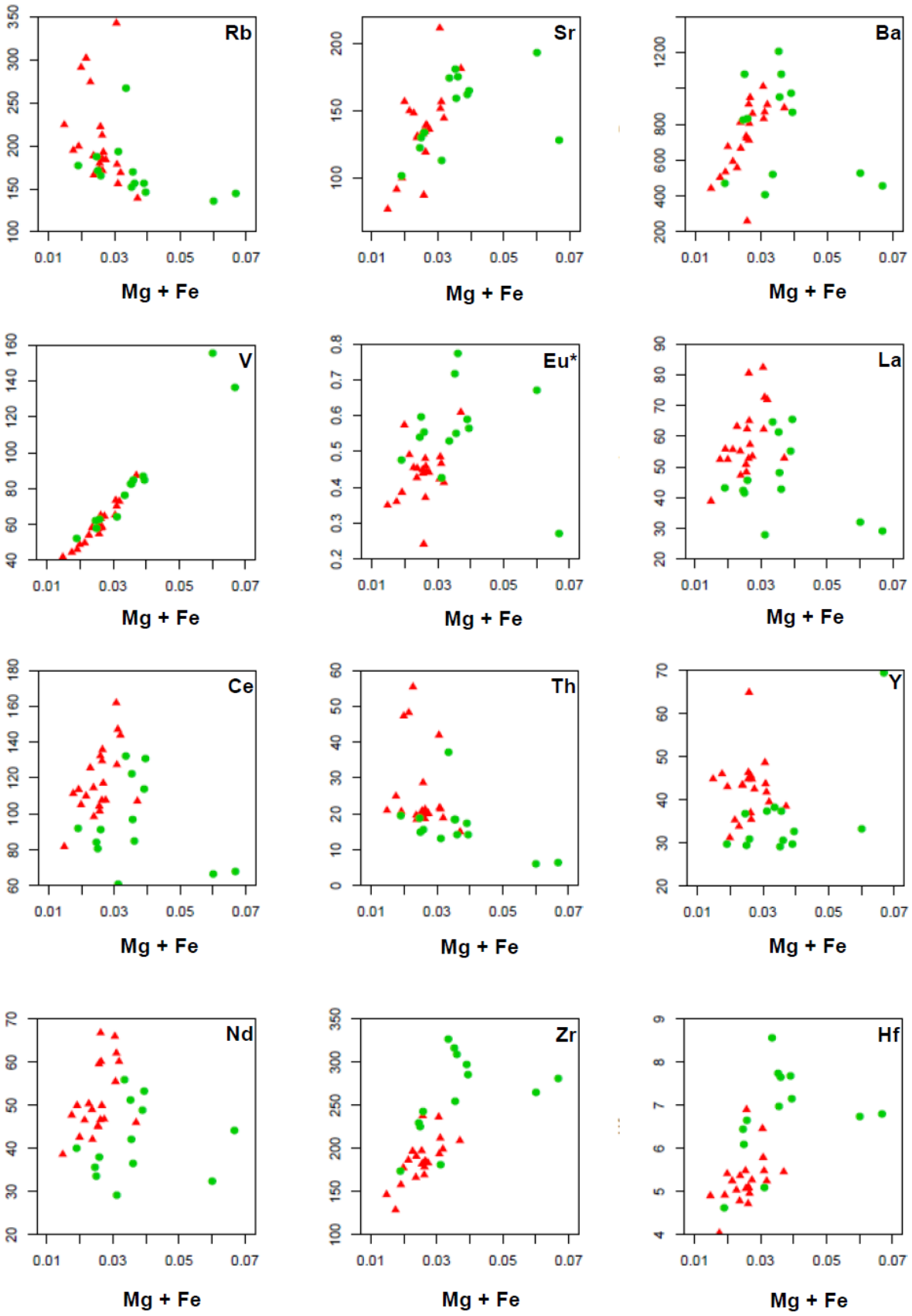

Figure 5.5 Bivariate plots for selected trace elements vs. maficity for the Vredenburg Batholith (granites and igneous enclaves). Red triangles indicate the granites and green circles the igneous enclaves.

5.3.3) Alkali feldspar granites

Trace element compositions are presented in Table 5.2 for the alkali feldspar granites. The alkali feldspar granites range in Ni and Cu between 10 – 23 ppm and 6 – 16 ppm, respectively. In addition, their Rb concentrations vary between 151 and a high of 328 ppm, and Sr values range from 5 − 77 ppm. On bivariate plots of trace elements vs. SiO_2, no well-defined positive trends are observed (Fig. 5.6) apart from Cr which has a moderate positive correlation (R^2 =0.64). However, several good negative correlations are observed [Ba (R^2 = 0.67), La (R^2 =0.79) and Sr (R^2 =0.74)], when excluding samples with high Ba and Sr values (PAT 18 and PAT 38).

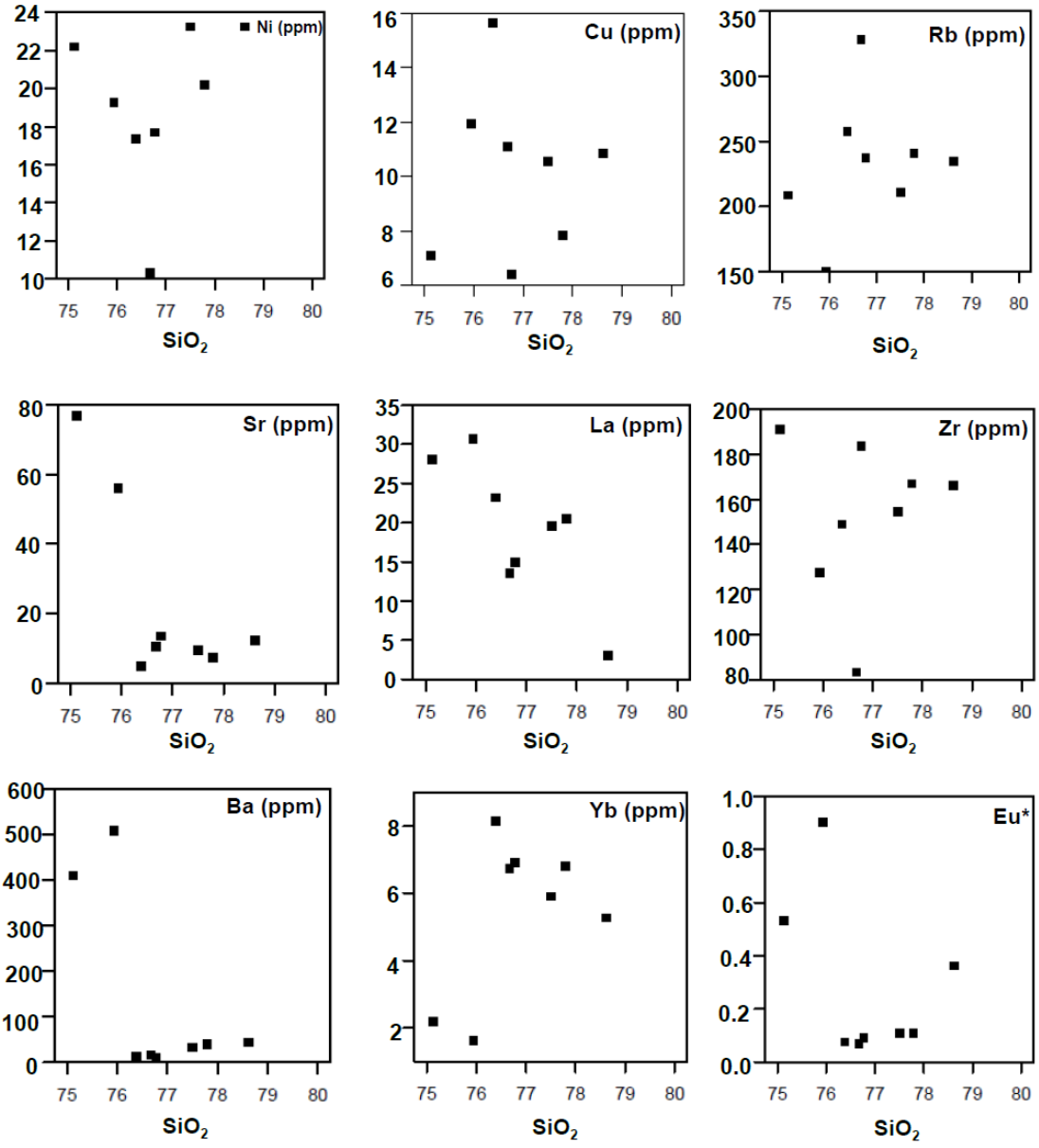

Figure 5.6: Bivariate diagrams of selected trace elements vs. SiO_2 for the Cape Columbine Granite (alkali feldspar granites).

Table 5.3: Rare earth element compositions for the Vredenburg Batholith (granites and igneous enclaves), and Cape Columbine Granite (alkali feldspar granites).

Rock Type	***Granites***																					
Sample	PAT2	PAT10	PAT11	PAT14	PAT17	PAT19	PAT21	PAT22	PAT26	PAT29	PAT31	PAT33	PAT36	PAT37	PAT39	PAT41	PAT43	PAT51	PAT52	PAT55A	PAT55B	PAT56
REE (ppm)																						
La	47,26	65,00	48,35	62,20	55,10	57,27	52,75	53,45	50,85	52,88	71,95	72,65	80,50	38,90	55,80	62,34	52,40	82,35	52,40	55,65	83,10	63,20
Ce	98,50	135,85	101,60	127,40	114,65	117,20	107,65	107,75	104,40	107,20	143,90	147,15	129,55	81,80	113,65	132,35	111,45	161,90	105,15	110,00	182,05	125,70
Pr	10,98	15,38	11,45	14,22	12,97	13,05	12,09	12,23	11,79	11,74	16,01	16,46	17,28	9,70	13,09	15,13	12,59	17,46	11,14	12,30	23,05	14,34
Nd	42,10	60,20	45,10	55,55	49,05	50,00	46,70	46,80	45,20	46,05	60,20	62,15	66,85	38,65	50,00	59,65	47,75	66,05	42,65	46,60	95,55	50,40
Sm	8,72	10,95	9,90	11,05	9,88	11,00	8,44	9,07	9,25	8,92	11,39	12,20	13,00	8,80	9,21	11,89	9,79	12,00	7,10	7,10	21,75	9,00
Y	43,40	35,49	46,42	43,80	43,49	44,85	37,06	42,55	44,83	38,55	39,58	41,85	45,65	44,90	43,09	65,00	46,09	48,70	31,25	35,35	110,00	33,85
Eu	1,22	1,47	1,31	1,59	1,24	1,42	1,24	1,20	1,30	1,63	1,36	1,62	1,43	0,91	1,08	0,88	1,04	1,44	1,21	1,16	1,20	1,20
Gd	7,69	8,76	8,29	9,07	7,91	8,68	7,38	7,60	8,44	7,50	8,86	9,24	10,63	7,16	7,92	10,25	7,96	9,00	5,85	7,35	18,50	7,15
Tb	1,23	1,29	1,29	1,29	1,26	1,30	1,10	1,28	1,27	1,17	1,30	1,29	1,59	1,10	1,24	1,68	1,17	1,30	0,95	1,16	3,06	1,07
Dy	8,00	7,96	8,27	8,45	7,94	8,44	7,12	8,01	8,18	7,41	7,61	8,42	9,00	8,15	7,83	11,03	7,77	8,14	5,46	5,92	19,40	5,74
Ho	1,62	1,40	1,75	1,67	1,61	1,59	1,38	1,57	1,63	1,40	1,45	1,64	1,77	1,57	1,65	2,24	1,60	1,67	1,12	0,98	4,04	1,32
Er	4,60	3,61	4,89	4,44	4,57	4,35	3,96	4,23	4,77	4,16	3,81	4,25	4,78	4,83	4,60	6,36	4,71	4,74	3,19	3,49	11,99	3,38
Tm	0,67	0,47	0,74	0,67	0,63	0,67	0,55	0,58	0,74	0,52	0,61	0,56	0,67	0,66	0,68	1,01	0,67	0,73	0,45	0,61	1,74	0,46
Yb	4,73	2,79	4,82	4,40	3,92	4,54	3,65	3,76	4,79	3,78	3,38	3,91	3,96	4,53	4,21	5,80	4,43	4,52	3,61	3,21	11,51	3,85
Lu	0,67	0,38	0,63	0,62	0,61	0,62	0,56	0,61	0,69	0,56	0,47	0,60	0,55	0,72	0,62	0,85	0,71	0,82	0,51	0,55	1,69	0,51
∑REE	237,96	315,50	248,37	302,60	271,33	280,11	254,55	258,11	253,28	254,90	332,28	342,12	341,54	207,46	271,55	321,42	264,01	372,10	240,78	256,06	478,62	287,30
$(La/Sm)_N$	3,41	3,74	3,07	3,54	3,51	3,28	3,93	3,71	3,46	3,73	3,97	3,75	3,90	2,78	3,81	3,30	3,37	4,32	4,64	4,93	4,32	4,42
$(Gd/Lu)_N$	1,43	2,87	1,63	1,82	1,61	1,75	1,65	1,56	1,51	1,67	2,36	1,91	2,40	1,24	1,60	1,50	1,40	1,36	1,44	1,68	1,75	1,76
Eu/Eu*	0,45	0,46	0,44	0,48	0,43	0,40	0,48	0,44	0,45	0,61	0,41	0,46	0,37	0,35	0,39	0,24	0,36	0,42	0,57	0,49	0,18	0,45

Table 5.3 *(Cont)*

Rock Type	***Igneous enclaves***													***Alkali feldspar granites***							
Sample	PAT4	PAT6	PAT7	PAT13	PAT15	PAT24	PAT25	PAT26A	PAT28	PAT30	PAT35	PAT50	PAT54	PAT18	PAT34	PAT38	PAT45	PAT46	PAT47	PAT48	PAT49
REE (ppm)																					
La	42,49	47,98	29,09	41,76	45,55	61,30	55,20	32,25	42,98	65,60	43,10	27,92	64,60	28,05	30,65	14,99	13,55	3,08	19,53	20,46	23,20
Ce	84,43	96,70	68,01	80,95	91,50	122,35	113,60	66,49	85,05	130,95	92,15	60,75	132,10	62,05	64,95	38,70	36,30	8,10	51,25	58,55	62,55
Pr	9,12	10,68	9,27	9,13	10,26	13,34	12,71	7,69	9,38	14,18	10,60	7,25	14,85	7,00	6,65	5,29	5,14	1,04	6,71	9,03	8,98
Nd	35,60	42,15	44,25	33,70	37,90	51,15	48,85	32,50	36,45	53,25	40,20	29,25	56,10	25,60	24,25	21,75	23,95	4,05	29,80	48,10	37,70
Sm	6,88	8,18	13,28	6,87	7,24	8,56	8,57	7,16	6,99	8,81	8,00	7,25	8,87	4,70	4,04	8,07	8,20	1,17	8,35	16,15	12,05
Y	36,82	37,49	69,55	29,45	31,01	29,25	29,88	33,43	30,80	32,82	29,75	37,44	38,40	20,45	12,92	55,90	70,10	31,75	68,60	56,90	90,25
Eu	1,17	1,34	1,18	1,23	1,22	1,74	1,50	1,55	1,62	1,51	1,09	1,00	1,43	0,74	0,93	0,24	0,21	0,19	0,33	0,55	0,30
Gd	6,39	6,71	13,32	5,76	6,18	6,42	7,06	6,95	5,85	7,52	6,05	7,03	7,64	3,88	2,43	8,47	10,45	2,09	10,27	14,55	12,55
Tb	1,00	1,05	2,09	0,91	0,87	0,96	1,03	0,94	0,89	1,09	0,99	1,13	1,09	0,69	0,39	1,68	1,98	0,56	1,82	1,86	2,23
Dy	6,36	7,29	14,35	5,62	5,78	6,01	6,12	6,06	5,63	6,46	5,50	6,91	6,73	3,73	2,13	10,09	12,20	4,67	11,98	10,76	12,94
Ho	1,31	1,38	2,64	1,12	1,15	1,03	1,15	1,23	1,08	1,24	1,12	1,52	1,46	0,75	0,48	2,20	2,41	1,11	2,48	2,22	2,70
Er	3,71	3,89	7,33	3,20	3,32	3,08	2,97	3,62	3,43	3,31	3,18	3,96	3,70	2,22	1,32	6,30	7,13	3,90	6,36	6,08	7,88
Tm	0,59	0,58	1,01	0,48	0,46	0,43	0,43	0,46	0,49	0,44	0,49	0,52	0,59	0,33	0,24	1,16	1,15	0,84	1,05	1,11	1,25
Yb	3,72	4,05	6,09	3,09	2,82	3,05	2,60	3,32	3,24	3,16	2,95	3,43	3,54	2,20	1,61	6,92	6,74	5,27	5,91	6,82	8,15
Lu	0,57	0,58	0,80	0,38	0,48	0,41	0,42	0,48	0,40	0,47	0,47	0,49	0,57	0,37	0,26	0,91	1,10	0,78	0,92	1,04	1,19
∑REE	203,32	212,67	232,53	194,17	214,69	279,82	262,18	170,67	203,46	297,97	215,88	158,39	303,23	142,28	140,32	126,74	130,50	36,83	156,74	197,26	193,66
$(La/Sm)_N$	3,89	1,38	3,69	3,82	3,96	4,51	4,05	2,84	3,87	4,69	3,39	2,42	4,58	3,76	4,78	1,17	1,04	1,66	1,47	0,80	1,21
$(Gd/Lu)_N$	1,39	2,07	1,43	1,91	1,62	1,93	2,12	1,81	1,81	2,00	1,59	1,80	1,68	1,30	1,17	1,16	1,18	0,33	1,39	1,74	1,31
Eu/Eu*	0,54	0,55	0,27	0,59	0,55	0,72	0,59	0,67	0,77	0,56	0,48	0,42	0,53	0,53	0,90	0,09	0,07	0,36	0,11	0,11	0,07

5.4 Rare earth elements and spider diagrams

5.4.1) Granites

The REEs are normalised to the chondritic values of Boynton (1984) (Fig. 5.7 A). The LREE slope shows a slightly steep negative slope, with $(La/Sm)_N$ values ranging from 2.78 – 4.93, and an average of 3.77. The heavy rare earth elements (HREE) are typified by a flat trend, with $(Gd/Lu)_N$ values between 1.24 and 2.87, with an average of 1.72. Overall the REE pattern is gently negatively sloping [$(La/Yb)_N$ = 9.91]. The Eu anomaly is negative and ranges from 0.18 – 0.61.

The granite samples have all been normalised to the primitive−mantle−normalised values of Sun and McDonough (1989). The granites typically show a gentle decreasing slope from left to right (incompatible to compatible elements) (Fig. 5.7 B). The decrease is not straightforward as there are many anomalies in the form of peaks and valleys in the trends. Overall the pattern shows enrichment in the LILE over the HFSE. The valleys are defined by depletion in the LIL elements Ba, Sr, and Eu, and the HFS elements Nb, P, and Ti. The peaks are typified by enrichment in the LIL element Rb, and the HFS elements Cs, Th, U, and Pb.

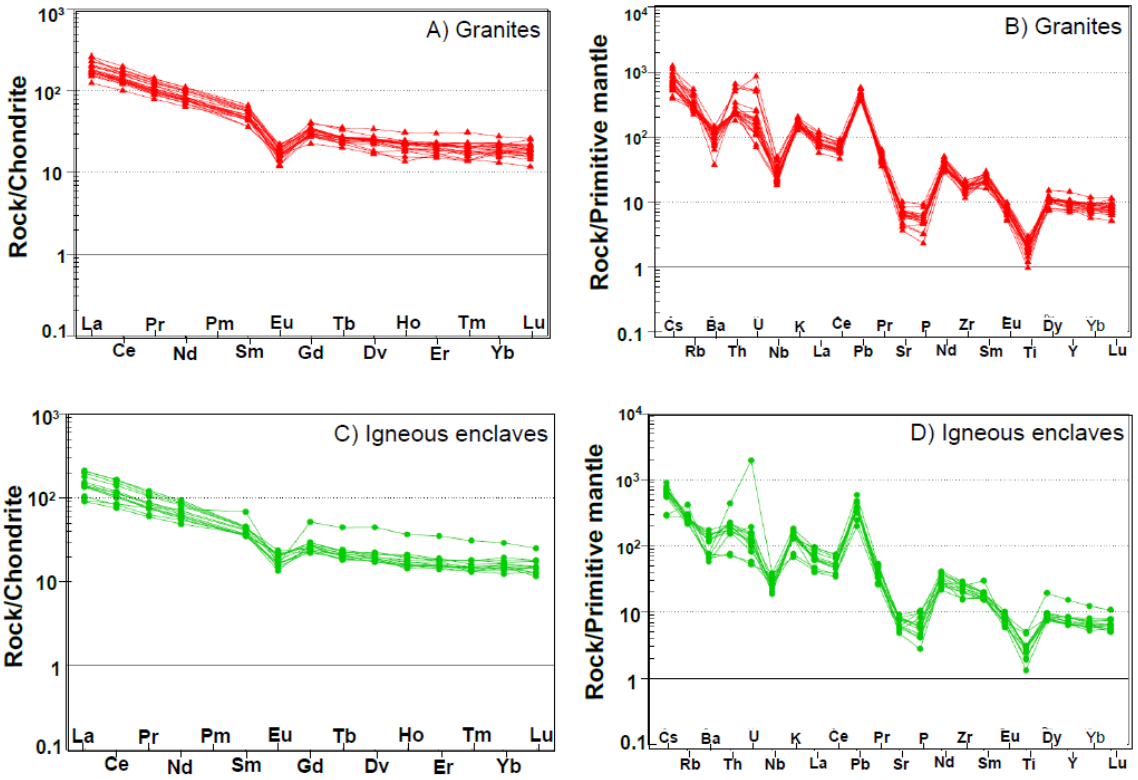

Figure 5.7: Chondrite−normalised REE diagrams and Primitive mantle−normalised multi−element diagrams for the Vredenburg Batholith granites (A and B) and igneous enclaves (C and D). Normalising values for chondrite are from Boynton (1984) and for primitive mantle are from Sun and McDonough (1989).

5.4.2) Igneous enclaves

Rock/chondrite diagrams of REE normalisation (Boynton, 1984) for the igneous enclaves illustrate identical trends to the host granite rock/chondrite normalisation trends (Fig. 5.7C). Their REE concentrations are given in Table 5.3. The samples of the igneous enclaves show a similar slightly steep negative slope as the host granites in terms of LREE enrichment [$(La/Sm)_N$ = 1.38 – 4.69], and the same gentle slope for the HREE as the host granite with $(Gd/Lu)_N$ values from 1.39 – 2.12, with moderate to strongly negative Eu/Eu* anomaly values (0.27 – 0.77) (Fig. 5.7 A and C).

On the primitive mantle−normalised multi-element diagram (Fig. 5.7 D) all samples were normalised to the primitive mantle values of Sun and McDonough (1989). Similar trends are observed as in the host granite with identical depletion trends in the elements Ba, Nb, Sr, P, Eu, and Ti, and enrichments in Ce, Rb, Th, U, and Pb. Similarly to the major and trace element plots there is a great degree of overlap between the enclaves and host granites in the REE plots and spider diagrams.

5.4.3) Alkali feldspar granites

Chondrite−normalised REE diagrams for the Cape Columbine Granite (alkali feldspar granites) show the typical seagull trends of ferroan granites (A−type) when compared with the chondritic values of Boynton (1984) (Fig. 5.8 A). The alkali feldspar granite samples are enriched in the LREE with gentle decreasing slopes and $(La/Sm)_N$ values ranging from 1.03 – 4.77, with one sample showing a low $(La/Sm)_N$ value of 0.79. The HREE show flat patterns with $(Gd/Lu)_N$ values from 1.16 to 1.74], with one sample (PAT 46) having a $(Gd/Yb)_N$ value as low as 0.33. All the alkali feldspar granite samples exhibit strongly negative Eu anomalies [$(Eu/Eu^*)_N$ = 0.06 – 0.09)].

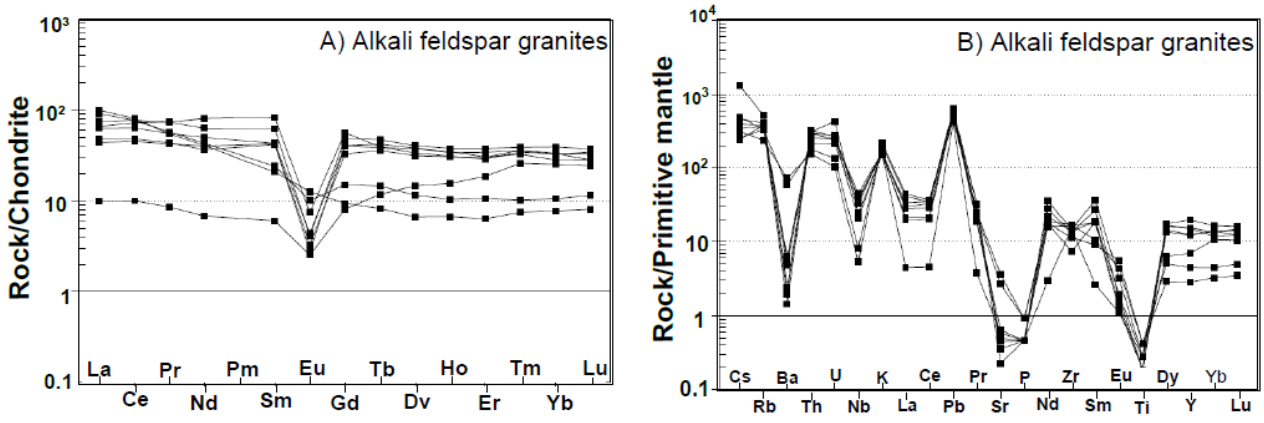

Figure 5.8: A) Chondrite−normalised REE diagram and B) Primitive mantle−normalised multi−element diagram for the Cape Columbine Granite. Normalising values for chondrite are from Boynton (1984) and for primitive mantle are from Sun and McDonough (1989).

Primitive mantle−normalised multi−element plots of the alkali feldspar granites (Fig. 5.8 B) show a gentle decreasing slope from Cs to Lu. The slope, however, is not smooth, and there are several negative and positive anomalies present. The diagram shows depletion in the LIL elements Ba, La, Ce, Sr, and Eu, for the HFS elements P and Ti. The samples of alkali feldspar granites show enrichment of the LIL element K and the HFS elements Th, U, and Pb.

5.5 Sr and Nd isotopes

Six samples were analysed for Sr−Rb and Sm−Nd isotopes. Two samples from each rock type were sampled. All samples analysed for isotopic concentrations are presented below in Table 5.4. εNd_t values were calculated using U−Pb SHRIMP age data from da Silva et al. (2000) for the I-type Vredenburg Batholith, and, since there is no age data for the enclaves associated with the granites, for this study it was assumed that they formed coevally with the host granites (t = 540 Ma). The age data for the Cape Columbine Granite (t= 525 Ma) was taken from Chemale et al. (2011) to calculate the εNd_t values.

5.5.1 Granites

The granites yield $^{87}Sr/^{86}Sr_{(t)}$ values between 0.7397 − 0.7488. The $^{87}Rb/^{86}Sr$ ratios range from 3.371 − 4.717 In addition, their epsilon concentrations for initial Sr ($^{87}Sr/^{86}Sr_{(i)}$ = 0.7125 – 0.7138) and values for today ($\varepsilon Sr_{(t)}$= 120.2548 – 138.5821). The $^{143}Nd/^{144}Nd_{(t)}$ values are relatively consistent ranging from 0.5121 − 0.5122, corresponding to $\varepsilon Nd_{(t)}$ values from -3.57 to -3.13. T_{CHUR} model ages range from 0.88 – 0.89 Ga and T_{DM} ages from 1.54 – 1.59 Ga.

5.5.2 Igneous enclaves

The Sr isotopes of the enclaves in comparison to the host granites show a greater range in $^{87}Sr/^{86}Sr_{(t)}$ (= 0.7396 to 0.7520), $^{87}Rb/^{86}Sr$ (=3.286 − 5.347), $^{87}Sr/^{86}Sr_{(i)}$ (=0.7108 – 0.7143), and $\varepsilon Sr_{(t)}$ (96.0 to 146.2. The Nd isotope analysis of the enclaves indicates identical $^{143}Nd/^{144}Nd_{(t)}$ values to the host granites (0.5121 − 0.5122), but with higher $\varepsilon Nd_{(t)}$ values (-3.48 to -0.56), and younger T_{CHUR} model ages of 0.58 – 0.87 Ga and T_{DM} ages of 1.14 – 1.52 Ga.

5.5.3 Alkali feldspar granites

The two alkali feldspar granite samples analysed for Sr−Rb isotopes show a large range in $^{87}Sr/^{86}Sr_{(t)}$(=0.7688 to 1.2451), $^{87}Rb/^{86}Sr$ ratios of 7.208 and 59.505, $^{87}Sr/^{86}Sr_{(i)}$ (= 0.7147 and 0.7999), and an extreme range in $\varepsilon Sr_{(t)}$ values from -16263 to 161. Their $^{143}Nd/^{144}Nd_{(t)}$ ranges from 0.51218 to 0.51244 which translates to $\varepsilon Nd_{(t)}$ values of-3.03 to -2.01. Model ages of 0.80 to 1.10 Ga and 1.43 to 2.44 Ga for T_{CHUR} and T_{DM}, respectively are older than for the granites and enclaves.

Table 5.4: Whole−rock Sr−Nd isotopic data for the Vredenburg Batholith (granites and igneous enclaves) and, Cape Columbine Granite (Alkali feldspar granites)

Sample ID	Rock Type	Age (Ma)[a]	Rb (ppm)	Sr (ppm)	$^{87}Rb/^{86}Sr$	$^{87}Sr/^{86}Sr(i)$	±2σ	Sm (ppm)	Nd (ppm)	$^{147}Sm/^{144}Nd$	$^{143}Nd/^{144}Nd(i)$	±2σ	$f^{Sm/Nd}$	$^{143}Nd/^{144}Nd(t)$	εNd(i)[b]	εNd(t)[a,c]	T_{CHUR}[e]	T_{DM}[d]
PAT 2	Granite	540	166.40	131.10	3.371	0.7397	15	8.72	42.10	0.1253	0.511782	12	-0.36	0.512225	-8.06	-3.13	0.88	1.59
PAT 36	Granite	540	212.20	119.50	4.717	0.7488	11	13.00	66.85	0.1176	0.511760	16	-0.40	0.512176	-9.02	-3.57	0.89	1.54
PAT 15	Igneous enclaves	540	165.40	133.70	3.286	0.7396	17	7.24	37.90	0.1155	0.511764	12	-0.41	0.512172	-9.09	-3.48	0.87	1.52
PAT 55A	Igneous enclaves	540	301.85	149.95	5.347	0.7520	13	7.10	46.60	0.0922	0.511914	15	-0.53	0.512240	-7.77	-0.56	0.58	1.14
PAT 18	Alkali feldspar granite	525	208.80	76.95	7.208	0.7688	18	4.70	25.60	0.1109	-0.000382	12	-0.44	0.512188	-8.78	-3.03	0.80	1.43
PAT 47	Alkali feldspar granite	525	211.25	9.43	59.505	1.2451	15	8.35	29.80	0.1695	-0.000583	14	-0.14	0.512441	-3.83	-2.01	1.10	2.44

[a] Based on U/Pb zircon ages (Chemale et al., 2011 and references therein)

[b] Calculated using $^{143}Nd/^{144}Nd$ today = 0.512638 with $^{146}Nd/^{144}Nd$ = 0.72190, $\varepsilon Nd(i) = ((^{143}Nd/^{144}Nd_{(t)}/0.512638)-1) \times 10000$

[c] $\varepsilon Nd(t) = ((^{143}Nd/^{144}Nd_{(sample,\ t)}/^{143}Nd/^{144}Nd_{(CHURt)})-1) \times 10000$

[d] $T_{DM} = 1/(\lambda) \times \ln(1+(^{143}Nd/^{144}Nd_{(sample,\ t)}-^{143}Nd/^{144}Nd_{(DM,\ t)})/^{147}Sm/^{144}Nd_{(sample,\ t)}-^{147}Sm/^{144}Nd_{(DM,\ t)}) \times 0{,}000000001$ (after DePaolo, 1981)

[e] $T_{CHUR} = 1/(\lambda) \times \ln(1+(^{143}Nd/^{144}Nd_{(sample,\ t)}-^{143}Nd/^{144}Nd_{(CHUR,\ t)})/^{147}Sm/^{144}Nd_{(sample,\ t)}-^{147}Sm/^{144}Nd_{(CHUR,\ t)}) \times 10^9$ (after DePaolo, 1981)

where t is the time of emplacement of the granite.

5.6 Tectonic discrimination diagrams

Tectonic diagrams help clarify the tectonic environment in which the rocks formed. In the past mainly trace elements were used to determine the tectonic settings of felsic igneous rocks (i.e. Pearce et al., 1984). However, in recent years this method of distinguishing the settings for igneous rocks has been challenged, mainly due to the inconsistent results produced by these trace element diagrams (Verma, 2010). Moreover, the data used in defining the Pearce et al. (1984) diagrams are not treated statistically thus giving them a variable degree of inaccuracy, especially for felsic rocks (Verma, 2012). Therefore, the tectonic setting diagram analysis for this study incorporates methods introduced by Verma et al. (2013) to determine the tectonic setting of felsic rocks of the Vredenburg Batholith and Cape Columbine Granites.

Table 5.5: Five discriminant−function−based multi−dimensional discrimination diagrams for the Vredenburg Batholith and Cape Columbine Granites, where IA = island arc, CA = continental arc, CR = continental rift, OI = ocean island, and Col = collision.

Locality	Tectonic diagram	Total number of samples	Number of discriminated samples [x ± s of probability values](range of probability values for samples)				
			IA+CA	IA	CA	CR+OI	Col
Vredenburg/Paternoster	**(IA+CA-CR+OI-Col)**	32	2 [0.3564±0.0053] (0.3526, 0.3601)	---	---	15 [0.463±0.073] (0.3649-0.5756)	15 [0.469±0.084] (0.3726-0.6133)
Vredenburg/ Paternoster	**(IA-CA-CR+OI)**	32	---	0 (0)	4 [0.5320±0.0418] (0.4844-0.5693)	28 [0.641±0.111] (0.4807-0.8399)	---
Vredenburg/ Paternoster	**(IA-CA-Col)**	32	---	0 (0)	2 [0.4866±0.0130] (0.4774, 0.4957)	---	30 [0.647±0.117] (0.4611-0.8911)
Vredenburg/ Paternoster	**(IA-CR+OI-Col)**	32	---	0 (0)	---	23 [0.528±0.048] (0.4721-0.6233)	9 [0.557±0.056] (0.4493-0.6258)
Vredenburg/ Paternoster	**(CA-CR+OI-Col)**	32	---	---	10 [0.406±0.050] (0.3385-0.4847)	12 [0.444±0.061] (0.3594-0.5422)	10 [0.467±0.081] (0.3839-0.5885)
Vredenburg/ Paternoster	**{Σn} {Σprob} [%prob]**	**160**	**{2} {0.7127} [---]**	**{0} {0} [0%]**	**{16} {7.1587} [9.1%]**	**{78} {42.3473} [49.1%]**	**{64} {36.1234} [41.8%]**
Cape Columbine	**(IA+CA-CR+OI-Col)**	8	0 (0)	---	---	8 [0.837±0.083] (0.7274-0.9319)	0 (0)
Cape Columbine	**(IA-CA-CR+OI)**	8	---	0 (0)	0 (0)	8 [0.975±0.048] (0.8658-0.9989)	---
Cape Columbine	**(IA-CA-Col)**	8	---	0 (0)	0 (0)	---	8 [0.948±0.081] (0.7697-0.9943)
Cape Columbine	**(IA-CR+OI-Col)**	8	---	0 (0)	---	8 [0.829±0.071] (0.7312-0.9101)	0 (0)
Cape Columbine	**(CA-CR+OI-Col)**	8	---	---	0 (0)	8 [0.849±0.060] (0.7691-0.9193)	0 (0)
Cape Columbine	**{Σn} {Σprob} [%prob]**	**40**	**{0} {0} [0%]**	**{0} {0} [0%]**	**{0} {0} [0%]**	**{32} {27.9096} [79%]**	**{8} {7.5816} [21%]**

5.6.1 Vredenburg Batholith (granites and igneous enclaves)

Figure 5.9 and Table 5.5 indicates that the setting for the granites is complex and most likely represents a transitional tectonic setting from collisional to within−plate. In total 32 samples (20 granite and 12 of the igneous enclaves) qualified (SiO_2>65%) and were plotted on the five tectonomagmatic diagrams of Verma et al. (2013). The total number of samples (∑n=160) plot mainly in the within−plate (continental rift and oceanic island), collisional, or continental arc fields (Table 5.5). Sixteen samples plot in the continental arc fields on the IA-CA-CR+OI, IA-CA-Col and CA-CR+OI-Col diagrams (Fig. 5.9 B, C & D) with a much greater probability than the continental arc field probability (∑prob =7.1587). Two samples plot in the combined arc field for granites and enclaves (on the IA+CA-CR+OI-Col diagram (Fig. 5.9 A; Table 5.5)) with an extremely low probability of ∑prob =0.7127. Since no samples plot in the IA field on any of the diagrams, it is possible to eliminate the possibility that any of the samples are derived from an island arc, and, therefore, of the ∑prob =0.7127 probability, 100% of the samples are in the continental arc field. The largest of the sample distributions plot in the continental rift and oceanic island field, and the collision fields, being ∑n =78 with the highest ∑prob =42.35 and ∑n =64 with a relatively high ∑prob =36.12, respectively. Fifteen samples each plot in both fields on the IA+CA-CR+OI-Col diagram, twenty eight samples in CR+OI field on the IA-CA-CR+OI diagram, thirty samples plot in the Col field on the IA-CA-Col diagram, twenty three samples in the CR+OI field and nine samples in the Col field (IA-CR+OI-Col diagram), and twelve samples in the CR+OI field and ten samples in the Col field on the CA-CR+OI-Col diagram (Fig. 5.9). The diagrams (Fig. 5.9) and Table 5.5 still render some ambiguity with regards to the settings of the granites and enclaves. However, a transition from a collisional to a within−plate environment can be inferred.

5.6.2 Cape Columbine Granites (alkali feldspar granites)

In total eight samples of the ferroan granites were analysed and all samples are indicative of a single setting (Fig. 5.9 and Table 5.5). The total number of samples, ∑n=40, mainly plot in the within−plate (continental rift and oceanic island) fields. Thirty-two samples, of the total 40 samples for five diagrams plot in the continental rift and oceanic island fields (all eight in the IA+CA-CR+OI-Col, IA-CA-CR+OI, IA-CR+OI-Col and CA-CR+OI-Col diagrams) with high probabilities ∑prob. =27.9096 (Fig. 5.9). Eight samples plot in the collisional field with ∑prob. =7.5816 in the IA-CA-Col diagram (Fig. 5.9C). However, it should be noted that the IA-CA-Col diagram does not have a field that accommodates a within−plate setting, therefore, this particular plot may not be reliable as the data has to plot in some field on the diagram by default. Moreover, the total probability percentage for within−plate settings account for 79%, which is much greater than the 21% for collisional settings (Table 5.5).

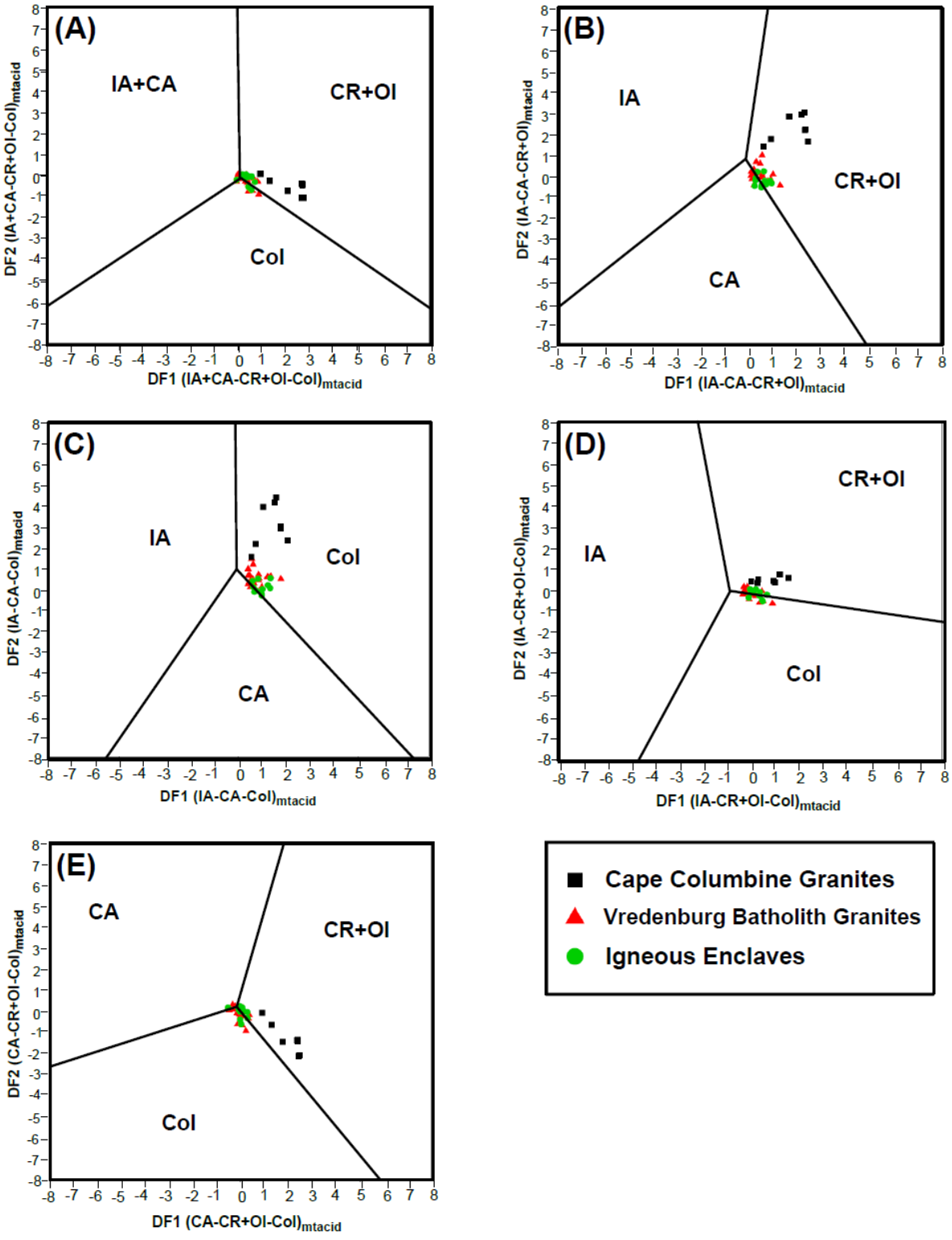

Figure 5.9: Discriminant–function multi–dimensional discrimination diagrams based on natural log–transformed ratios of immobile major and trace elements (after Verma et al., 2013). The "mtacid" subscript in the axis labels refers to major and trace element ratios. a) IA+CA–CR+OI–Col diagram. (b) IA–CA–CR+OI diagram. (c) IA–CA–Col diagram. (d) IA–CR+OI–Col diagram and (e) CA–CR+OI–Col diagram. IA–island arc; CA–continental arc; IA+CA–combined island and continental arcs, i.e., arc setting; CR–continental rift; OI–ocean island; CR+OI –combined continental rift and ocean island, i.e., within-plate (WP) setting; Col–collision.

5.7 Summary of Geochemistry

Vredenburg Batholith

Granites

- The granites are magnesian to ferroan, calc−alkalic to alkali−calcic, weakly peraluminous and display chemical variability for major and minor elements (SiO_2: 63.24 − 72.74 wt. %, K_2O: 3.86 − 6.70 wt. %, Na_2O: 2.88 – 3.26 wt. %, CaO: 1.26 – 3.02 wt. %, TiO_2: 0.21 – 0.87 wt. %, MgO + FeO_t: 2.63 – 10.30);selected trace elements: Zr: 128 − 580 ppm, Th: 15 −55 ppm and La: 39 −83 ppm.
- They display positive correlation trends for the major elements Ti, Ca and P, and the trace elements V, Ba, Sr and Zr vs. maficity.
- They display negative correlation trends for the major elements Si and K, and trace elements Rb and Th vs. maficity.
- LREE values show a gradual negative slope [$(La/Sm)_N$ = 3.7], with a large negative $(Eu/Eu^*)_N$ (0.18 −0.61), and the HREE have a gentle negative slope [$(Gd/Lu)_N$ = 1.4].
- Isotope chemistry is characterised by strongly negative εNd_t values (-3.57 to -3.13) which corresponds to T_{DM} model ages of 1.54 to1.59 Ga.
- Their tectonic setting indicates a transitional setting for the granites and the enclaves, with a high percentage probability indicating that the granites formed in a collisional setting (%prob. = 41.8%), with a large number of samples indicating a within−plate setting (%prob. = 49.1%), with the remaining percentage indicative of an island arc setting (%prob. =9.1%).

Igneous enclaves

- The igneous enclaves are magnesian, calc−alkalic to calcic and weakly peraluminous to metaluminous and the chemical composition is similar to the host granites.
- Moreover, the geochemical trends between the major and trace elements are identical to the host granites.
- The LREEhave a similar negative slope (average $(La/Sm)_N$ = 3.6), higher negative $(Eu/Eu^*)_N$ (0.27 − 0.77), and the HREE have a slightly steeper slope [$(Gd/Lu)_N$ = 1.9].
- Their εNd_tvalues have a greater range (-3.5 to -0.5) with model ages the same as the granites.

Cape Columbine Granite

Alkali feldspar granites

- Their lithochemical characteristics are: ferroan, calc−alkalic and weakly peraluminous.
- Positive correlations are observed for the trace elements Ni, Cr, and Zr when plotted against SiO_2.
- The data array shows negative relationships for the major elements CaO, MgO, Na_2O, and Al_2O_3, and for the trace elements Sr, Rb, La, and Yb when plotted against silica.
- They are enriched in the LREE with gentle positive slopes, with $(La/Sm)_N$ values ranging from 1.03 – 4.77, along with negative Eu anomalies (Eu/Eu* = 0.06 – 0.09), and slightly negative to flat HREE values [$(Gd/Lu)_N$ values from 1.16 to 1.74].
- Their isotopic signatures indicate $\varepsilon Nd_{(t)}$ of -3.03 to -2.01, that corresponds to model ages of 1.43 to 2.44 Ga for T_{DM}.
- The tectonic setting for the alkali feldspar granites almost all plot in the within−plate field. This setting corresponds to high probabilities (Σprob. =27.9096) and percentage probabilities (%prob. = 79%).

Chapter 6 Discussion

6.1 Introduction

The following chapter consists of interpretation of the results. From the geochemical and isotopic data inferences will be made on the sources, petrogenesis, and tectonic setting for the Vredenburg Batholith and the Cape Columbine granites.

The structure of the chapter is as follows: the chapter is separated into three sections for each of the geological interpretations (e.g. sources). These sections are further split into two subsections. The subsections will contain a description for the rock groups under investigation. It should be noted that, although in the introduction various models for I−type and A−type (ferroan) granite magma generation is described, in the *Petrogenesis* section three models will be tested for I−type granites and one model for ferroan granites to explain chemical variation observed.

6.1 Sources

6.1.1 Vredenburg Batholith (granites and IEs)

Previous studies (da Silva et al., 2000; Chemale et al., 2011) suggest that the Phase II magmas from the CGS resulted from melting of an older Eburnian or Namaquan crust, or by mixing between an Eburnian-aged basement source and variable amounts of juvenile crustal source. The late− to post−collisional I−type granites have U−Pb ages of ~540 Ma and have T_{DM} and $\varepsilon Nd_{(t)}$ values of 1540 to 1590 Ma and -3.57 to -3.13, respectively. The igneous enclaves have a similar $\varepsilon Nd_{(t)}$ value of -3.48 and a slightly negative value (-0.56) with corresponding T_{DM} ages of 1520 and 1140 Ma, respectively. It might seem at this point that the outlier (PAT 55A) is within the enclaves i.e. the sample that reflects a slight negative $\varepsilon Nd_{(t)}$ and younger T_{DM} age. However, these $\varepsilon Nd_{(t)}$ and T_{DM} age for the granites and enclaves coincides with the $\varepsilon Nd_{(t)}$ and T_{DM} age reported for the I−type granites by Chemale et al. (2011). This suggests that the enclaves have a crustal origin as for the granites, rather than a contrasting mantle source (Fig. 6.1 A) and discussed in the following subsection (*Petrogenesis; I−type granites; magma mixing*). The isotopic composition of the granites and enclaves, thus, indicate sources from the reworking of juvenile igneous crustal material from the Mesoproterozoic eras, as proposed by da Silva et al. (2000) and Chemale et al. (2011). This hypothesis is further supported by the $\varepsilon Nd_{(i)}$ vs. $Sr_{(i)}$ diagram (Fig. 6.1B) which indicates enriched crustal sources for the granites and enclaves.

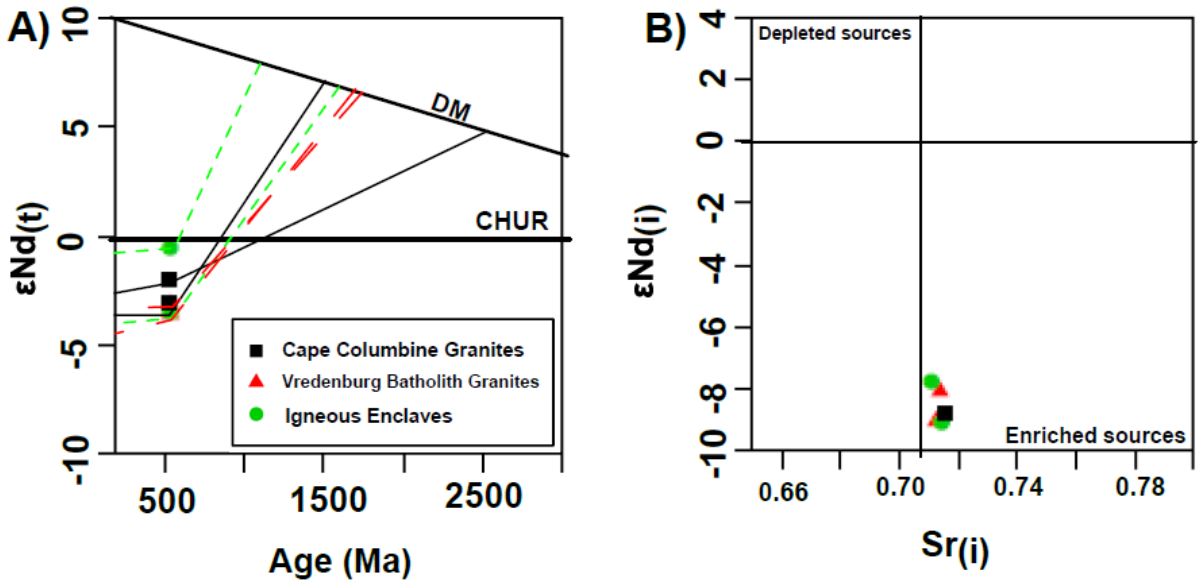

Figure 6.1: A) Age (Ma) vs. $\varepsilon Nd_{(t)}$ diagram for the Vredenburg Batholith (granites and igneous enclaves) and Cape Columbine Granite (alkali feldspar granites) with thick solid lines representing the depleted mantle (DM) and chondritic uniform reservoir (CHUR) (after DePaolo, 1981). The red long dashed line represents the granites, green short dashed lines are the igneous enclaves and the thin solid black lines indicate the alkali feldspar granites. B) $Sr_{(i)}$ vs. $\varepsilon Nd_{(i)}$ diagram for the Vredenburg Batholith (granites and igneous enclaves) and Cape Columbine Granite (alkali feldspar granites).

6.1.2 Cape Columbine Granite (alkali feldspar granites)

The post−collisional alkali feldspar granites have an emplacement age of 525 Ma (Chemale et al., 2011) which translates to negative $\varepsilon Nd_{(t)}$ values (-2.01 to -3.03) and Meso- to Paleoproterozoic T_{DM} model ages of 2440 and 1430 Ma. This indicates that both samples are derived from a mixture of juvenile and more mature crustal sources (Fig. 6.1A). The $\varepsilon Nd_{(i)}$ vs. $Sr_{(i)}$ diagram (Fig. 6.1B) indicates that the alkali feldspar granites all plot in the enriched source field reflecting crustal components. Thus, the results of this study support the results of Chemale et al. (2011) and Scheepers (1995), as they suggested variable amounts of mixing between juvenile sources and, melting of a granulitic crustal component. Melting of the juvenile source can be attributed to the rifting and mantle upwelling inferred (*section 6.3*). It is suggested that a Namaquan crust was melted by asthenospheric upwelling of the mantle beneath the crust forming the ferroan magmas. The mantle source providing the heat for melting was most likely the same as which generated the intermediate to mafic plutons associated with the CGS (Clemens et al., 2017a).

6.2 Petrogenesis

6.2.1 Vredenburg Batholith

The granites of the Vredenburg Batholith have silica contents ranging from 62.24 – 72.74 wt. %, exhibit high−K values (3.86 – 6.70 wt. %), and are weakly peraluminous. All these characteristics are typical of I−type granitoids (Chappell and White, 1974; Frost et al., 2001). Chemical variability in I−type granites has been attributed to a variety of processes involving mantle−derived magmas (Clemens et al., 2016, also, see chapter 1 for an overview). Some of these processes include fractional crystallisation of a mantle-melt accompanied by assimilation of crustal material, magma mixing between a crustal and mantle melt, and, more recently, coupled entrainment of peritectic and accessory phases (PAE) in a peraluminous crustally derived melt (Clemens and Stevens, 2012; Clemens et al., 2011; Clemens et al., 2016; Villaros et al., 2009b). In fact, fractionation of a mantle−melt has been suggested to have caused the chemical variability displayed by the I−type granites of the Cape Granite Suite (Scheepers, 1995), of which the Vredenburg Batholith forms a part. Such a model does not seem to correlate with the new data presented for this thesis. Here it can be shown that the primary process involved in the chemical variation of the Vredenburg Batholith can be attributed to PAE. However, this does not negate that such magma chamber processes, such as fractional crystallisation and magma mixing, have not played a role in granite genesis, as will be shown.

6.2.1.1 Fractional Crystallisation

The trends observed on Harker plots (see Appendix E) show a moderate to strong decrease in CaO, Fe_2O_3, TiO_2, MgO, P_2O_5, and MnO with increasing silica content. These trends are indicative of crystallisation of plagioclase, biotite and accessory apatite from a parental magma which would have produced the Vredenburg Batholith granites. Moreover, trace element models indicate trends for mineral assemblages that will crystallise from a granitic melt (Cai et al., 2011; Rollinson, 1993). In Figure 6.2 trace element models are used, which suggests variable degrees of fractional crystallisation has occurred. The Rb vs. Sr diagram (Fig. 6.2A) shows similar crystallisation trends as the Harker plots, where the main mineral assemblage that differentiated from the magma is plagioclase and biotite, with the addition of hornblende. In the Ba versus Sr plot (Fig 6.2C) the main mineral phases which crystallised out of the melt to cause the compositional variations were alkali feldspar and hornblende. And undoubtedly, field evidence of mafic mineral cumulates (*see Chapter 4*) is evidence that fractionation has occurred. In addition, peraluminous granites can be produced by fractionation of hornblende from a lesser aluminous precursor magma (Clemens et al., 2016). However, chemical fractionation was not the primary control on the chemical variability of the granites, as will be described below.

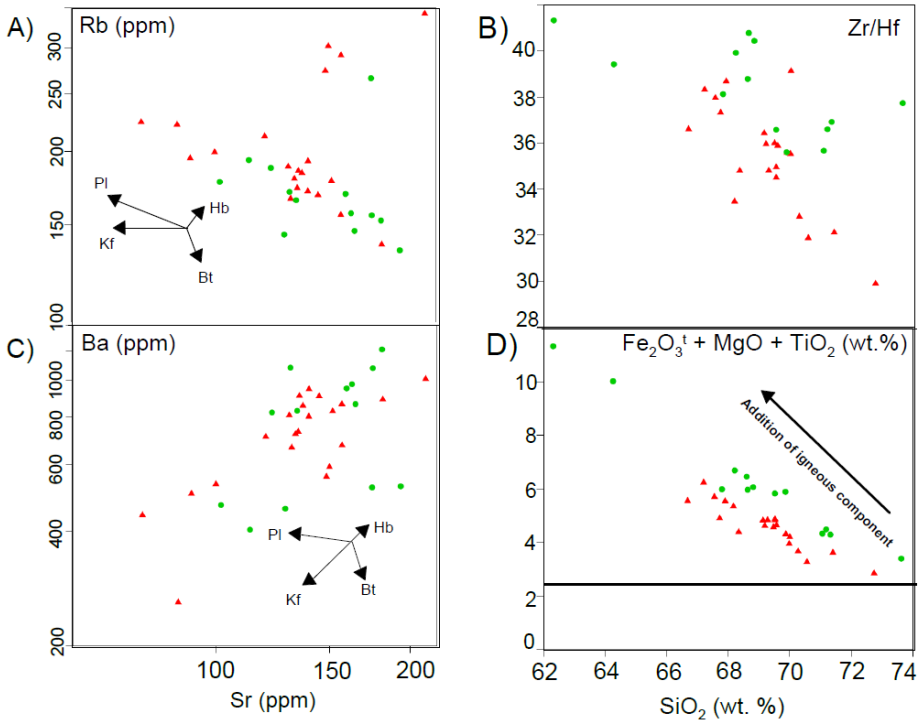

Figure 6.2: Fractionation vector diagrams (after Cai et al., 2011; Rollinson, 1993). A) Rb–Sr. B) Zr/Hf versus SiO_2. C) Ba–Sr. D) $Fe_2O_3^t$ +MgO + TiO_2 versus SiO_2. Symbols are the same as in Fig 6.1.

Firstly, peraluminous granites that would result from fractionation of such a magma would be rather small in volume (Chappell et al., 2012; Clemens et al., 2016). Such a suggestion would seem unlikely, given the large size of the mildly peraluminous Vredenburg Batholith. Secondly, the enclaves are unlikely to represent the magma from which the granites formed as they are less aluminous. However, chemically the enclaves and the granites typically show similar ranges for silica content (62.31 – 73.62 and 66.68 – 72.74 wt. %, respectively), and on the Harker plots (Appendix E) and $Fe_2O_3^t$ + MgO + TiO_2 vs. SiO_2 plot (Fig. 6.2D) the granites and enclaves have parallel trends. In some cases, such as the maficity plots (Figs. 5.3, 5.5), there is a considerable degree of overlap between the two for certain major (e.g. Ti and Ca) and trace (e.g. V) elements. Thirdly, Figure 6.2b shows the decrease in trace element ratios constrained by zircon (Zr and Hf) with increasing SiO_2 for both the granites and enclaves which is not compatible with fractional crystallisation (Cai et al., 2011). The trend may, however, indicate source heterogeneity or magma mixing (Cai et al., 2011). Finally, the trace element plot of Ba vs. Pb (Fig. 6.3) indicates that the granites and the enclaves are products of melts with progressive temperature increase. The line annotated by "fractionation" shows the trend produced by fractionation of biotite and feldspars, of which neither the granites nor enclaves follow the trend. This implies that fractional crystallisation was not the main cause of chemical variation, as suggested previously by Scheepers (1995).

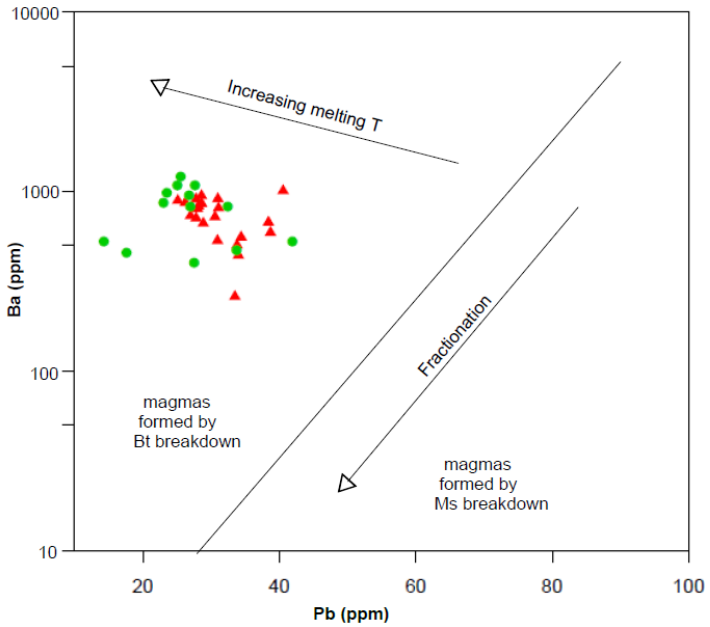

Figure 6.3: Log Ba versus Pb concentrations for the Vredenburg Batholith, from Clemens et al., (2016), after Finger and Schiller (2012). The diagram illustrates magmas formed by partial melting of sources containing biotite (Bt) or muscovite (Ms) as well as granites formed from fractionation. Symbols are the same as for Fig. 6.1.

6.2.1.2 Magma mixing

Magma mixing between a felsic crustally derived magma and a mafic mantle-derived magma has gained worldwide acceptance and became favoured for explaining chemical variability in granitoids with I−type affinities (Barbarin, 1999). This model has been further supported by the presence of mafic enclaves in most granitic plutons (Barbarin, 1999; Clemens and Stevens, 2012). The role of magma mixing played will be investigated in the following text.

A magma mixing model would be invoked based on the field evidence. In the outcrop there are significant volumes of what appears to magma mixing/mingling zones (Fig. 4.3), however, it should be noted that although the mingling zones are voluminous, relative to the Vredenburg batholith they are quite small. These zones are interpreted to represent mingling between a ferroan, weakly peraluminous, alkali−calcic granite magma and a metaluminous, magnesian, calc−alkalic magma represented by the enclaves. Their lithochemical characteristics are undoubtedly an indication of different sources. Thus, it can be taken into consideration that what was mapped as enclaves (IE1) could potentially represent a mantle-derived magma. However, the lithochemical and isotopic data of the enclaves show no mantle connection.

They have high SiO_2 contents (>67%), with the exception of PAT 7 and PAT 26a (62.31 and 64.26, respectively), and they have high K_2O, CaO and LREE values. Moreover, their isotope data [Sr_i (0.7108 − 0.7143) and εNd_t (-0.55 and -3.48)] are indicative of enriched crustal sources.

Therefore, it is suggested that what was mapped as enclaves (IE1) is not derived from a mantle magma, but rather they reflect anatexis of a heterogeneous source. Clemens et al. (2011) suggested that potential sources for I−type magmas are typically produced from rocks associated with volcanic arcs. These associated sources range from intermediate igneous rocks (dacites and andesites) with an admixture of up to 70% metagreywackes (Clemens et al., 2011, 2016). On this basis, it is then suggested that the metaluminous, magnesian, calc−alkalic enclaves represent melting of dacites and/or andesites, and the ferroan, weakly peraluminous, alkali−calcic granites reflect partial melting of a metagreywacke source. Therefore, a magma mixing model of crustal− and mantle−derived magmas seems to be out of favour.

Further corroboration that rules out a magma mixing model is based on chemical modeling between magmas derived from mantle and crustal sources. Associated with the Cape Granite Suite (CGS) are intermediate and mafic plutons (Scheepers, 1995). These intermediate to mafic intrusives are most likely the best representatives of mantle magma addition to the CGS. Thus, they can be used to test if any mixing between crustal and mantle magmas occurred, to produce the chemical variability displayed by the granites.

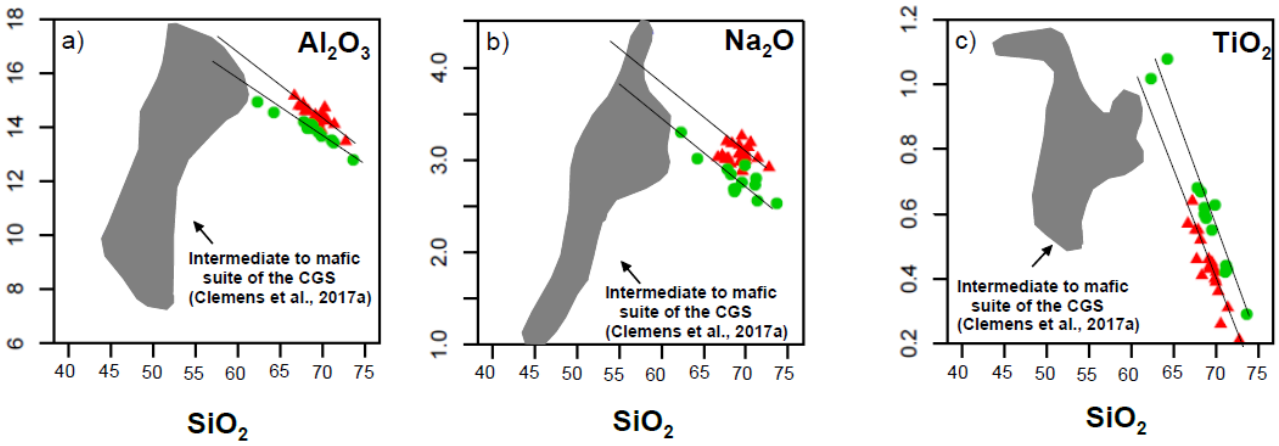

Figure 6.4: Harker plots for the variation of a) Al_2O_3, b) Na_2O and c) TiO_2 for the Vredenburg batholith granites (red triangles) and igneous enclaves (green circles). The grey shaded area is geochemical data for the intermediate to mafic associations of the Cape Granite Suite (CGS) (from Clemens et al., 2017a).

Figure 6.4 indicates that there is no connection between the intermediate to mafic plutons and the I−type granites. The trends on the Al_2O_3, Na_2O, and TiO_2plots for the granites and the enclaves rarely extrapolate back into the intermediate and mafic pluton fields (Fig. 6.4). This further substantiates the idea that magma mixing was not the cause of chemical variation observed. However, the magma mingling zones cannot be ignored. Therefore, it is suggested that magma mixing played a role in chemical variation, just that the magma mixing/mingling occurred locally between crustal magma pulses from distinct sources.

6.2.1.3 Co−entrainment of peritectic and accessory phases

Finally, the co−entrainment of peritectic and accessory phases into anatectic melts to account for the chemical diversity of the Vredenburg batholith is investigated. The major element trends displayed by the Vredenburg Batholith mimics that which have been explained for other I−type granite suites worldwide inferred to have been produced by peritectic assemblage entrainment (Clemens and Stevens, 2012; Figs. 5.3, 6.5). Figure 6.5 illustrates positive trends for Ti and Ca, and a strong negative correlation for ASI and K with increasing maficity for the Vredenburg Batholith. This indicates that the entrained phases must have consisted of Ca−Ti−Mg−Fe peritectic assemblages (Farina et al., 2012). The high K values at low maficity (pure melt) are accounted for by the principal reactants during anatexis (Clemens et al., 2011). These high K concentrations are evidence that the granites were not formed by melting of a mafic magma, as the melting of such rocks produces magmas that are highly sodic (Clemens et al., 2011; Clemens and Stevens, 2012).

An increase in calcium and the decrease of ASI vs. maficity are observed in the granites and enclaves (Fig. 6.5 C and D). These trends were suggested to be a function of the entrainment of clinopyroxene by the incongruent melting of hornblende in an intermediate source (Clemens et al., 2011; Farina et al., 2012). A positive linear correlation between titanium (Ti) and maficity is exhibited in the granites as well as the enclaves (Fig. 6.5 B). This relationship is a hallmark feature of the model (Clemens et al., 2011). This chemical relationship has been attributed to be a product of incongruent melting of biotite resulting in the peritectic phase ilmenite (Clemens et al., 2011).

Thus, combined incongruent melting of these biotite and amphibole reactants can be used to infer a peritectic assemblage of:

$Bt + Hbl + Qtz + Pl^1 = melt + Pl^2 + Cpx + Opx + Ilm \pm Grt$. (Clemens et al., 2011).

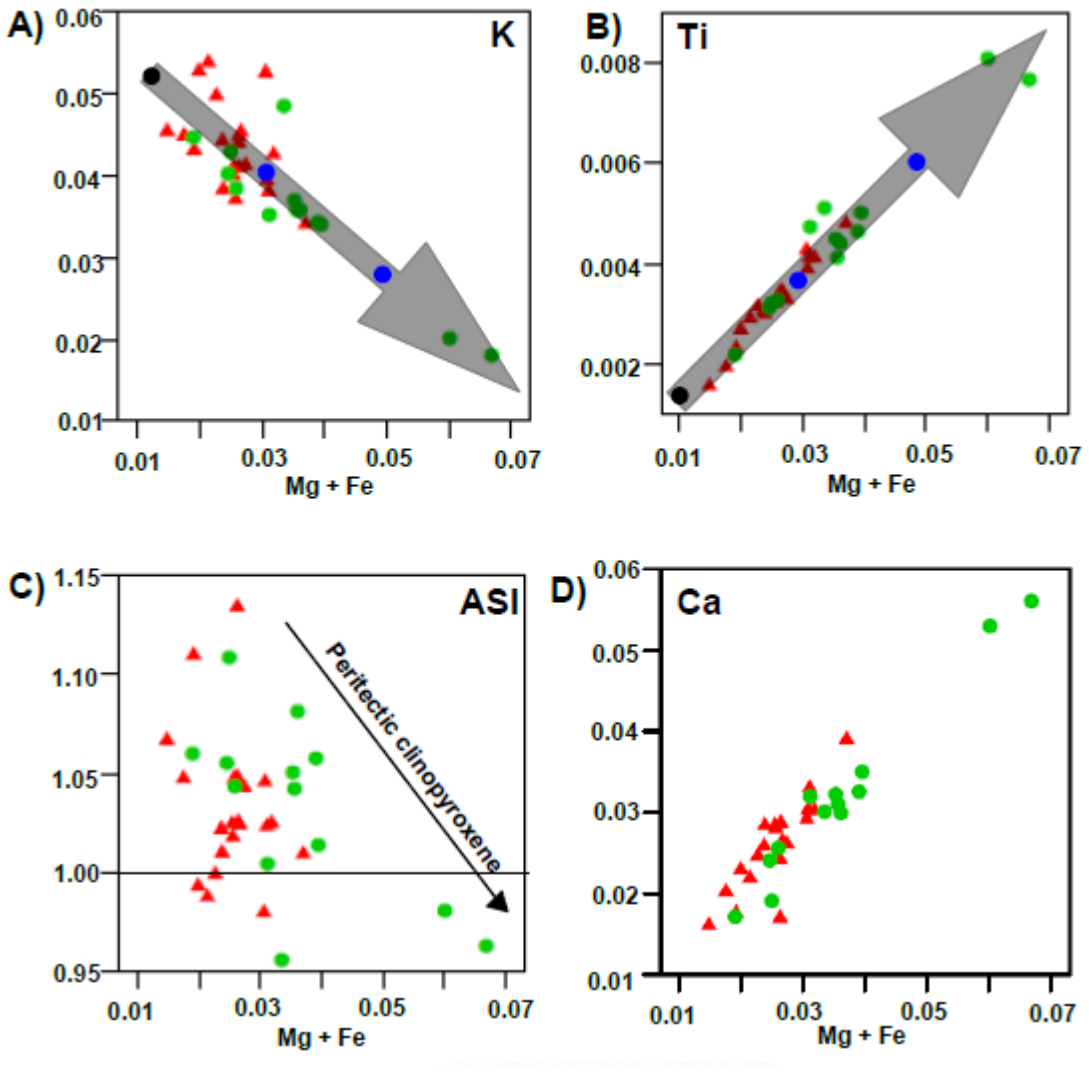

Figure 6.5: Peritectic assemblage entrainment model diagrams. A and B) K and Ti vs. maficity plots for the I–type granite (red triangles) and igneous enclaves (green circles) comparing trends in the Vredenburg Batholith with model trends for magmas produced by peritectic assemblage entrainment in broadly K–rich andesitic systems in which both biotite and hornblende melt. The black dots indicate melt compositions as determined by Clemens and Stevens (2012). The blue dots show the magma compositions produced by entrainment of 5 and 10 mol%, respectively of peritectic assemblage produced by incongruent melting of biotite (after Clemens and Stevens, 2012). C) ASI vs. maficity plot. The solid black line shows the distinction between peraluminous (ASI > 1) and metaluminous (ASI < 1). D) Ca vs. maficity.

Trace element compositions, such as Zr and Hf, show positive correlations with increasing maficity (Fig. 5.5). This trend was explained by Villaros et al. (2009b) who suggested that this is a function of zircon liberation from biotite during melting in the source that gets entrained with the peritectic assemblages. However, in the same study (Villaros et al., 2009b), they suggested that LREE elements (La, Ce, and Pr) are controlled by monazite entrainment and would reflect good positive correlations with increasing maficity. Positive correlations are observed for La, Ce and Pr with maficity (Fig. 5.5, Pr not plotted) thus suggesting that coupled entrainment of accessory phases occurred.

These trends observed for major and trace elements are evidence that coupled entrainment of at least ~7 − 10% peritectic phases (ilmenite and clinopyroxene) and accessory phases (zircon and monazite) accompanying weakly peraluminous to metaluminous melts produced by anatexis of andesites or dacites with an admixture of greywacke is compatible with describing the chemical variation in the Vredenburg batholith. It should be noted at this point that petrographically the peritectic phases may not be seen. This is due to the fact that these minerals will equilibrate with the melt at crustal *P−T* conditions, as emphasised by Zarrebini (2016). As for the accessory phases, they tend to dissolve until saturation is reached. Typically zircon saturation is reached relatively early which explains the presence of xenocrystic zircons, however, monazite saturation is hardly reached and therefore they tend to dissolve completely (Villaros et al., 2009b).

6.2.2 Cape Columbine Granite

The alkali feldspar granites of the Cape Columbine Granite are silica enriched (>75 wt. %), ferroan, calc−alkalic, have high alkali values ($Na_2O + K_2O$) (7.96 – 8.71 wt. %), and have high REE contents. All these characteristics are consistent with the classification schemes of ferroan granites which differ from those for S- and I-type granites (Eby, 1990; Frost and Frost, 2011; Loiselle and Wones, 1979). Ferroan magmas can be produced by various processes (Frost and Frost, 2011). However, alkali feldspar granites are calc−alkaline as well. This narrows down the chemical variation of the granites to a single process, notably partial melting of a quartzofeldspathic crust.

6.2.2.1 Partial Melting of crust

The alkali feldspar granites classify as A2 ferroan granites as defined by the new scheme suggested by Grebennikov (2014) (Fig. 6.6). Note that this A2 classification is not synonymous to the A1 and A2 classification defined by Eby (1990, 1992). The nature of A2 ferroan granites are siliceous and typically located in extensional zones of intracontinental and continental margin settings. In addition, their chemical affinities depend on the degree of permeability of the crust to allow mantle magma to penetrate it for melting to occur (Grebennikov, 2014). The magmas are produced by crustal thinning and extension of the lithospheric crust which is melted by mantle magmas underplating the lithospheric crust and/or by mantle magma infilling gaps. These granitoid genetic processes usually occur after collisional processes have ceased (Grebennikov, 2014).

In addition, the A2 granites which are related to rift systems have been categorised by two main structural processes, being simple shear and pure shear (Buck et al., 1988). In the first category, strain as a result of shearing only occurs in the subhorizontal plane, and in the latter crustal thinning is due to

extension in both lateral directions (Grebennikov, 2014). Here it is then suggested that the latter process is responsible for the generation of the alkali feldspar granites. This inference is supported by the tectonics of the Saldania Belt described in this study and by Kisters et al. (2002). The results of these studies suggest that the last phases of the Cape Granite Suite plutonism occurred in a post−collisional, extensional tectonic setting, almost identical to that for the A2 types described by Grebennikov (2014).

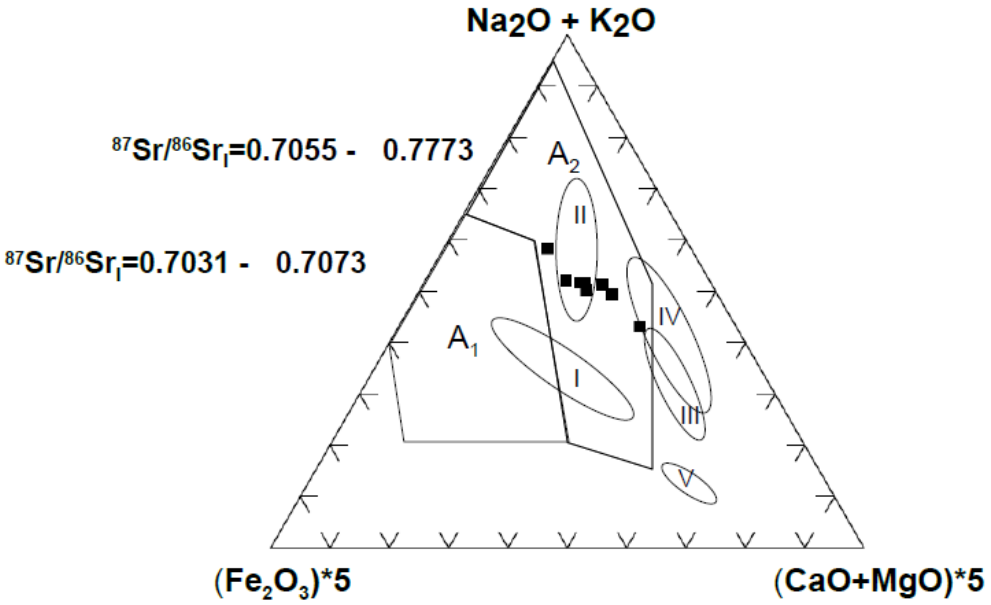

Figure 6.6: Diagram of (Na_2O + K_2O)–Fe_2O_3 ×5–(CaO + MgO) ×5 (mol.) to determine the nature of A-type granites (from Grebennikov, 2014). *A*1, Field of silicic rocks of within-plate geodynamic settings: oceanic islands and continental rifts; *A*2, felsic igneous rock associations of intracontinental and continental-margin geodynamic settings. Roman numerals mark the fields of felsic igneous rocks of major geodynamic settings, after Naumov et al. (2010): I, zones of mantle plumes in oceanic plates (oceanic islands and lava plateaus); II, intracontinental rifts and continental hot spots; III and IV, zones of subduction processes (III, zones of island-arc magmatism in oceanic crust; IV, zones of magmatism of active continental margins, involving continental crust in magma formation; V, back-arc spreading. The Cape Columbine Granites are indicated by the black squares.

Further corroboration that the alkali feldspar granites were produced by melting crustal material is based on their lithogeochemical features. The alkali feldspar granites classify as ferroan, calc−alkalic and weakly peraluminous according to the classification of Frost et al. (2001). Fig. 6.7 illustrates the various processes involved to produce granitoid magmas with the lithogeochemical characteristics it exhibits. There are two processes suggested in the schematic Fig. 6.7. The first process is the differentiation of basaltic magma, as inferred by Frost and Frost (1997, 2011), to produce metaluminous

magmas only, which requires a significantly voluminous amount of mafic source which will be associated with the pluton and which would have been emplaced coevally (Zhou et al., 2017). No such observation of large mafic bodies were made for the ferroan granites of this study and, therefore, it is not considered. This, therefore, enables the petrogenesis of the alkali feldspar granites to be narrowed down to a single process, namely partial melting of the crust.

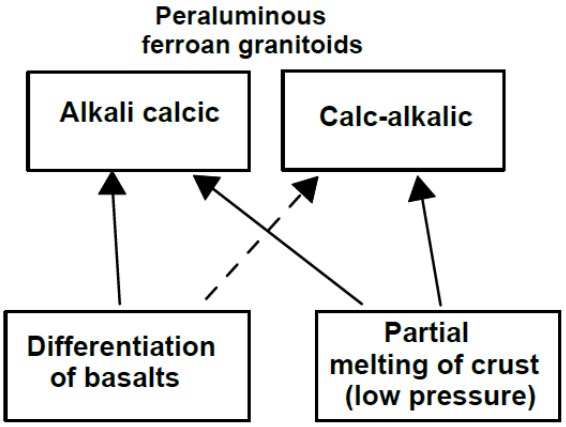

Figure 6.7: Schematic illustrating the petrogenesis of peraluminous ferroan granites (after Frost and Frost, 2011).

The generation of peraluminous, calc−alkalic ferroan granites through partial melting of calc−alkaline rocks was emphasised by Skjerlie and Johnston (1993). They investigated the melt products which would be produced by anhydrous melting of a tonalitic gneiss source rock with ~20% biotite and ~2% hornblende at pressure conditions which would represent mid−crustal conditions (between 6 and 10 kbars). The results obtained by Skjerlie and Johnston (1993) indicated that, at high pressures (10 kbars) the melts were strongly ferroan, tend towards alkali−calcic compositions, and are peraluminous at high melt content but move toward metaluminous compositions as the partial melting continues. Alternatively, relatively low pressure and high degrees of partial melting of tonalite−gneiss rock composition will produce ferroan, calc−alkalic and peraluminous melts. Therefore, it was suggested that in order to produce ferroan magma with the lithogeochemical signatures observed, similar to those of the Cape Columbine Granite, low pressures, and high temperatures are required and this most likely occurs at mid−crustal levels (i.e. rift settings). Therefore, of the chemical models described above to investigate the major petrogenetic processes that contributed to the chemical diversity of the Cape Columbine Granites, the composition of these granites can be attributed to the partial melting of crustal

material. This inference is based on chemical affinities, tectonic setting and melt sources determined in this study and the significant degree of correspondence of the models presented.

6.3 Tectonic settings

The amalgamation of the Kalahari and Rio de la Plata Cratons during the closing of the Adamastor Ocean (Gondwana supercontinent formation) has been widely accepted as the event for the formation of the Saldania Belt. The Cape Granite Suite (CGS) represented the granitoid intrusions associated with this orogenic belt on the basis of the geochronology of the granitoid phases and structural data (Kisters et al., 2002; Frimmel et al., 2011; Rozendaal et al., 1999). Associated with the closing of the Adamastor Ocean is a progression from continental−continental collision to extensional tectonics (Kisters et al., 2002). There is a large degree of overlap between the main phases of collisional tectonism (at ~550 to ~530 Ma) and the granitic emplacement ages of the CGS (at ~550 to ~525 Ma) (Kisters et al., 2002; Chemale et al., 2011). These tectonomagmatic events allowed many authors (Kisters et al., 2002; Rozendaal et al., 1999) to relate the magmatic phases to the types of tectonic events that caused their emplacement. Scheepers (1995) and Kisters et al. (2002) suggested that the I−type granites coincide with late− to post−collisional tectonics, whereas the A−type (ferroan) granites are suggested to be post-collisional in terms of time of emplacement. In addition, the setting for the granitic emplacement of the I−type granites has been suggested to be subduction−related and formed in an island arc setting, whereas the A−type granites are envisaged to have formed in a continental extensional rift setting caused by mantle upwelling during the strike−slip reversal of the Colenso Fault (Kisters et al., 2002; Scheepers, 1995; Rozendaal et al., 1999). However, these inferences were made as a consequence of the similarities of the CGS rocks and other tectonic settings for various granite types globally (Scheepers, 1995).

The I−type granites and the enclaves of the Vredenburg Batholith were emplaced during a transition from collisional to an extensional setting. Based on the statistical tectonomagmatic analysis (*subsection 5.6*) a larger probability percentage of the sample population plot in the within−plate (continental rift + ocean Island) settings ([%prob.] = 49.1%) than a collisional setting ([%prob.] = 41.8%). These findings are consistent with the suggestions made by Kisters et al. (2002) and are in contrast to the island arc and active continental margin suggestions of Scheepers (1995). The latter suggestion (active continental margin) still holds, but it does not depict the whole situation as it does not incorporate the continental collision setting. Kisters et al. (2002) reported geochronological and structural data for the Darling granites (older S−types) which constrained the emplacement of the earlier phases to the waning stages of the continental collisional tectonics after the closing of the Adamastor Ocean. Moreover, they report that the final exhumation of the Saldania Belt occurred at ~520 to ~510 Ma. This

was succeeded by the sedimentation of the Klipheuwel Group overlying the Malmesbury Group in a rift−type setting. They noted the temporal overlap between the collisional settings of the S−type tectonics and the sedimentary rift settings, and therefore, suggested that extensional tectonics may have occurred by ~540 Ma. This age also coincides with the ages of the I−type and A−type granites of this study (da Silva et al., 2000; Scheepers 1995). The suggestion by Kisters et al. (2002) of a transitional setting from collisional to extensional tectonics is further supported by the findings of this study. Therefore, a transition from collisional to within−plate (continental rift) setting is inferred for the granites and enclaves of the Vredenburg Batholith. In addition, Kisters et al. (2002) and Scheepers (1995) report continental rift tectonic settings for the A-type granites of the CGS. The statistical results of this study attest to their findings. The analysis of the alkali feldspar granites of the Cape Columbine Granite indicate a within−plate setting with an extremely high probability percentage ([%prob.] = 79%). It is here suggested that after the transition from collisional to extensional tectonics occurred well within the age constraints of the A−type granites (~530 to ~525 Ma) and therefore, their tectonic setting is most likely rift-related, as suggested Kisters et al. (2002) and Scheepers (1995).

Chapter 7 Conclusion

From the geochemical analysis and models created for the Vredenburg Batholith and Cape Columbine Granites, the findings of this study can then be summarised as follows:

7.1) Vredenburg Batholith

1) The Sr and Nd isotopic analysis of the host granites and enclaves indicate that the magmas which generated both of these igneous intrusives are from an admixture of crustal sources. The host granites and enclaves have similar εNd_t values with corresponding Mesoproterozoic Nd model ages. This indicates variable degrees of mixing between Paleoproterozoic, possibly reworked crustal material and younger juvenile Mesoproterozoic material. A likely interpretation is they then likely formed due to direct crustal melting of a Namaquan crust.
2) The petrochemical process responsible for the compositional variation is attributed to co−entrainment of peritectic assemblages and accessory phases (PAE) from the source; as opposed to the fractional crystallisation model suggested by Scheepers (1995). Evidence for PAE stems from the geochemical trends observed for the major elements Ti, Ca and ASI, and the trace elements Zr, Hf and the LREE vs. maficity. The major element trends are indicative of coupled incongruent melting of biotite and hornblende producing peritectic ilmenite and clinopyroxene. The trace elements are attributed to the entrainment of zircon and monazite followed by subsequent dissolution. Thus, the geochemical data collected in this study provides evidence that magmatic−chamber processes, such as fractional crystallisation and magma mixing between two crustal heterogeneous sources played a minor role in the chemical variation of the Vredenburg Batholith.
3) Based on new major and trace element tectonomagmatic diagram analysis, the tectonic setting indicates a transition from collisional to a within−plate, rift−related setting. This finding agrees with the findings of Kisters et al. (2002) and opposes the suggestion of an island arc setting by Scheepers (1995).

7.2 Cape Columbine Granite

1) The granites have varying Nd model ages ranging from 2440 to 1430 Ma, with εNd_t values of -2.01 and -3.03. This suggests they might have had varying age sources, one of a juvenile or younger origin (1.5 Ga) and an older source (2.4 Ga). This implies that the 1430 Ma T_{DM} of the granites could, potentially, have been produced by mixing of a 50:50 ratio of older Namaquan (2250 Ma) and younger Malmesbury Group (550 Ma) material to give rise to the isotopic model ages. Moreover, the Cape Columbine Granite's isotopic systematics indicates an enriched

crustal source. This is evidence for the petrogenetic model used to explain the chemical variation.

2) On the models mentioned, partial melting of quartzofeldspathic crustal material at low pressure is suggested to be the main petrogenetic process involved in the geochemical compositions displayed by the Cape Columbine Granites.
3) The inferred tectonic setting for the Cape Columbine Granites shows that they were emplaced in a within−plate setting. This suggestion supports the findings of previous studies (e.g. Scheepers 1995; Kisters et al., 2002).

7.4 Future suggestions

It is noted that due to time and financial limitations that some important analyses were not conducted, such as geochronology, Hf−Lu isotopes, structural interpretations, mineral chemical analysis and phase equilibrium modeling. Therefore, it is suggested that for future studies on the Vredenburg Batholith new geochronological analysis be done on the host granites and enclaves from all the varieties. This will reveal whether there was any time lapse between the emplacements of the two separate intrusives. Moreover, mineral chemistry should be done on certain accessory minerals (e.g. apatite and monazite), as well as the alkali−feldspar megacrysts and biotite grains to test the true nature of lithochemical properties of the Batholith investigated. Lastly, it is suggested that oxygen isotopes be analysed from zircon grains; this will further constrain the sources of the magmas.

As for the Cape Columbine granites, the findings of this research seem to corroborate the findings of previous studies such as that of Scheepers (1995) and Frost and Frost (2011) on the petrogenesis of A−type (ferroan) granites. However, it is suggested that more samples be analysed for Nd isotopes. The isotopic data from this study suggests quite a large range in the T_{DM} model ages. This might simply be due to sample bias. Thus, more Sr and Nd analysis will yield a better statistical backing to constrain the sources.

References

Anderson, I. C., Frost, C. D., & Frost, B. R. (2003). Petrogenesis of the Red Mountain pluton, Laramie anorthosite complex, Wyoming: implications for the origin of A-type granites. In: Medaris, L. G. Jr, Byers, C. W., Mickelson, D. M. & Shanks, W. C. (Eds.). *Proterozoic geology: selected papers from an international symposium, Precambrian Research 124*, 243-267.

Barbarin, B. (1999). A review of the relationships between granitoid types, their origins and their geodynamic environments. *Lithos 46*, 605-626.

Barker, F., Wones, D. R., Sharp, W. N., & Desborough, G. A. (1975). The Pikes Peak Batholith, Colorado Front Range, and a model for the origin of the gabbro-anorthosite-syenite-potassic granite suite. *Precambrian Research 2*, 97-160.

Begemann, F., Ludwig, K. R., Lugmair, G. W., K., M., Nyquist, L. E., Patchett, P. J., Renne, P., Shih, C. Y., Villa, I. M., Walker, R. J. (2001). Call for an improved set of decay constants for geochronological use. *Geochimica et Cosmochimica Acta 65*, 111-121.

Belcher, R. W., & Kisters, A. F. (2003). Lithostratigraphic correlations in the western branch of the Pan-African Saldania Belt, South Africa: the Malmesbury Group revisited. *South African Journal of Geology 106*, 327-342.

Boynton, W. V. (1984). Geochemistry of the rare earth elements: meteorite studies. *Developments in Geochemistry 2*, 63-114.

Bowen, N.L., (1928). *The evolution of the igneous rocks*. Princeton University Press.

Buck, W. R., Martinez, F., Stecklear, M. S., & Cochran, J. R. (1988). Thermal consequences of lithospheric extension: pure and simple. *Tectonics 7 (2)*, 213-234.

Cai, K. D., Sun, M., Yuan, C., Zhao, G. C., Xiao, W. J., Long, X. P., Wu, F. Y. (2011). Prolonged magmatism, juvenile nature and tectonic evolution of the Chinese Altai, NW China: Evidence from zircon U–Pb and Hf isotopic study of Paleozoic granitoids. *Journal of Asian Earth Sciences 42*, 949-968.

Chappell, B. W., & White, A. J. (1974). Two contrasting granite types. *Pacific Geology 8(2)*, 173-174.

Chappell, B. W., & White, A. J. (1984). I- and S-type granites in the Lachlan Fold Belt, southeastern Australia. In X. Keqin, & Z. Guangchi (Eds.), *Geology of Granites and Their Metallo- genic Relations* (pp. 87-101). Beijing: Science Press.

Chemale, F., Scheepers, R., Gresse, P. G., & Van Schmus, W. R. (2011). Geochronology and sources of late Neoproterozoic to Cambrian granites of the Saldania Belt. *International Journal of Earth Sciences 100*, 431-444.

Clemens, J. D. (2012). Granitic magmatism, from source to emplacement: a personal view. *Applied Earth Science 121 (3)*, 107-136.

Clemens, J. D., & Mawer, C. K. (1992). Granitic magma transport by fracture propagation. *Tectonophysics 204* , 339-360.

Clemens, J. D., & Stevens, G. (2012). What controls chemical variation in granitic magmas? *Lithos 134–135*, 317-329.

Clemens, J. D., & Wall, V. J. (1981). Origin and crystallization of some peraluminous (S-type) granitic magmas. *Canadian Mineralogist 9*, 111-131.

Clemens, J. D., Darbyshire, D. P., & Flinders, J. (2009). Sources of post-orogenic calc-alkaline magmas: the Arrochar and Garabal Hill–Glen Fyne complexes, Scotland. *Lithos 112 (3–4)*, 524-542.

Clemens, J. D., Stevens, G., & Farina, F. (2011). The enigmatic sources of I-type granites: The peritectic connexion. *Lithos 126 (3-4)*, 174-181.

Clemens, J. D., Regmi, K., Nicholls, I. A., Weinberg, R., & Maas, R. (2016). The Tynong pluton, its mafic synplutonic sheets, and igneous microgranular enclaves: the nature of the mantle connection in I-type granitic magmas. *Contributions to mineralogy and petrology 171:35*.

Clemens, J. D., Buick, I. S., Frei, D., Lana, C., & Villaros, A. (2017a). Post-orogenic shoshonitic magmas of the Yzerfontein pluton, South Africa: the 'smoking gun' of mantle melting and crustal growth during Cape granite genesis? *Contributions to mineralogy and petrology 172:72*.

Clemens, J. D., Elburg, M. A., & Harris, C. (2017b). Origins of igneous microgranular enclaves in granites: the example of Central Victoria, Australia. *Contributions to Mineralogy and Petrology 172:88*.

Clemens, J. D., Stevens, G., & Elburg, M. A. (2017c). Petrogenetic processes in granitic magmas and their igneous microgranular enclaves from Central Victoria, Australia: match or mismatch?. *Transactions of the Royal Society of South Africa 72 (1)*, 6-32.

Clemens, J. D., Stevens, G., Frei, D., & Josephs, C. S. (2017d). Origins of cryptic variation in the Ediacaran–Fortunian rhyolitic ignimbrites of the Saldanha Bay Volcanic Complex, Western Cape, South Africa. *Contributions to petrology and mineralogy 172:99*.

Collins, W. J., Beams, D., White, J. R., & Chappell, B. (1982). Nature and origin of A-type granites with particular reference to south-eastern Australia. *Contributions to Mineralogy and Petrology 80*, 189-200.

Creaser, R. A., Price, R. C., & Wormald, R. J. (1991). A-type granites revisited: assessment of a residual-source model. *Geology 19*, 163-166.

Da Silva, L. C., Gresse, P. G., Scheepers, R., McNaughton, N. J., Hartmann, L. A., & Fletcher, I. (2000). U-Pb SHRIMP and Sm-Nd age constraints on the timing and sources of the Pan-African Cape Granite Suite, South Africa. *Journal of African Sciences 30*, 795-815.

DePaolo, D. (1981). A neodymium and strontium isotopic study of the Mesozoic calc-alkaline granitic batholiths of Sierra Nevada and Peninsular Ranges, California. *Journal Geophysical Research 68*, 470-488.

Eby, G. N. (1990). The A-type granitoids: A review of their occurrence and chemical characteristics and speculations on their petrogenesis. *Lithos 26*, 115-134.

Eby, G. N. (1992). Chemical subdivision of the A-type granitoids: Petrogenetic and tectonic implications. *Geology 20*, 641-644.

Farina, F., Stevens, G., Dini, A., & Rocchi, S. (2012). Peritectic phase entrainment and magma mixing in the late Miocene Elba Island laccolith–pluton–dyke complex (Italy). *Lithos 153*, 243-260.

Finger, F., & Schiller, D. (2012). Lead contents of S-type granites and their petrogenetic significance. *Contributions to mineralogy and petrology 164*, 747-755.

Frimmel, H. E., Basei, M. S., & Gaucher, C. (2011). Neoproterozoic geodynamic evolution of SW-Gondwana: a southern African perspective. *International Journal of Earth Sciences 100*, 323-354.

Frimmel, H. E., Miguel, A. S., Vinicius, X. C., & Ndawedapo, M. (2013). A new lithostratigraphic subdivision and geodynamic model for the Pan-African western Saldania Belt, South Africa. *Precambrian Research 231*, 218-235.

Frost, B. R., & Frost, C. D. (2008). A geochemical classification for feldspathic igneous rocks. *Journal of Petrology 49*, 1955-1969.

Frost, B. R., Barnes, C. G., Collins, W. J., Arculus, R. J., Ellis, D. J., & Frost, C. D. (2001). A geochemical classification for granitic rocks. *Journal of Petrology 42 (11)*, 2033-2048.

Frost, C. D., & Frost, B. R. (2011). On ferroan (A-type) granitoids: their compositional variability and modes of origin. *Journal of Petrology 52 (1)*, 39-53.

Frost, C. D., & Frost, B. R. (1997). Reduced rapakivi-type granites: the tholeiite connection. *Geology 25*, 647-650.

Gao, P., Zheng, Y.-F., & Zhao, Z.-F. (2016). Experimental melts from crustal rocks: A lithochemical constraint on granite petrogenesis. *Lithos 266-267*, 133-157.

Garcia-Arias, M., & Stevens, G. (2017). Phase equilibrium modeling of granite magma petrogenesis: A. An evaluation of the magma compositions produced by crystal entrainment in the source. *Lithos 277*, 131-153.

Glazner, A. F. (2007). Thermal limitations on incorporation of wall rock into magma. *Geology 35 (4)*, 319-322.

Grebennikov, A. V. (2014). Erratum to "A type granites and related rocks: petrogenesis and classification. *Russian Geology and Geophysics 55*, 1354-1366.

Gresse, P. G., Von Veh, M. W., & Frimmel, H. E. (2006). Namibian (Neoproterozoic) to early Cambrian successions. In M. R. Johnson, C. R. Anhaeusser, & R. J. Thomas, *The Geology of South Africa* (pp. 395-420). Johannesburg: Geological Society of South Africa.

Haapala, I., & Rämö, O. T. (1990). Petrogenesis of the Proterozoic rapakivi granites of Finland. In: Stein, H. J. & Hannah, J. L. (Eds.) Ore-bearing granite systems; petrogenesis and mineralizing processes. *Geological Society of America, Special Papers 246*, 275-286.

Han, Y., Wang, Y., Guochun, Z., & Qingyan, C. (2014). Syn-tectonic emplacement of the Late Mesozoic Laojunshan granite pluton in the eastern Qinling, central China: An integrated fabric and geochronologic study. *Journal of Structural Geology 68*, 1-15.

Hartnady, C. J., Newton, A. R., & Theron, J. N. (1974). The stratigraphy and structure of the Malmesbury Group in the southwestern Cape. *Bulletin of the Precambrian Research Unit, University of Cape Town, South Africa 15*, 193-213.

Hill, M., Barker, F., Hunter, D., & Knight, R. (1996). Geochemical characteristics and origin of the Lebowa Granite Suite, Bushveld Complex. *International Geology Review 38*, 195-227.

Janoušek, V., Farrow, C. M., & Erban, V. (2006). Interpretation of Whole-rock Geochemical Data in Igneous Geochemistry: Introducing Geochemical Data Toolkit (GCDkit). *Journal of Petrology 47 (6)*, 1255-1259.

Kisters, A. F., Belcher, R. W., Scheepers, R., Rozendaal, A., Jordaan, L. S., & Armstrong, R. A. (2002). Timing and kinematics of the Colenso Fault: The Early Paleozoic shift from collisional to extensional tectonics in the Pan-African Saldania Belt, South Africa. *South African Journal of Geology 105*, 257-270.

Loiselle, M. C., & Wones, D. R. (1979). Characteristics and origin of anorogenic granites. *Abstracts of Papers to Be Presented at the Annual Meetings of the Geological Society of America and Associated Societies 11*, (p. 468). San Diego, California.

Metcalfe, R. V., Smith, E. I., Walker, J. D., Reed, R. C., & Gonzales, D. A. (1995). Isotopic disequilibrium among commingled hybrid magmas: evidence for two-stage magma mixing – commingling processes in the Mt Perkins pluton, Arizona. *Journal of Geology 103*, 509-527.

Middlemost, E. A. (1994). Naming materials in magma/igneous rock system. *Earth Science Reviews 37*, 215-224.

Míková, J., & Denková, P. (2007). Modified chromatographic separation scheme for Sr and Nd isotope analysis in geological silicate samples. *Journal of Geosciences 52*, 221-226.

Moreno, J. A., Molina, J. F., Montero, P., Abu Anbar, M., Scarrow, J. H., Cambeses, A., Bea, F. (2014). Unraveling sources of A-type magmas in juvenile continental crust: Constraints from compositionally diverse Ediacaran post-collisional granitoids in the Katerina Ring Complex, southern Sinai, Egypt. *Lithos 192-195*, 56-85.

Moyen, J. F., Laurent, O., Chelle-Michou, C., Couzinié, S., Vanderhaeghe, O., Zeh, A., Villaros, A., Gardien, V. (2016). Collision vs. subduction-related magmatism: Two contrasting ways of granite formation and implications for crustal growth. *Lithos 277*, 154-177.

Naumov, V. B., Kovalenko, V. I., Dorofeeva, V. A., Girnis, A. V., & Yarmolyuk, V. V. (2010). Average compositions of igneous melts from main geodynamic settings according to the investigation of melt inclusions in minerals and quenched glasses of rocks. *Geochemistry International 48 (12)*, 1185-1207.

Osborn, E. F. (1956). Role of oxygen pressure in the crystallization and differentiation of basaltic magma. *American Journal of Science 257*, 609-647.

Patiňo Douce, A. (1997). Generation of metaluminous A-type granites by low-pressure melting of calc-alkaline granitoids. *Geology 25*, 743-746.

Pearce, J. A., Harris, N. B., & Tindle, A. G. (1984). Trace element discrimination diagrams for tectonic interpretation of granitic rocks. *Journal of Petrology 25*, 956-983.

Peng, G., Zhao, Z.-F., & Zheng, Y.-F. (2014). Petrogenesis of Triassic granites from the Nanling Range in South China: Implications for geochemical diversity in granites. *Lithos 210-211*, 40-56.

Pin, C., & Zalduegui, J. F. (1997). Sequential separation of light rare-earth elements, thorium and uranium by miniaturized extraction chromatography: application to isotopic analyses of silicate rocks. *Analytica Chimica Acta 339*, 79-89.

Pin, C., Briot, D., Bassin, C., & Poitrasson, F. (1994). Concomitant separation of strontium and samarium–neodymium for isotopic analysis in silicate samples, based on specific extraction chromatography. *Analytica Chimica Acta 298*, 209-217.

Roberts, M. P., & Clemens, J. D. (1993). Origin of high-potassium, calc-alkaline, I-type granitoids. *Geology 21*, 825-828.

Rollinson, H. (1993). *Using geochemical data: evaluation, presentation, interpretation.* Edinburgh: Edinburgh Gate.

Rowe, C. D., Backeberg, N. R., Van Rensburg, T., MacLennan, S. A., Faber, C., Curtis, C., Vigiletti, P. A. (2010). Structural geology of Robben Island: implications for the tectonic environment of Saldanian deformation. *South African Journal of Geology 113*, 57-72.

Rozendaal, A., Gresse, P. G., Scheepers, R., & Le Roux, J. P. (1999). Neoproterozoic to Early Cambrian crustal evolution of the Pan-African Saldania Belt, South Africa. *Precambrian Research 97*, 303-323.

Scheepers, R. (1995). Geology, geochemistry, and petrogenesis of Late Precambrian S-, I- and A-type granitoids in the Saldania belt, Western Cape Province, South Africa. *Journal of African Earth Sciences 21*, 35-58.

Scheepers, R., & Armstrong, R. A. (2002). New U-Pb SHRIMP zircon ages of the Cape Granite Suite: implications for the magmatic evolution of the Saldania Belt. *South African Journal of Geology 105*, 241-256.

Scheepers, R., & Poujol, M. (2002). U-Pb zircon age of Cape Granite Suite ignimbrites: characteristics of the last phases of the Saldanian magmatism. *South African Journal of Geology 105*, 163-178.

Siegfried, H. P. (1981). Die Vredenburg Adamelliet. *Annals of the University of Stellenbosch, series (A1), 3* , 279-347.

Skjerlie, K. P., & Johnston, A. D. (1993). Fluid-absent melting behavior of an F-rich tonalitic gneiss at mid-crustal pressures: Implications for the generation of anorogenic granites. *Journal of Petrology 34*, 785-815.

Steiger, R. H., & Jäger, E. (1977). Subcommission on geochronology: Convention on use of decay constants in geo- and cosmochronology. *Earth and Planetary Science Letters 126*, 359-362.

Stevens, G., Villaros, A., & Moyen, J. (2007). Selective peritectic garnet entrainment as the origin of geochemical diversity in S-type granites. *Geology 35 (1)*, 9-12.

Streckeisen, A. (1976). To each plutonic rock its proper name. *Earth Science Reviews 12*, 1-33.

Sun, F., Xisheng, X., Haibo, Z., & Yan, X. (2015). Petrogenesis and magmatic evolution of ~130 Ma A-type granites in Southeast China. *Journal of Asian Earth Sciences 98*, 209-224.

Sun, S. S., & McDonough, W. F. (1989). Chemical and isotopic systematics of oceanic basalts, implications for mantle composition and processes. *Geological Society of London, Special Publications 42 (1)*, 313-345.

Tanaka, H., Togashi, S., Kamioka, H., Amakawa, H., Kagami, H., Hamamoto, T., Yuhara, M., Orihashi, Y., Yoneda, S., Shimizu, H., Kunimaru, T., Takahashii, K., Yanagi, T., Nakano, T., Fujimaki, H., Shinjo, R., Asahara, Y., Tanimizu, M., Dragusanu, C. (2000). JNdi−1: a neodymium isotopic reference inconsistency with Lajolla neodymium. *Chemical Geology 168*, 279-281.

Theron, J. N., Gresse, P. G., Siegfried, H. P., & Rogers, J. (1992). The Geology of the Cape Town Area. *Explantation of Sheet 3318. Geological Survey of South Africa*, 140pp.

Verma, S. P. (2012). Application of multi-dimensional discrimination diagrams and probability calculations to acid rocks from Portugal and Spain. *Comunicações Geológicas 99*, 79-93.

Verma, S. P. (2010). Statistical evaluation of bivariate, ternary and discriminant function tectonomagmatic discrimination diagrams. *Turkish Journal of Earth Sciences 19*, 185-238.

Verma, S. P., Pandarinath, K., Verma, S. K., & Agrawal, S. (2013). Fifteen new discriminant-function-based multi-dimensional robust diagrams for acid rocks and their application to Precambrian rocks. *Lithos 168-169*, 113-123.

Villaros, A. (2010). Petrogenesis of S-type Granite with Particular Emphasis on Source Processes: The Example of the S-type Granite of the Cape Granite Suite. Ph.D. Thesis. Stellenbosch University. Stellenbosch, South Africa.

Villaros, A., Stevens, G., & Buick, I. S. (2009a). Tracking S-type granite from source to emplacement: Clues from garnet in the Cape Granite Suite. *Lithos 112 (3-4)* , 217-235.

Villaros, A., Stevens, G., Moyen, J., & Buick, I. (2009b). The trace element compositions of S-type granites: evidence for disequilibrium melting and accessory phase entrainment in the source. *Contributions to mineralogy and petrology 158*, 543-561.

Wall, V. J., Clemens, J. D., & Clarke, D. (1987). Models for granitoid evolution and source compositions. *Journal of Geology 95*, 731-749.

Weis, D., Kieffer, B., Maerschalk, C., Barling, J., de Jong, J., Williams, G. A., Hanano, D., Pretorius, W., Mattielli, N., Scoates, J. S., Goolaerts, A., Friedman, R. M., Mahoney, G. B. (2006). High-precision isotopic characterization of USGS reference materials by TIMS and MC-ICP- MS. *Geochemistry, Geophysics, Geosystems 7 (8)*.

Whalen, J. B., Currie, K., & Chappell, B. (1987). A-type granites: geochemical characteristics, discrimination, and petrogenesis. *Contributions to Mineralogy and Petrology 95*, 407-419.

White, A. J., & Chappel, B. W. (1977). Ultrametamorphism and granitoid genesis. *Tectonophysics 43*, 7-22.

White, A. R., & Chappell, B. W. (1988). Some supracrustal (S-type) granites of the Lachlan Fold Belts. *Transactions of the Royal Society of Edinburgh, Earth Sciences 79*, 169-181.

Winter, J. D. (2001). *An Introduction to Igneous and Metamorphic Petrology.* New Jersey, USA: Prentice-Hall Inc.

Zarrebini, S. K. (2016). An experimental investigation into the 'fate' of entrained peritectic minerals in I-type granite magmas intruded at below 2kbar. Unpublished MSc. Thesis. Stellenbosch University, Stellenbosch, South Africa.

Zhou, G., Wu, Y., Wang, H., Qin, Z., Zhang, W., Zheng, J., Yang, S. (2017). Petrogenesis of the Huashanguan A-type granite complex and its implications for the early evolution of the Yangtze Block. *Precambrian Research 292*, 57-74.

Appendix list

Appendix A	Google Earth™ images with sample locations
Appendix B	Table which present the geographic locations of each sample collected and what they were analysed for.
Appendix C	Photographs of outcrop that were not in the thesis.
Appendix D	Standards used for X−ray fluorescence (XRF) and Laser-Ablation Inductively Coupled Plasma Mass Spectrometry (LA-ICPMS) geochemical analysis
Appendix E	Harker Plots for the Vredenburg Batholith granites and enclaves
Appendix F	Calculated values for the discriminant functions for the tectonomagmatic diagrams using TecDia software (after Verma et al., 2013).

Appendix A: Google Earth™ images with sample locations.

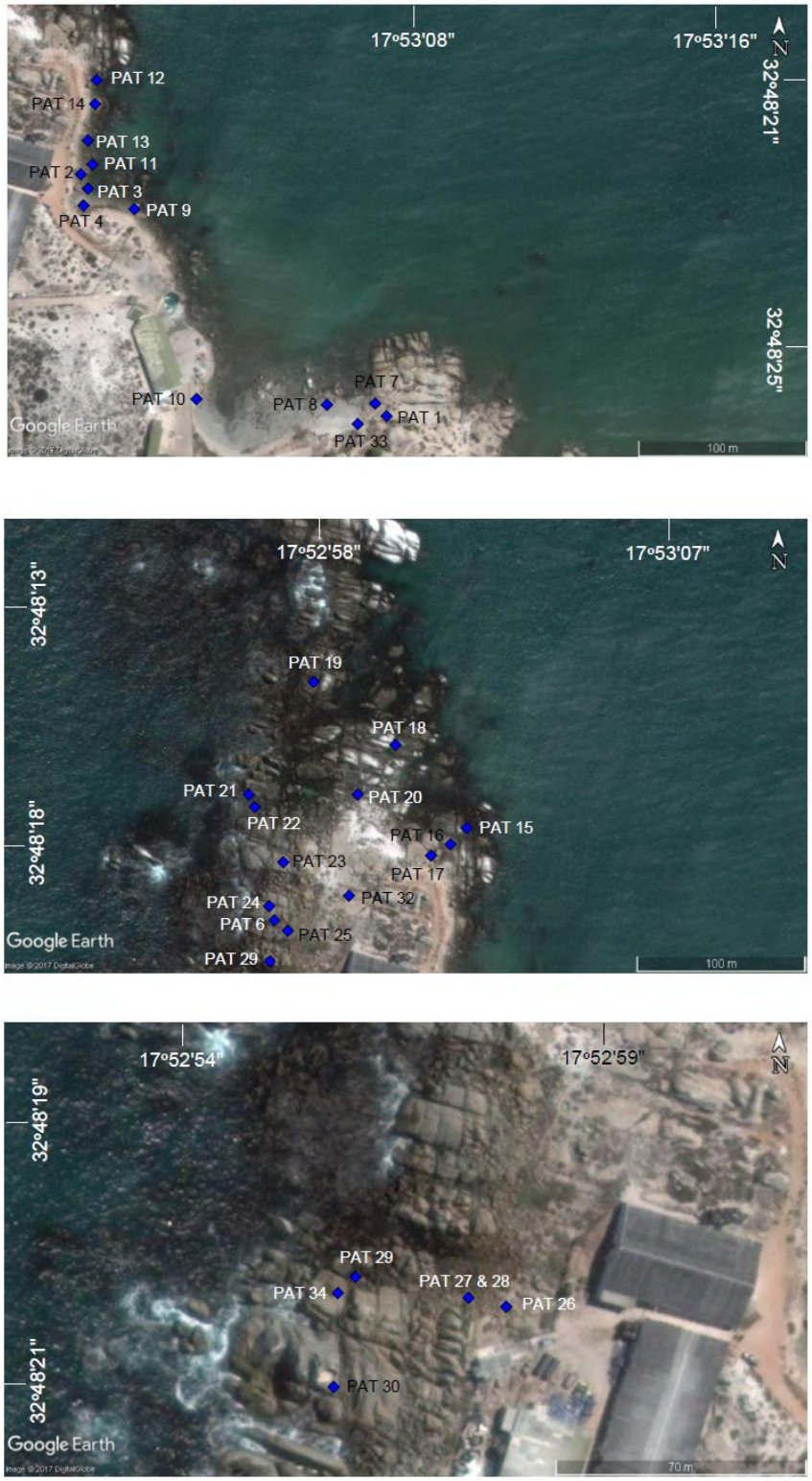

Figure A1: Sample locations collected around the fisheries of Paternoster. Top) Samples locations to the east of the fisheries. Middle) Sample locations to the north of the fisheries. Bottom) Samples collected to the west of the fisheries. All directions are reported with reference to the North arrow direction in the images.

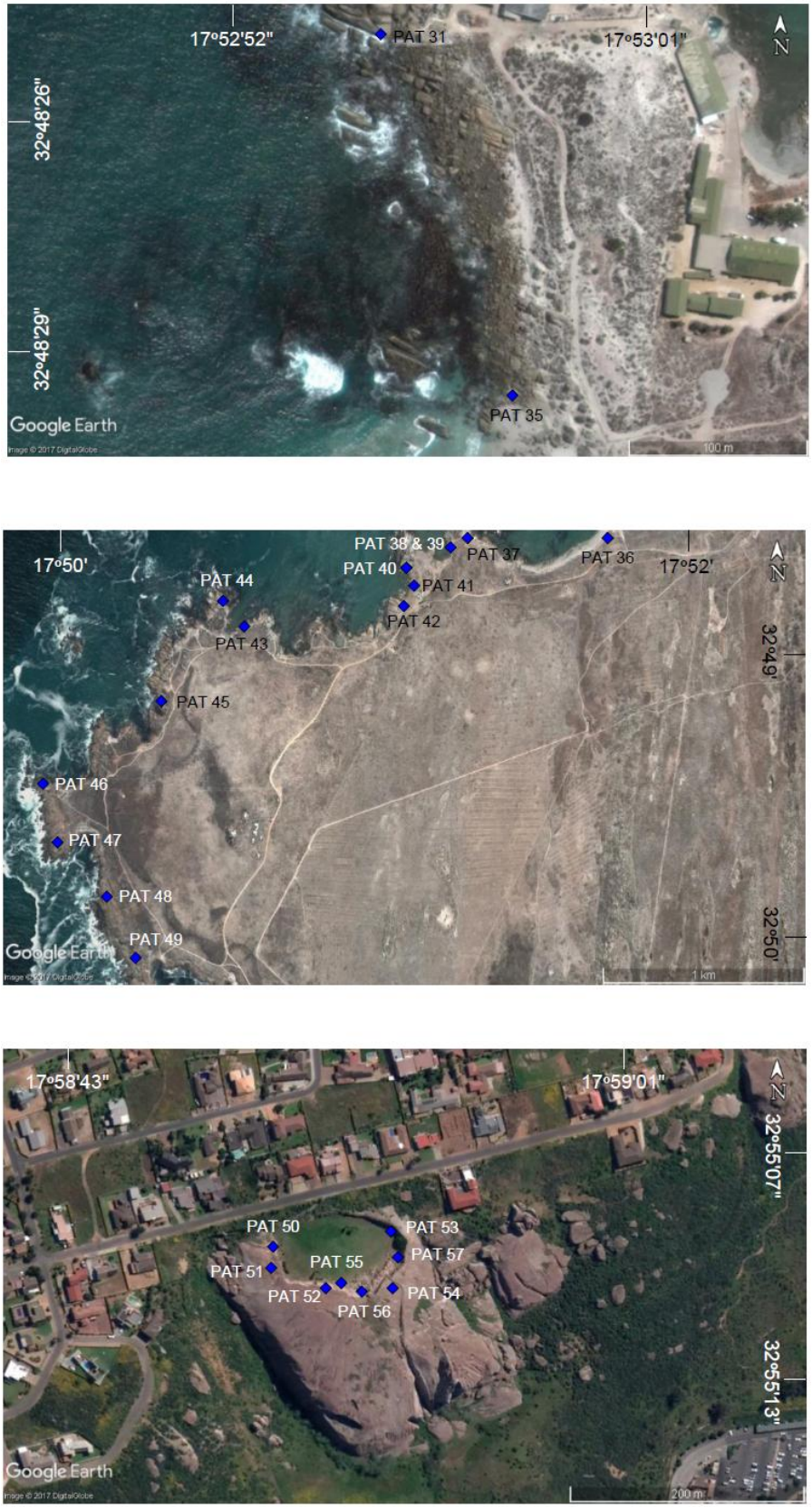

Figure A2: Sample locations along the west coast and in Vredenburg. Top: Two sample localities to the Southwest of the fisheries in Paternoster. Middle) Sample localities from the Cape Columbine Nature Reserve. Bottom) image of the sample locations in the residential area of Vredenburg.

Appendix B: Sample coordinates.

Sample ID	Comment	Pluton/Batholith	Southing	Easting	Analysed for
PAT 1	Sheared granite	Vredenburg batholith	32°48'25.76"	17°53'08.26"	
PAT 2	Granite	Vredenburg batholith	32°48'21.15"	17°53'01.15"	Geochemistry
PAT 3	Granite	Vredenburg batholith	32°48'21.52"	17°53'01.44"	
PAT 4	Igneous enclave	Vredenburg batholith	32°48'21.89"	17°53'01.31"	Geochemistry
PAT 6	Igneous enclave	Vredenburg batholith	32°48'19.57"	17°52'57.25"	Petrography and geochemistry
PAT 7	Igneous enclave	Vredenburg batholith	32°48'25.14"	17°53'08.00"	Petrography and geochemistry
PAT 8	Sheared granite	Vredenburg batholith	32°48'25.54"	17°53'06.94"	
PAT 9	Igneous enclave	Vredenburg batholith	32°48'21.83"	17°53'02.59"	
PAT 10	Granite	Vredenburg batholith	32°48'25.16"	17°53'04.23"	Geochemistry
PAT 11	Granite	Vredenburg batholith	32°48'21.08"	17°53'01.43"	Geochemistry
PAT 12	Sheared granite	Vredenburg batholith	32°48'19.25"	17°53'01.62"	
PAT 13	Igneous enclave	Vredenburg batholith	32°48'20.53"	17°53'01.40"	Petrography and geochemistry
PAT 14	Granite	Vredenburg batholith	32°48'19.87"	17°53'01.67"	Petrography and geochemistry
PAT 15	Igneous enclave	Vredenburg batholith	32°48'17.93"	17°53'01.69"	Petrography and geochemistry
PAT 16	Granite	Vredenburg batholith	32°48'18.31"	17°53'01.47"	
PAT 17	Granite	Vredenburg batholith	32°48'18.70"	17°53'00.97"	Geochemistry
PAT 19	Granite	Vredenburg batholith	32°48'15.22"	17°52'58.25"	Geochemistry
PAT 20	Sheared granite	Vredenburg batholith	32°48'17.26"	17°52'59.25"	
PAT 21	Granite	Vredenburg batholith	32°48'17.30"	17°52'56.84"	Geochemistry
PAT 22	Granite	Vredenburg batholith	32°48'17.70"	17°52'57.13"	Petrography and geochemistry
PAT 23	Sheared granite	Vredenburg batholith	32°48'18.74"	17°52'57.59"	Petrography
PAT 24	Igneous enclave	Vredenburg batholith	32°48'19.33"	17°52'57.22"	Geochemistry
PAT 25	Igneous enclave	Vredenburg batholith	32°20'21.02"	17°52'57.64"	Geochemistry
PAT 26	Granite	Vredenburg batholith	32°48'21.32"	17°52'58.00"	
PAT 26A	Igneous enclave	Vredenburg batholith	32°48'21.32"	17°52'58.00"	
PAT 27	Sheared granite	Vredenburg batholith	32°48'21.13"	17°52'57.50"	Petrography and geochemistry
PAT 28	Igneous enclave	Vredenburg batholith	32°48'21.13"	17°52'57.50"	Geochemistry
PAT 29	Granite	Vredenburg batholith	32°48'21.02"	17°52'56.31"	Petrography and geochemistry
PAT 30	Igneous enclave	Vredenburg batholith	32°48'22.06"	17°52'36.06"	Petrography and geochemistry
PAT 31	Granite	Vredenburg batholith	32°48'23.63"	17°52'58.25"	
PAT 32	Granite	Vredenburg batholith	32°48'19.34"	17°52'59.16"	
PAT 33	Granite	Vredenburg batholith	32°48'23.86"	17°53'07.63"	Petrography and geochemistry
PAT 34	Alkali feldspar granite	Vredenburg batholith	32°48'21.24"	17°52'56.09"	Petrography and geochemistry
PAT 35	Igneous enclave	Vredenburg batholith	32°48'30.46"	17°52'58.72"	Petrography and geochemistry
PAT 36	Granite	Vredenburg batholith	32°48'48.68"	17°52'31.55"	Petrography and geochemistry
PAT 37	Granite	Vredenburg batholith	32°48'49.34"	17°52'05.72"	Petrography and geochemistry
PAT 38	Alkali feldspar granite	Vredenburg batholith	32°48'51.87"	17°52'01.31"	Petrography and geochemistry
PAT 39	Granite	Vredenburg batholith	32°48'51.87"	17°52'01.31"	Geochemistry
PAT 40	Granite	Vredenburg batholith	32°48'55.44"	17°51'52.87"	
PAT 41	Granite	Vredenburg batholith	32°48'58.22"	17°51'54.36"	Petrography and geochemistry
PAT 42	Aplite vein	Vredenburg batholith	32°49'01.59"	17°51'52.32"	Petrography
PAT 43	Granite	Vredenburg batholith	32°49'06.17"	17°51'22.09"	Petrography and geochemistry

Sample ID	Comment	Pluton/Batholith	Southing	Easting	Analysed for
PAT 44	Mafic dyke	Vredenburg batholith	32°49'02.53"	17°51'17.63"	Petrography
PAT 18	Alkali feldspar granite	Cape Columbine Granites	32°48'16.43"	17°53'00.06"	Geochemistry
PAT 45	Alkali feldspar granite	Cape Columbine Granites	32°49'17.21"	17°51'05.77"	Petrography and geochemistry
PAT 46	Alkali feldspar granite	Cape Columbine Granites	32°49'31.90"	17°50'42.14"	Petrography and geochemistry
PAT 47	Alkali feldspar granite	Cape Columbine Granites	32°49'41.38"	17°50'44.87"	Petrography and geochemistry
PAT 48	Alkali feldspar granite	Cape Columbine Granites	32°49'48.61"	17°50'54.91"	Petrography and geochemistry
PAT 49	Alkali feldspar granite	Cape Columbine Granites	32°50'01.23"	17°51'01.26"	Petrography and geochemistry
PAT 50	Igneous enclave	Vredenburg batholith	32°55'09.59"	17°58'49.78"	Petrography and geochemistry
PAT 51	Granite	Vredenburg batholith	32°55'10.15"	17°58'49.80"	Geochemistry
PAT 52	Granite	Vredenburg batholith	32°55'10.58"	17°58'51.61"	Geochemistry
PAT 53	Granite	Vredenburg batholith	32°55'09.09"	17°58'53.32"	
PAT 54	Igneous enclave	Vredenburg batholith	32°55'10.60"	17°58'53.09"	Petrography and geochemistry
PAT 55A	Igneous enclave	Vredenburg batholith	32°55'10.53"	17°58'51.65"	Geochemistry
PAT 55B	Igneous enclave	Vredenburg batholith	32°55'10.53"	17°58'51.65"	
PAT 56	Granite	Vredenburg batholith	32°55'10.78"	17°58'52.36"	Petrography and geochemistry
PAT 57	Granite	Vredenburg batholith	32°55'09.82"	17°58'53.72"	

Appendix C: Field photos of the Vredenburg Batholith.

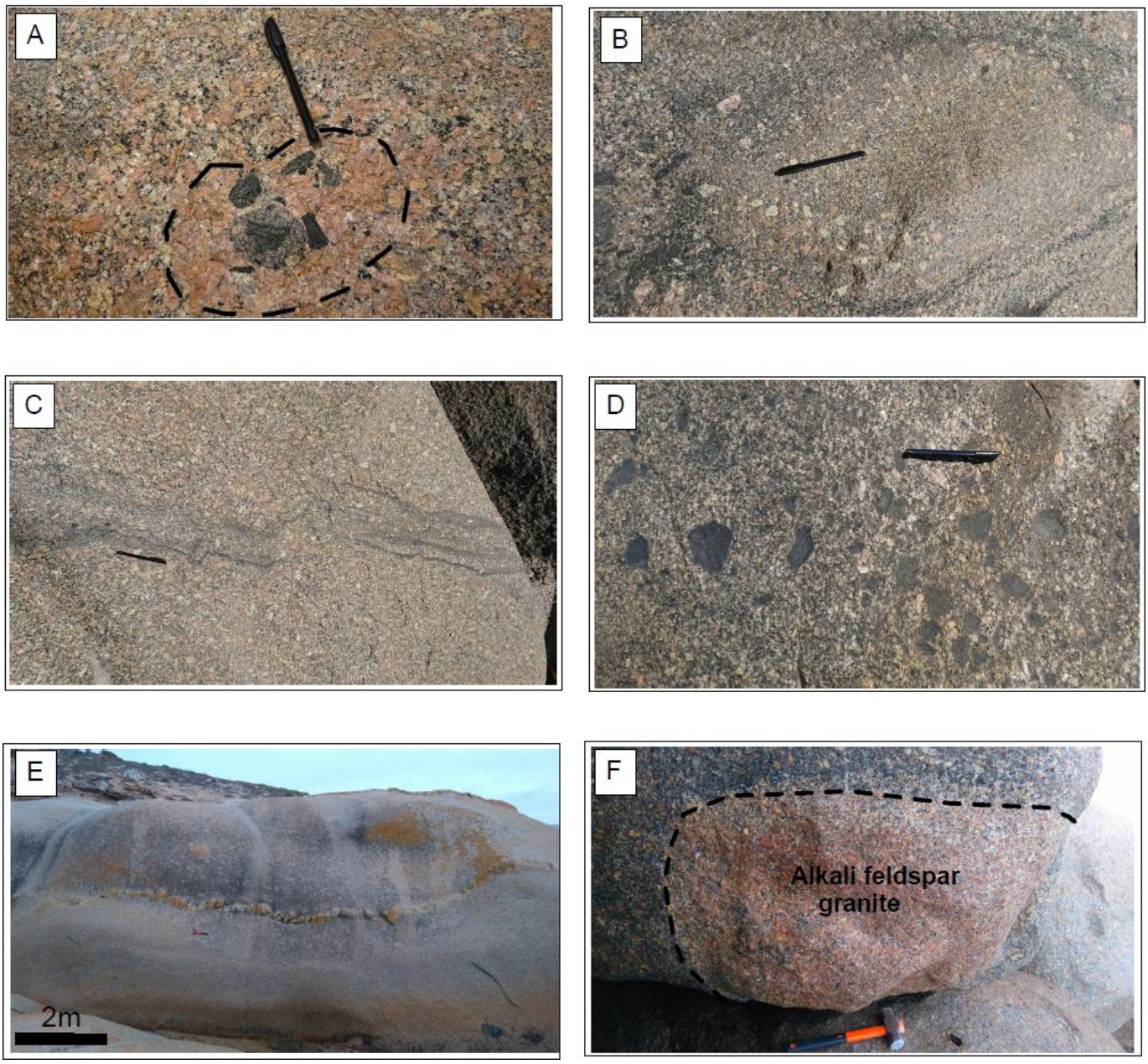

Figure C1: Selected field photographs of the Vredenburg Batholith outcrop. A) Pegmatoidal clot B) Mafic mineral layering wrapping around an enclave. C) Mafic mineral layering with a kink in the layer. D) Xenolith clots in a more mafic portion of the granites. E) Aplite vein cross–cutting the granites. F) An alkali feldspar granite. Scale: Hammer = 32cm and pen = 12cm.

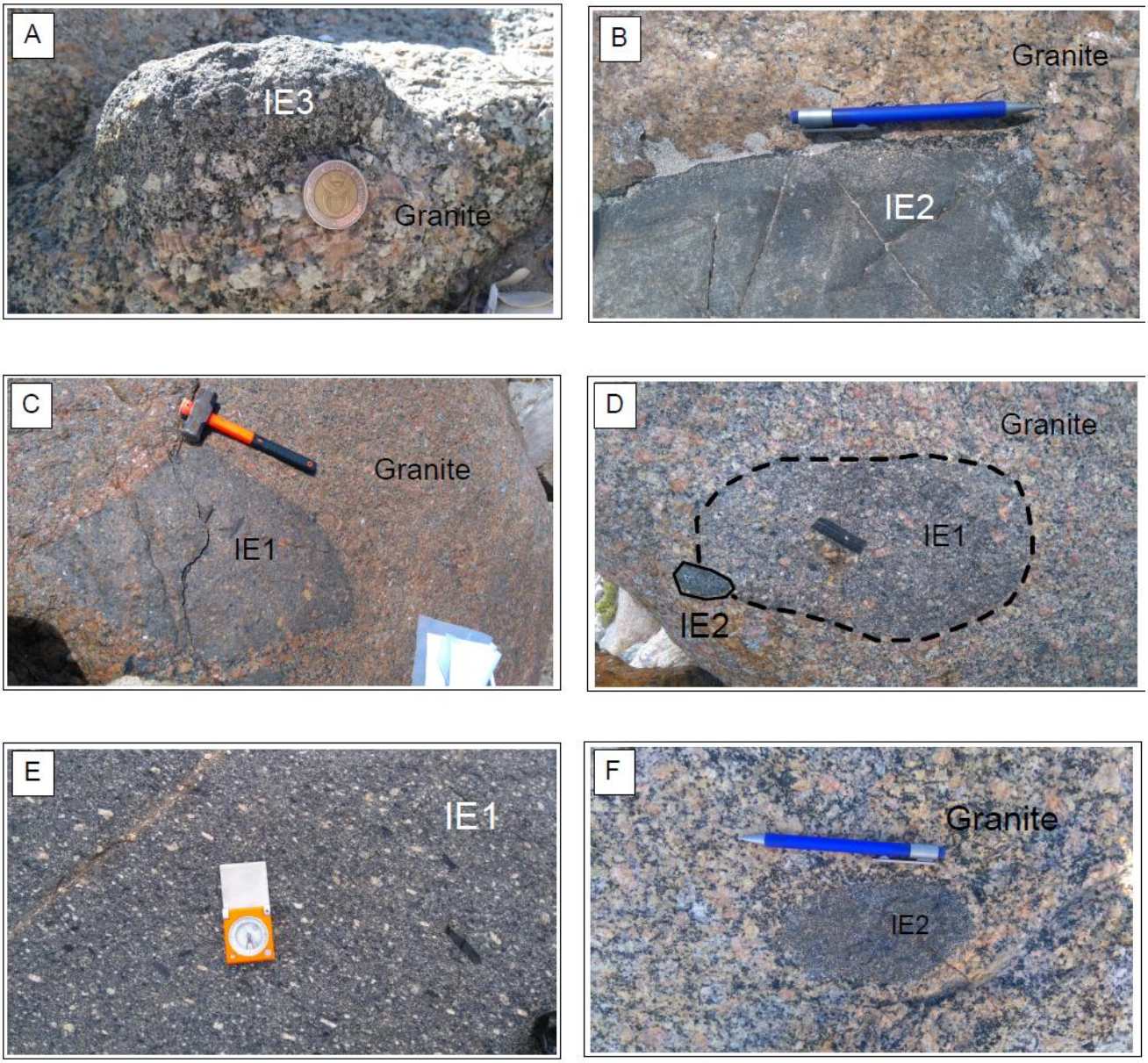

Figure C2: A) Intermediate enclave. B) Medium− grained mafic enclave with a biotite clot to the top right of the enclave. C) Rhombic shaped enclave of IE1 D) Porphyritic enclave of IE1 with a medium-grained mafic enclave (IE2). E) Porphyritic enclave with aligned Alkali feldspar megacrysts. F) Oval shaped medium−grained mafic enclave with a clot of mafic minerals to the top left of the enclave.

Appendix D: Standards used for X-ray fluorescence (XRF) and Laser-Ablation Inductively Coupled Plasma Mass Spectrometry (LA-ICPMS)

Table D1: Standards used for XRF

NIM-G		Meas. date/time	Al2O3	CaO	Cr2O3	Fe2O3	K2O	MgO	MnO	Na2O	P2O5	SiO2	TiO2	L.O.I.	Sum Of Conc.
Granite Reference values			**12,08**	**0,78**	**0,0012**	**2,02**	**4,99**	**0,06**	**0,02**	**3,36**	**0,01**	**75,7**	**0,09**		**99,1112**
NIM-G STD	Majors Acid32	2015-07-27 10:17	12,26	0,82	0	1,99	5,01	0,08	0,02	3,41	0,01	75,76	0,1		99,46
NIM-G STD	Majors Acid32	2015-07-27 17:44	12,2	0,82	0	1,99	5,01	0,07	0,02	3,37	0,01	75,85	0,09		99,44
NIM-G STD	Majors Acid32	2015-07-28 12:03	12,25	0,81	0	1,98	5,01	0,07	0,02	3,38	0,01	75,7	0,1		99,33
STANDARD Nim-G	Majors Acid32	2015-09-01 10:52	12,26	0,8	0	1,98	4,98	0,08	0,02	3,37	0,01	75,43	0,1		99,03
NIM-G std	Majors Acid32	2015-10-01 11:24	12,3	0,81	0	1,99	5,01	0,07	0,02	3,35	0,01	76,31	0,09		99,96
NIM-G std	Majors Acid32	2015-10-06 12:52	12,27	0,81	0	1,98	5,01	0,07	0,02	3,34	0,01	75,97	0,09		99,57
NIM-G STD	Majors Acid32	2015-10-29 11:53	12,18	0,81	0	1,98	4,98	0,07	0,02	3,36	0,01	76,02	0,1		99,53
NIM-G STD	Majors Acid32	2016-01-14 16:29	12,14	0,81	0	1,98	4,99	0,07	0,02	3,34	0,02	75,74	0,1		99,27
NIM-G std	Majors Acid32	2016-02-04 20:53	12,16	0,8	0	1,99	5,02	0,07	0,02	3,39	0,01	75,77	0,1		99,33
NIM-G STD	Majors Acid32	2016-02-11 17:56	12,17	0,81	0	1,99	5	0,07	0,02	3,34	0,02	75,41	0,1		98,93
NIM-G std	Majors Acid32	2016-03-08 16:17	11,94	0,82	0	1,99	4,97	0,07	0,02	3,22	0,01	75,43	0,09		98,56
NIM-G std	Majors Acid32	2016-03-14 23:05	12	0,81	0	1,98	4,96	0,07	0,02	3,21	0,01	75,5	0,08		98,63
NIM-G STD	Majors Acid32	2016-03-18 23:30	11,93	0,8	0	1,98	4,97	0,07	0,02	3,19	0,02	75,41	0,08		98,47
NIM-G STD	Majors Acid32	2016-04-12 23:31	12,03	0,81	0	1,99	4,97	0,07	0,02	3,22	0,02	75,17	0,08		98,36
NIM-G STD	Majors Acid32	2016-04-15 05:48	12,03	0,81	0	1,99	4,99	0,07	0,02	3,19	0,02	75,38	0,08		98,58
NIM-G std	Majors Acid32	2016-05-05 00:16	11,96	0,81	0	1,99	4,97	0,06	0,02	3,22	0,01	75,46	0,08		98,56
NIM-G STD	Majors Acid32	2016-06-07 00:28	12,01	0,81	0	1,99	4,97	0,07	0,02	3,22	0,02	75,23	0,08		98,42
NIM-G STD	Majors Acid32	2016-07-26 23:47	11,96	0,81	0	1,98	4,98	0,07	0,02	3,18	0,02	75,29	0,08		98,39
NIM-G std	Majors Acid32	2016-08-23 00:21	11,96	0,8	0	1,99	4,99	0,07	0,02	3,15	0,01	75,34	0,08		98,41
NIM-G std	Majors Acid32	2016-08-24 20:44	11,9	0,8	0	1,99	4,98	0,07	0,02	3,16	0,02	75,13	0,08		98,15
NIM-G std	Majors Acid32	2016-08-25 17:17	11,95	0,81	0	1,99	4,98	0,07	0,02	3,21	0,02	75,02	0,08		98,33
NIM-G std	Majors Acid32	2016-08-31 02:31	11,91	0,81	0	1,98	4,99	0,07	0,02	3,17	0,02	75,15	0,08		98,2
NIM-G STD	Majors Acid32	2016-09-01 04:00	11,88	0,81	0	1,98	4,98	0,07	0,02	3,17	0,02	75,44	0,09		98,46
NIM-G STD	Majors Acid32	2016-09-07 16:37	11,95	0,81	0	1,99	4,97	0,07	0,02	3,19	0,02	75,39	0,08		98,49
Average			12,07	0,81	0,00	1,99	4,99	0,07	0,02	3,27	0,02	75,52	0,09		98,83
Relative standard deviation (%)			0,1 1	3,74	100,00	1,69	0,06	17,36	0,00	2,83	54,17	0,24	2,31		0,29
JG-1															
Granodiorite Reference values			**14,20**	**2,18**	**0,01**	**2,14**	**3,97**	**0,74**	**0,06**	**3,39**	**0,10**	**72,30**	**0,26**		**99,35**
JG-1 STD	Majors Interm32	2014-12-10 14:42	14,14	2,17	0,01	2,12	4,01	0,73	0,07	3,35	0,10	72,95	0,25		99,90
STANDARD JG-1	Majors Acid32	2015-09-01 12:44	14,34	2,19	0,01	2,12	4,02	0,78	0,07	3,60	0,10	72,13	0,27		99,63
JG-1 std	Majors Acid32	2015-10-01 11:33	14,44	2,20	0,01	2,14	4,03	0,77	0,07	3,63	0,10	72,80	0,26		100,45
JG-1 std	Majors Acid32	2015-10-06 12:43	14,37	2,20	0,01	2,13	4,02	0,78	0,07	3,56	0,09	72,72	0,26		100,21

JG-1 STD	Majors Acid32	2015-10-29 11:44	14,45	2,21	0,01	2,12	4,02	0,77	0,06	3,68	0,10	72,48	0,26				100,16
JG-1 STD	Majors Acid32	2016-01-15 11:26	14,36	2,21	0,01	2,13	4,03	0,77	0,07	3,67	0,10	72,57	0,27				100,19
JG-1 std	Majors Acid32	2016-02-04 20:44	14,37	2,21	0,01	2,13	4,02	0,79	0,07	3,66	0,10	72,18	0,26				99,80
JG-1 STD	Majors Acid32	2016-02-11 17:46	14,34	2,21	0,01	2,13	4,03	0,78	0,06	3,61	0,10	72,19	0,27				99,73
JG-1 std	Majors Acid32	2016-03-08 16:08	14,13	2,21	0,01	2,13	4,02	0,75	0,07	3,43	0,09	72,03	0,26				99,13
J-G std	Majors Acid32	2016-03-14 22:57	14,12	2,21	0,01	2,13	3,98	0,75	0,07	3,42	0,10	71,98	0,26				99,03
JG-1 STD	Majors Acid32	2016-03-18 23:22	14,03	2,20	0,01	2,13	4,00	0,77	0,06	3,46	0,10	71,95	0,26				98,97
JG-1 STD	Majors Acid32	2016-04-12 23:22	14,11	2,21	0,01	2,13	4,00	0,76	0,07	3,42	0,10	72,13	0,26				99,20
JG-1 STD	Majors Acid32	2016-04-15 05:39	14,00	2,21	0,01	2,13	3,99	0,75	0,07	3,44	0,10	72,02	0,26				98,98
JG-1 std	Majors Acid32	2016-05-05 00:07	14,06	2,21	0,01	2,13	4,01	0,76	0,07	3,43	0,10	72,05	0,26				99,09
JG-1 STD	Majors Acid32	2016-06-07 00:20	14,00	2,20	0,01	2,13	4,01	0,77	0,07	3,44	0,10	71,81	0,26				98,80
JG-1 STD	Majors Acid32	2016-07-26 23:39	13,99	2,20	0,01	2,13	4,00	0,78	0,06	3,39	0,10	71,98	0,26				98,90
JG-1 std	Majors Acid32	2016-08-23 00:29	14,04	2,19	0,01	2,13	3,99	0,76	0,07	3,36	0,10	71,80	0,26				98,71
JG-1 std	Majors Acid32	2016-08-24 20:35	13,98	2,20	0,01	2,13	4,01	0,74	0,07	3,41	0,10	71,66	0,26				98,57
JG-1 std	Majors Acid32	2016-08-25 17:09	13,95	2,20	0,01	2,13	4,02	0,76	0,07	3,38	0,10	71,97	0,26				98,85
JG-1 std	Majors Acid32	2016-08-31 02:22	14,01	2,20	0,01	2,13	4,00	0,74	0,06	3,42	0,10	71,88	0,26				98,81
JG-1 STD	Majors Acid32	2016-09-01 03:51	14,01	2,19	0,01	2,12	3,98	0,75	0,07	3,43	0,10	71,72	0,26				98,64
JG-1 STD	Majors Acid32	2016-09-07 16:28	14,01	2,20	0,01	2,13	3,99	0,75	0,07	3,39	0,10	71,96	0,26				98,87
Average			14,15	2,20	0,01	2,13	4,01	0,76	0,07	3,48	0,10	72,13	0,26				99,30
Relative standard deviation (%)			0,37	0,98	6,38	0,53	0,96	2,95	7,50	2,68	2,16	0,23	0,35				0,05

Table D2: Standards used for LA−ICPMS

	Sc	V	Cr	Co	Ni	Cu	Zn	Rb	Sr	Y	Zr	Nb	Mo	Cs	Ba	La	Ce	Pr	Nd	Sm	Eu	Gd	Tb	Dy	H
Instrument DL	0,02	0,02	0,17	0,01	0,14	0,02	0,13	0,01	0,00	0,00	0,00	0,00	0,01	0,00	0,02	0,00	0,00	0,00	0,01	0,01	0,00	0,01	0,00	0,00	0
Method DL	0,45	0,36	3,33	0,16	2,88	0,41	2,60	0,16	0,07	0,03	0,10	0,03	0,19	0,07	0,41	0,03	0,04	0,03	0,14	0,20	0,05	0,15	0,02	0,09	0
Certified BHVO glass	**33,00**	**308,00**	**293,00**	**44,00**	**116,00**	**127,00**	**102,00**	**9,20**	**396,00**	**26,00**	**170,00**	**18,30**	**3,80**	**0,10**	**131,00**	**15,20**	**37,60**	**5,35**	**24,50**	**6,10**	**2,07**	**6,16**	**0,92**	**5,28**	**0**
Repl 1	30,69	305,80	262,40	42,66	116,30	121,30	108,40	9,25	363,50	22,22	151,10	16,70	3,89	0,11	123,20	14,45	35,24	4,87	22,60	5,86	1,90	5,69	0,81	4,98	0
Repl 2	31,85	315,70	280,70	42,94	117,70	120,64	102,00	9,10	380,20	22,86	154,00	16,90	3,96	0,10	126,40	14,20	35,57	4,83	23,12	5,81	1,87	5,69	0,81	4,83	0
Repl 3	32,24	317,40	282,10	43,44	118,00	119,16	99,10	8,79	381,60	23,23	156,20	16,90	4,03	0,10	125,00	14,25	35,56	4,92	23,31	5,81	1,97	5,63	0,83	4,85	0
Repl 4	31,92	317,70	282,60	43,13	117,70	121,60	103,90	8,95	380,90	22,88	155,10	16,91	3,95	0,10	124,60	14,14	35,58	4,94	23,12	5,75	1,88	5,74	0,81	4,92	0
Average Analysed	31,68	314,15	276,95	43,04	117,43	120,68	103,35	9,02	376,55	22,80	154,10	16,85	3,96	0,10	124,80	14,26	35,49	4,89	23,04	5,81	1,90	5,69	0,81	4,90	0
% Deviation	4,02	2,00	5,48	2,18	1,23	4,98	1,32	1,93	4,91	12,32	9,35	7,91	4,14	3,78	4,73	6,18	5,62	8,59	5,97	4,80	8,04	7,67	11,37	7,29	6
Certified BHVO powder	**31,42**	**313,80**	**287,60**	**44,90**	**120,00**	**137,20**	**105,10**	**9,52**	**399,20**	**26,23**	**174,60**	**18,53**	**1,06**	**0,10**	**134,40**	**15,44**	**38,08**	**5,42**	**24,78**	**6,17**	**2,05**	**6,29**	**0,95**	**5,27**	**0**
Repl 1	37,00	355,70	320,90	47,70	144,10	144,70	131,00	9,66	436,60	26,38	178,10	19,14	1,58	0,67	142,40	16,75	40,64	5,42	26,90	5,94	2,36	6,87	0,97	5,55	1
Repl 2	37,00	359,20	320,00	46,80	141,20	141,70	125,50	9,53	441,50	26,95	180,90	20,08	1,38	0,26	152,40	16,99	42,33	5,66	26,40	7,15	2,20	6,43	0,91	5,57	1
Repl 3	34,70	358,10	324,30	48,30	140,10	145,10	122,50	9,69	442,70	27,34	182,20	19,63	1,47	0,26	148,50	17,26	41,84	5,66	27,90	7,29	2,36	6,66	1,03	5,92	1
Repl 4	36,28	360,50	319,10	48,20	135,40	144,40	117,50	9,72	435,30	27,08	181,70	19,84	1,50	0,29	148,40	16,91	41,58	5,90	26,30	6,16	2,12	6,82	1,04	6,06	1
Repl 5	37,50	354,80	323,70	48,10	141,10	143,80	129,10	9,76	438,60	26,89	180,60	19,79	1,48	0,30	148,30	16,90	40,66	5,72	28,10	6,43	2,13	7,02	0,98	5,78	1

Repl 6	36,20	357,40	317,20	48,40	143,10	143,20	123,40	9,97	439,30	26,99	181,30	19,60	1,69	0,39	145,80	17,27	41,73	5,61	27,80	7,15	2,24	6,71	1,02	5,72	1
Repl 7	36,40	361,40	319,00	48,00	135,70	138,30	122,30	10,14	434,70	27,48	181,60	19,94	1,90	0,30	147,50	16,87	42,02	5,65	27,20	7,38	2,32	6,59	0,96	6,33	1
Repl 8	35,77	357,00	320,90	48,50	144,90	138,20	121,00	10,10	440,70	27,00	185,10	19,62	1,89	0,23	144,40	16,66	41,46	5,87	26,20	6,99	2,20	6,50	0,87	6,07	1
Repl 9	35,60	351,40	315,40	47,00	140,00	143,00	131,70	9,33	425,90	26,09	175,00	18,90	1,44	0,55	133,70	16,22	39,58	5,42	25,20	6,05	2,13	6,18	0,87	5,50	1
Repl 10	35,80	358,10	323,90	48,00	144,30	147,00	136,50	9,81	436,20	26,74	179,70	19,84	1,64	0,28	139,80	16,97	41,44	5,48	25,60	7,21	2,20	6,75	1,09	5,91	1
Repl 11	36,00	360,50	323,40	48,90	139,20	143,70	132,20	9,89	441,30	27,64	183,10	20,01	1,73	0,35	140,90	16,98	41,58	5,57	26,60	5,83	2,20	6,63	0,91	6,11	1
Repl 12	36,40	355,40	314,00	47,80	146,20	142,00	130,40	9,86	439,40	26,91	179,30	20,17	1,55	0,31	148,00	16,28	41,06	5,54	27,00	7,14	2,21	6,46	1,00	6,29	1
Repl 13	35,50	354,20	319,40	47,50	140,10	139,80	128,40	9,78	440,70	26,94	178,30	19,21	1,82	0,21	146,70	16,47	40,45	5,72	27,30	6,66	1,99	6,38	0,95	5,99	1
Repl 14	35,90	357,60	317,50	48,80	143,80	144,50	129,40	9,28	439,20	27,00	181,20	19,32	1,74	0,36	146,20	16,81	41,12	5,28	27,80	6,64	2,02	5,99	1,03	5,81	1
Repl 15	36,28	362,50	319,10	48,20	146,50	147,90	128,00	9,67	440,70	26,78	182,20	19,81	2,38	0,34	141,90	16,95	41,81	5,55	26,30	7,08	2,37	6,41	0,99	5,72	1
Repl 16	36,80	359,60	316,10	48,30	140,20	143,20	122,50	10,57	437,00	27,02	181,10	19,59	1,82	0,31	145,10	16,73	41,77	5,88	26,70	6,85	2,34	6,53	1,02	5,73	1
Average Analysed	36,20	357,71	319,62	48,03	141,62	143,16	126,96	9,80	438,11	26,95	180,71	19,66	1,69	0,34	145,00	16,81	41,32	5,62	26,83	6,75	2,21	6,56	0,98	5,88	1
% Deviation	0,56	0,65	1,79	0,48	3,13	0,81	2,64	0,63	0,29	0,16	0,79	2,55	8,91	8,89	2,03	3,28	0,63	1,46	0,62	5,51	0,08	1,52	2,38	6,54	3

Appendix E: Harker plots for Vredenburg Batholith.

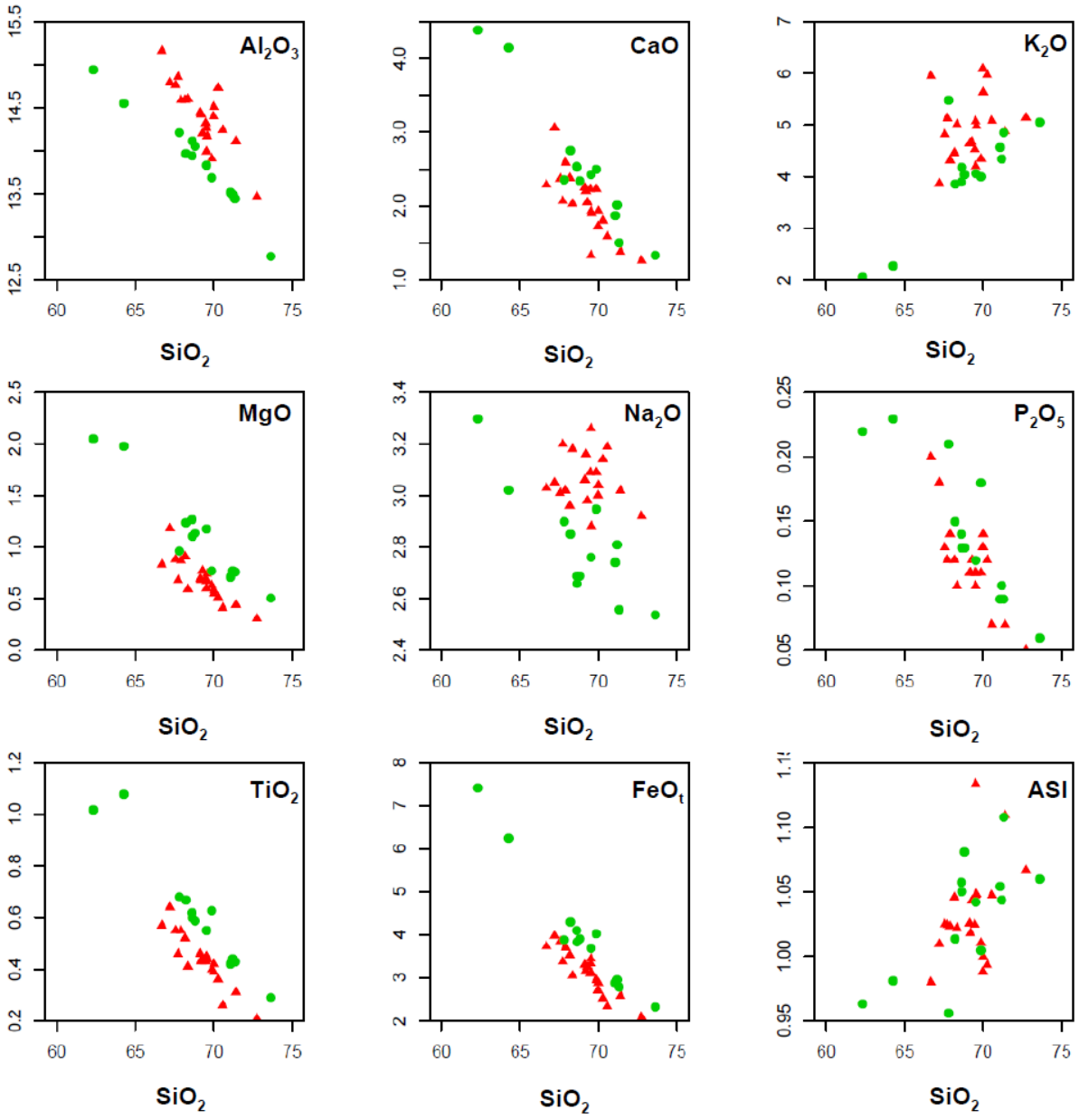

Figure E1: Harker plots for the Vredenburg Batholith granites and enclaves. Red triangles represent the granites and green circles the igneous enclaves

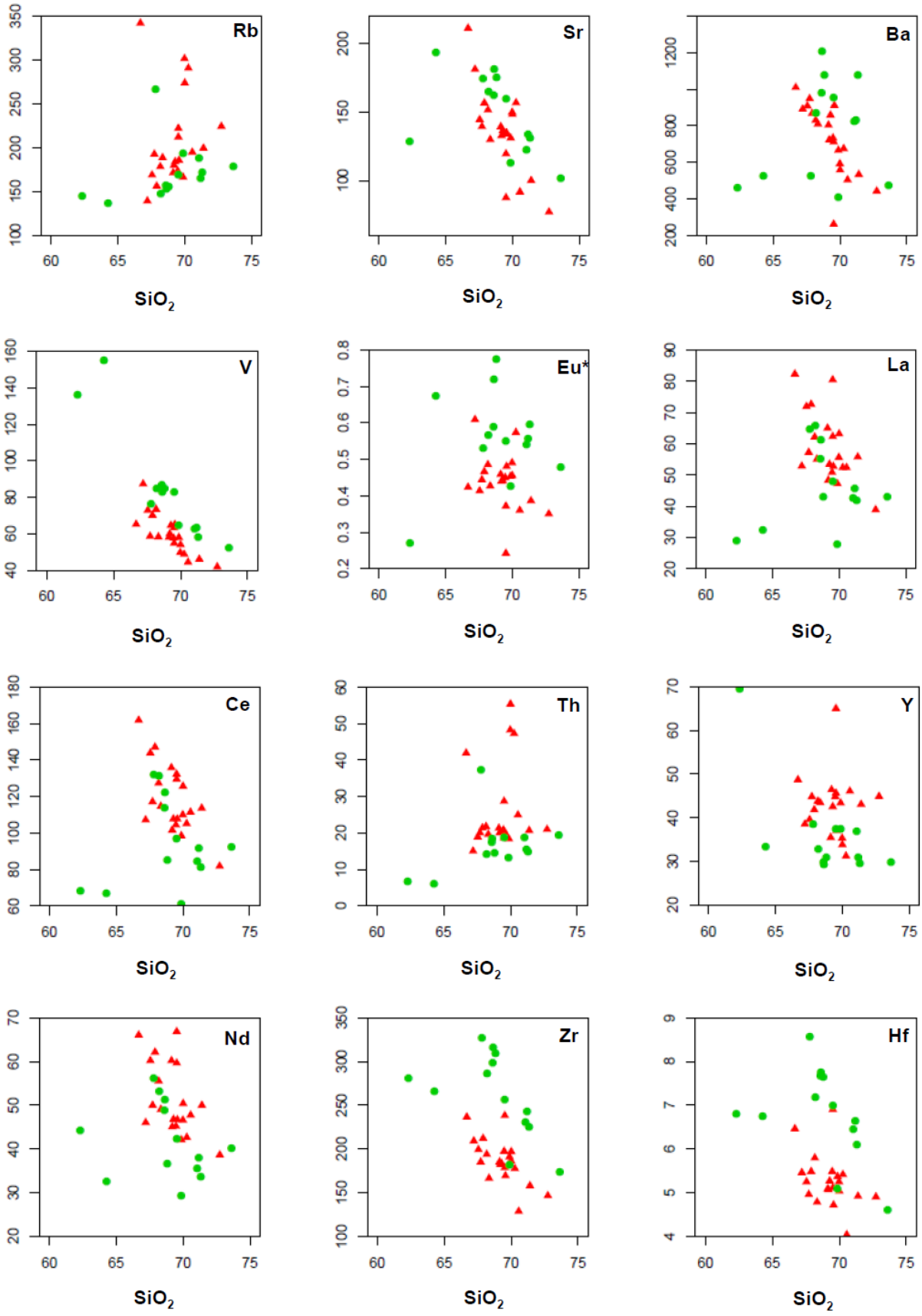

Figure E2: Selected trace elements Harker plots for the Vredenburg Batholith granites and enclaves. Symbols are the same as Fig. E1.

Appendix F: Tectonomagmatic discriminant function values.

Table F1: Discriminant function values for the five tectonomagmatic diagrams from (Verma et al., 2013).

	(IA+CA-CR+OI-Col)		(IA-CA-CR+OI)		(IA-CA-Col)		(IA-CR+OI-Col)		(CA-CR+OI-Col)	
Sample ID	DF1	DF2	DF1	DF2	DF1	DF2	DF1	DF2	DF1	DF2
PAT2	0,3928	-0,3756	0,5625	0,1013	0,8417	0,6998	0,0956	-0,2155	-0,0250	-0,2157
PAT10	0,1058	-0,0422	0,2455	-0,0831	0,5697	0,2205	-0,1202	-0,0833	-0,2378	0,2459
PAT11	0,3760	-0,2975	0,5762	-0,0208	0,8590	0,5271	0,1113	-0,1753	-0,0671	-0,1273
PAT14	-0,0127	0,0161	0,1062	-0,0352	0,4001	0,2479	-0,2772	-0,0601	-0,3396	0,3343
PAT17	0,1997	-0,1012	0,3269	0,0970	0,5829	0,4997	-0,1485	-0,0512	-0,1823	0,1481
PAT19	0,3083	-0,2801	0,5241	-0,0958	0,8434	0,4295	0,0833	-0,1948	-0,1388	-0,0689
PAT21	0,1285	-0,1666	0,3158	-0,1354	0,6501	0,2838	-0,0664	-0,1767	-0,2622	0,1044
PAT22	0,0223	-0,2011	0,1238	0,1741	0,4073	0,6429	-0,3131	-0,1780	-0,3136	0,1010
PAT26	0,1578	-0,1386	0,2250	0,2645	0,4611	0,6827	-0,2387	-0,0747	-0,1632	0,1081
PAT29	-0,0642	-0,2990	0,2250	-0,4658	0,7013	0,0227	-0,0464	-0,4021	-0,4932	0,0630
PAT31	-0,0060	-0,0074	0,1534	-0,1791	0,5028	0,0990	-0,1873	-0,1053	-0,3529	0,3251
PAT33	0,3041	-0,2897	0,5841	-0,3694	0,9781	0,1220	0,2389	-0,2645	-0,1573	-0,0757
PAT36	0,1420	-0,0846	0,2633	0,0903	0,5266	0,4766	-0,1979	-0,0586	-0,2269	0,1854
PAT37	0,6572	-0,1770	0,5674	0,9521	0,5489	1,4662	-0,1271	0,1766	0,3673	-0,1666
PAT39	0,8152	-0,3073	1,0215	0,0385	1,2165	0,6016	0,4861	-0,0398	0,3279	-0,3204
PAT41	0,3656	0,0121	0,3198	0,6335	0,4046	0,9714	-0,2703	0,1788	0,0844	0,1682
PAT43	0,4181	-0,3268	0,4855	0,5400	0,6128	1,1832	-0,1521	-0,0695	0,0181	-0,1941
PAT52	0,4313	-0,7647	0,7907	-0,2926	1,2462	0,5877	0,3860	-0,5713	-0,1319	-0,5817
PAT55A	0,6042	-0,7463	0,9304	-0,2187	1,3504	0,6245	0,5302	-0,5035	0,0691	-0,6422
PAT56	0,8630	-0,9212	1,3162	-0,4824	1,7765	0,4976	0,9164	-0,6037	0,2114	-0,9137
PAT4	0,5543	-0,7240	0,8951	-0,2900	1,3400	0,5300	0,5150	-0,5134	0,0150	-0,5923
PAT6	0,3293	0,0216	0,3668	0,1714	0,5845	0,4033	-0,0108	0,0581	0,0709	0,1795
PAT13	0,1733	-0,0379	0,2992	-0,1517	0,6138	0,1018	0,0256	-0,1002	-0,1108	0,1732
PAT15	0,4934	-0,0949	0,6754	-0,2804	1,0000	-0,0054	0,4026	-0,0745	0,1503	0,0051
PAT24	0,7022	-0,3236	0,9639	-0,3843	1,3232	0,0628	0,6868	-0,2081	0,2826	-0,3029
PAT25	0,1824	0,0323	0,2898	-0,2463	0,6642	-0,1189	0,1191	-0,0821	-0,0452	0,2556
PAT26A	0,3039	-0,1649	0,5399	-0,5248	0,9770	-0,2415	0,3901	-0,2441	-0,0285	0,0106
PAT28	0,3764	-0,1297	0,5717	-0,4005	0,9670	-0,1420	0,3928	-0,1738	0,0652	0,0145
PAT30	0,2705	-0,1300	0,5341	-0,5929	0,9834	-0,3192	0,3638	-0,2277	-0,0970	0,0765
PAT35	0,5713	-0,0642	0,6334	0,1813	0,8122	0,4881	0,2199	0,0659	0,2731	-0,0162
PAT50	-0,0647	-0,2224	0,2489	-0,5145	0,7502	-0,0679	-0,0694	-0,3316	-0,5453	0,1941
PAT54	0,4256	-0,5545	0,7386	-0,4292	1,2334	0,1954	0,4825	-0,4681	-0,0328	-0,3738
PAT18	1,3256	-0,2697	0,9442	1,7193	0,7204	2,1719	0,3003	0,3588	1,3108	-0,6290
PAT34	0,9376	0,0493	0,6064	1,3710	0,5325	1,5584	0,0264	0,4499	0,8965	-0,0511
PAT38	2,6658	-1,0729	2,2048	2,8883	1,5206	4,1621	1,0191	0,3808	2,4752	-2,0759
PAT45	2,0871	-0,7478	1,6866	2,7696	1,0290	3,9409	0,3270	0,5194	1,7659	-1,4226
PAT46	2,6860	-0,5095	2,4811	1,6183	2,0605	2,3280	1,5807	0,5920	2,3769	-1,4113
PAT47	2,7001	-0,4575	2,3892	2,1911	1,7675	3,0069	1,2035	0,7872	2,3601	-1,3658
PAT48	2,6840	-0,4334	2,3568	2,1540	1,7647	2,9103	1,2355	0,7793	2,3861	-1,3364
PAT49	2,7512	-1,0932	2,3314	2,9921	1,5739	4,3882	0,9570	0,4550	2,4370	-2,1019